Master of Science Thesis

Experimental Characterization of a Micro-ramp Wake and its Flow Mixing Properties in Supersonic Flow

Aabhas Srivastava

August 19, 2014

Aerodynamics

Faculty of Aerospace Engineering

TU Delft

Delft University of Technology

Experimental Characterization of a Micro-ramp Wake and its Flow Mixing Properties in Supersonic Flow

Master of Science Thesis

For obtaining the degree of Master of Science in Aerospace Engineering
at Delft University of Technology

Aabhas Srivastava

August 19, 2014

Faculty of Aerospace Engineering · Delft University of Technology

Delft University of Technology

DELFT UNIVERSITY OF TECHNOLOGY
DEPARTMENT OF AERODYNAMICS

The undersigned hereby certify that they have read and recommend to the Faculty of Aerospace Engineering for acceptance the thesis entitled **"Experimental Characterization of a Micro-ramp Wake and its Flow Mixing Properties in Supersonic Flow"** by **Aabhas Srivastava** in fulfillment of the requirements for the degree of **Master of Science**.

Dated: August 19, 2014

Supervisors:

Dr.ir. B.W. van Oudheusden

Dr.ir. F.F.J. Schrijer

Dr.ir. G.E. Elsinga

Ir. R.H.M. Giepman

Preface

This thesis marks the culmination of my masters course in Aerodynamics at the Faculty of Aerospace Engineering, Delft University of Technology. The research has been performed under the supervision of Dr.ir. B.W. van Oudheusden and Dr.ir. F.F.J. Schrijer, along with the able guidance of Ir. R.H.M. Giepman.

At the onset of this report, I would like to express my gratitude to the Justus van Effen foundation and the Delft University of Technology for funding my masters with a scholarship. Without the scholarship, I would have missed an excellent opportunity to study in Delft. All the experiments for this study were done at the TST-27 supersonic wind tunnel at the High Speed Laboratory, TU Delft. I am deeply indebted to my mentors, Dr. Schrijer and Dr. Oudheusden, whose help, guidance, stimulating suggestions and encouragement helped me in my research. I also extend my gratitude to Rogier, who helped me during my experiments and also guided me whenever I took a wrong turn during my research. The research has been exhilarating for me. A special thanks goes to the technical staff comprising of Frits, Peter, Eric, Henk-Jan and Nico for the excellent support during my test campaign.

Moreover, I also thank my close friends in Delft, Caroline, Pradeep, Avigyan, Nouman, Richard, and others from the society Rock n' Delft, who made my stay in Delft fun-filled, wonderful and extra-ordinary. Special thanks to Cedric and Naresh, who helped me in starting with LATEX to write my report.

Last but not the least, I would like to thank my family, whose never-ending love and support, from a distance of thousands of kilometers, helped me reach so far in my life.

Aabhas Srivastava
Delft,
The Netherlands.

Summary

Micro-ramps are currently being investigated as a means of reducing negative effects of shock wave-turbulent boundary layer interactions. A micro-ramp enhances the mixing of the flow by introducing vortices in the flow, thus energizing the boundary layer to overcome the adverse pressure gradient due to an impinging shock. The effect of changing micro-ramp height, Mach number and Reynolds number on the mean flow downstream of a micro-ramp's center-line has been studied extensively.

In the present study, a single micro-ramp (geometry defined by Anderson et al. (2006)) was used in the supersonic TST-27 wind-tunnel at different incoming flow conditions. Experimental investigations were done using surface oil flow visualization and planar particle image velocimetry (PIV). The TST-27 wind-tunnel has a movable throat section which was used to vary the Mach numbers from 1.5 to 3. The unit Reynolds number was controlled by varying the pressure in the stagnation chamber to give values ranging from 28 million to 64 million. Differences in the mean flow characteristics behind the micro-ramp were observed by varying the aforementioned parameters.

The undisturbed boundary layer profiles and properties matched well with the trends reported in literature for changing Mach number and Reynolds number. The wind tunnel fluctuation levels were also observed to be in agreement with Klebanoff (1955).

The effects of varying the micro-ramp height were similar to the ones reported by Babinsky et al. (2009). The wake location and the momentum-deficit region scaled with micro-ramp height and the larger micro-ramp gave a fuller velocity profile near the wall but also had a larger wake. The wake strength was observed to be higher for the larger micro-ramp.

Several interesting observations were made when the Mach number was changed. The oil flow visualization showed that the primary vortices moved closer with an increasing Mach number. The wake location was lower for a higher Mach number, though the size of the momentum deficit region remained the same for the tested range of Mach numbers. The velocity profile was fuller near the wall for the lower Mach number. It was also deduced that the rate of the decay of circulation, when moving downstream, did not depend on the Mach number.

Varying the Reynolds number showed some effects on the flow characteristics near the micro-ramp but the differences seemed to disappear while moving downstream. The wake location

and the size of the momentum deficit region did not change for the tested Reynolds number range. For the higher Reynolds number case, the wake and upwash strength were lower in the vicinity of the micro-ramp.

Table of Contents

List of Figures

List of Tables

Nomenclature

λ_c	Compressible flow length scale	m
λ_i	Incompressible flow length scale	m
μ_∞	Coefficient of dynamic viscosity for air in the test section	Ns/m^2
μ_f	Dynamic viscosity of fluid	Ns/m^2
$\rho(y)$	Density in the boundary layer	kg/m^3
ρ_w	Density at wall	kg/m^3
ρ_∞	Density in the test section	kg/m^3
C_p	Specific heat capacity of air at constant pressure	J/kgK
h	Micro-ramp height	mm
M_∞	Freestream Mach number in the test section	-
r	Recovery factor, 0.89 for turbulent flows	-
$T(y)$	Temperature in the boundary layer	K
T_w	Temperature at wall	K
T_{aw}	Adiabatic wall temperature	K
U_∞	Freestream velocity in the test section	m/s
U_{min}	Value of the minimum horizontal velocity in the micro-ramp wake	m/s
V_{max}	Value of the maximum vertical velocity in the micro-ramp wake	m/s
x	Horizontal axis with origin at the trailing edge of the micro-ramp	mm
x'	Horizontal axis with origin at the start of the first Field of View	mm

x_{MR}	Distance between micro-ramp trailing edge and the start of first field of view	mm
y	Wall-normal distance	mm
y_{upwash}	Location of V_{max}	mm
y_{wake}	Location of U_{min}	mm
δ^*	Compressible displacement thickness	mm
δ_{99}	Boundary layer thickness	mm
δ^*_{inc}	Incompressible displacement thickness	mm
Γ	Circulation strength	m^2/s
ν	Kinematic viscosity of air	m^2/s
ρ_f	Density of the fluid	kg/m^3
ρ_f	Fluid density	kg/m^3
ρ_p	Tracer particle density	kg/m^3
τ_f	Flow characteristic time	s
τ_p	Particle response time	s
θ_{inc}	Incompressible momentum thickness	mm
θ	Compressible momentum thickness	mm
C_f	Skin friction coefficient	-
h_e^+	Effective device height Reynolds number	-
h_v	Vortex core height	mm
H_{inc}	Incompressible Shape factor	-
H	Compressible Shape factor	-
P_o	Total pressure in the stagnation chamber	Pa
r_c	Vortex core radius	m
r_p	Tracer Particle radius	m
Re_θ	Reynolds number based on θ , $\mathrm{Re}_\theta = \frac{\rho_\infty U_\infty \theta}{\mu_\infty}$	-
$Re_{\theta_{inc}}$	Reynolds number based on θ_{inc} , $\mathrm{Re}_{\theta_{inc}} = \frac{\rho_\infty U_\infty \theta_{inc}}{\mu_\infty}$	-
Re	Unit Reynolds number $\mathrm{Re} = \frac{\rho_\infty U_\infty}{\mu_\infty}$	-
S_k	Particle Stokes number	-

T_o	Total temperature	K
T_∞	Static temperature in the test section	K
u_τ	Wall friction velocity	m/s
u_θ	Tangential velocity around a vortex	m/s
u_f	Fluid velocity	m/s
u_p	Tracer particle velocity	m/s
$\overline{u}_{BL}$	Mean horizontal velocity in the undisturbed boundary layer	m/s

Chapter 1

Introduction

> "We were in a turn and climbing when one of the inlets showed signs of instability. Shortly thereafter - KER BLAM! - the aircraft slammed my head against the side of the cockpit and then momentarily became unstable as it yawed, pitched, and vibrated."

This is how retired reconnaissance systems officer Roger Jacks recounted an engine inlet failure or 'unstart' in a book by retired Lockheed SR-71 pilot R.H. Graham (1996)). For jet airplanes flying at speeds faster than Mach 1, the air entering the engine also moves supersonically. Turbojet compressors cannot handle the supersonic airflow. Supersonic inlets are, hence, needed to slow the incoming supersonic air to subsonic speeds so that this air can be fed to the engines. One of the ways to make the flow subsonic is by using a mixed compression inlet nozzle as shown in figure 1.1, which introduces a series of oblique shocks to decelerate the flow. Mixed compression inlets allow the flow to be supersonic within a small portion of the inlet. The shape of the inlet can be changed by either moving the inner centerbody or the outer surface to reposition the terminal shock for maximum efficiency according to the flight conditions. A larger number of shocks give a better pressure recovery (Goldsmith and Seddon (1993)), but it also implies that the inlet will be longer and heavier. Also the boundary layer grows substantially thicker in a longer inlet, reducing the inlet mass flow and hence the efficiency of the engine. If there is flow separation in the engine, it can result in violent breakdown of the supersonic flow in the inlet and the establishment of subsonic flow through the inlet and out in front of it. This change in the compression process is known as engine unstart.

The shock wave boundary layer interaction do not just occur in supersonic inlets, but are also observed in turbomachinery and on transonic wings. An improvement of jet engines towards higher efficiency requires higher compression ratios in compressors. This requirement leads to considerable increase in flow velocities relative to compressor blades, at times reaching supersonic speeds. The shock waves occurring as a consequence of these high velocities influence the pressure rise and make the boundary layer thicker, leading to a smaller cross-section area for the mass flow, thus, affecting the efficiency of the engine. An example of

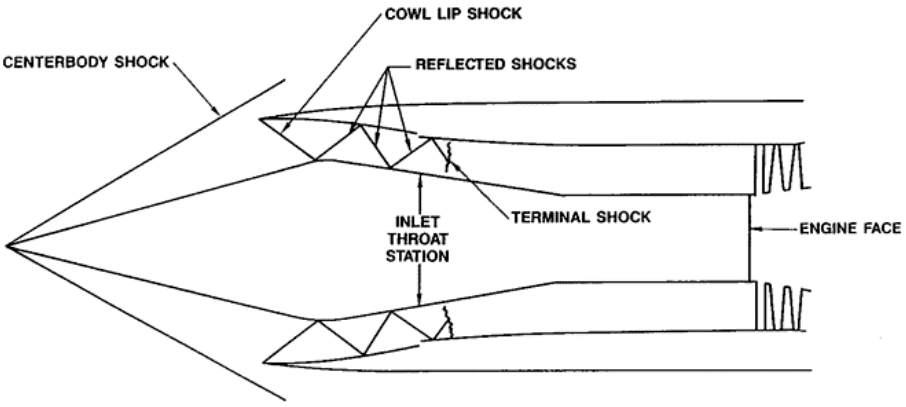

Figure 1.1: A supersonic jet inlet showing the locations of shock to make the incoming flow subsonic.

SWBLI in a compressor cascade is shown in figure 1.2.

When an airfoil is flying at transonic speeds, at the critical freestream Mach number, the local flow becomes sonic at a single point on the upper surface. As the freestream Mach number increases over its critical value, a region of supersonic flow develops on the upper surface of the airfoil. The deceleration causes the flow to re-compress through a shock. A strong adverse pressure gradient introduced by this shock wave may cause the boundary layer to separate as shown in figure 1.3. In addition, a sudden impulse may lead to unsteady fluctuation of the shock location on the airfoil surface, leading to 'shock buffeting'. The low-frequency unsteady fluctuations cause the shock wave to oscillate on the airfoil surface accompanied by intermittent separation. The fluctuating aerodynamic load, due to intermittent separation and shock movement may lead to flutter on the airfoil which can cause structural problem for the wing.

Boundary layer control is, thus, one of the major research areas to control shock wave-boundary layer interactions. Boundary layer bleed and vortex generators are two well known methods to control the boundary layer separation in such flows. The bleed method removes the low momentum portion of the boundary layer, making the velocity profile fuller near the wall to be more resistant against separation, but ends up reducing the mass flow of the incoming flow in the engine. Vortex generators are used to control the boundary layer separations from smooth surfaces. Different types of vortex generators have been studied by researchers including wedge type devices, counter rotating vanes and single rotation vanes. Micro-ramps or micro vortex generators (MVGs) are passive boundary layer control devices (wedge type) which can be used instead of bleed method. They energize the boundary layer by introducing two counter-rotating vortices in the flow (Ashill et al. (2005)). Whether the micro-ramps are superior to bleed method or not, this is still another question to be investigated.

Figure 1.4 shows a typical micro-ramp as defined by Anderson et al. (2006) which has been used for experiments by different researchers, where the dimensions are normalized by the micro-ramp height h. It has been reported by Babinsky et al. (2009) that micro-ramps can reduce the boundary layer shape factor, reducing the chances of separation. Babinsky (2007)

Figure 1.2: Schlieren image of SWBLI in compressor cascade at M=1.25 (Source: Institute of Propulsion Technology, DLR).

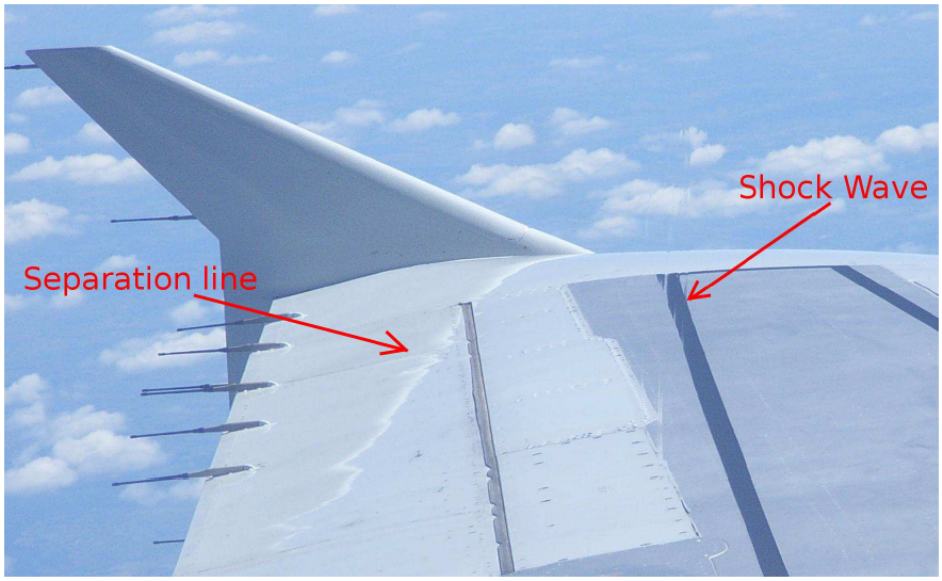

Figure 1.3: Shock wave and boundary layer separation on the wing of an Airbus A320 aircraft. The shock is visble through refraction of the wing and clouds in the background. The separation line can be seen by the accumulation of white deposits on aileron. (Source: Souverein (2010))

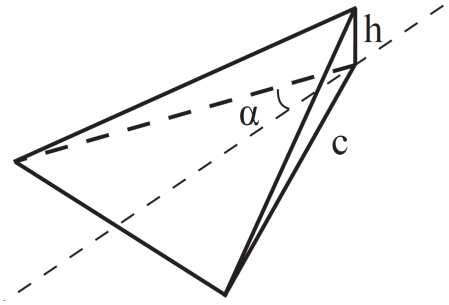

Figure 1.4: A typical Micro-ramp geometry where c=7.5h, $\alpha = 24^{\circ}$.

showed that for same flow conditions, the flow development behind the micro-ramp scales with micro-ramp height. Experiments and numerical studies have been conducted at different flow conditions by researchers (Blinde et al. (2009); Giepman et al. (2013); Hirt and Anderson (2009); Babinsky et al. (2009); Lee et al. (2007)) to study the effect of Micro-ramps on the boundary layer profile. Since earlier experiments were carried out at different flow conditions, for results to be of interest to industry, the key is to quantify the effects of Mach and Reynolds number on the mixing properties of the ramp.

1.1 Thesis Aims and Objectives

For the research on micro-ramps to be of interest to the industry, the key aim is to quantify the effects of changing in-flow conditions on the flow mixing properties of the micro-ramp. To this cause, the objectives of this thesis project are listed as follows:

- Obtain and analyze the wake properties using PIV along the center-line of micro-ramps at different micro-ramp heights, Mach numbers and Reynolds numbers.
- Obtain a more complete view of the surface flow and the momentum near the wall with the micro-ramp by Oil Flow Visualization.
- Compare the obtained data with other researchers and propose a model to quantify the wake properties based on the micro-ramp height, flow Reynolds number and flow Mach number.

In this study, the experimental data at different Reynolds number (28, 40, 52 and 64 million) ; different Mach numbers (1.5, 2 , 2.5 and 3) and for different micro-ramp heights (6mm, 8mm and 10 mm) were collected. The properties that were analyzed from the mean flow profile behind the micro-ramp include the wake location, the wake strength, the upwash strength, shear layer locations and the incompressible shape factor. Surface oil flow visualizations were used to confirm the flow model proposed by Li et al. (2011) and to observe the change in vortex footprints at different flow conditions.

1.2 Thesis Outline

Chapter 2 gives a theoretical survey of the literature defining the fundamental properties of turbulent boundary layers, shock wave-turbulent boundary layer interactions and a review of studies on micro-ramps outlining the fundamental concepts of the flow that will be dealt with in the thesis.

Chapter 3 is devoted to the description of the measurement techniques and experimental arrangements. The flow facility is described and the micro-ramp geomtery are first described, followed by an outline of the working principles of planar Particle Image Velocimetry (PIV), as well as the experimental considerations for PIV set-up. It is followed by an outline of the surface oil flow visualization technique used for the experiment. At the end of the chapter, the experimental matrix is presented.

Chapter 4 presents the undisturbed velocity profiles obtained from planar PIV at different test conditions. It discusses the effects of changing Mach number and Reynolds number on boundary layer properties. The chapter ends with an analysis of the fluctuation levels present in the tunnel.

Chapter 5 presents a description of all results obtained from the experiments with micro-ramps. The oil flow results are first presented. It is followed by a description of the mean flow results obtained from the PIV data along the micro-ramp's center-line. The micro-ramp wake's properties are categorized with the evolution wake-location, wake strength, upwash strength, shear layers and shape factor with respect to the distance behind the micro-ramp. An analysis of the results is then presented in a separate section.

Chapter 6 presents the major conclusions drawn from the study. And finally in chapter 7, the recommendations and outline for future work are presented.

Chapter 2

Theoretical Background

The micro-ramp vortex generator will be mounted on a surface in the turbulent boundary layer, hence, it is necessary to introduce the properties of turbulent flows. Adverse pressure gradient occurring due to a shock impinging on the boundary layer can induce flow separation. Babinsky et al. (2009) showed that a fuller boundary layer profile due to vortex mixing from micro-ramps, allows the flow to pass through a shock with less separation.
In this chapter, the turbulent boundary layer profile is first discussed, followed by the flow physics of shock induced boundary layer separation and a literature study of the flow features behind the micro-ramp.

2.1 Turbulent Boundary Layers

Turbulent boundary layers have a wide spectrum of eddy sizes and a corresponding spectrum of fluctuation frequencies. The motion can be thought of as a tangle of many vortex elements aligned randomly in all directions and having a highly unsteady velocity field. Turbulent flow regimes are characterized by chaotic property changes in both space and time. A turbulent boundary layer is marked by unsteady mixing of the flow on macroscopic scale (White and Corfield (2006)) leading to large scale exchange of mass, momentum and energy.

The turbulent boundary layer profile consists of an inner layer, an overlapping layer and an outer layer (White and Corfield (2006)) and a typical profile is shown in figure 2.1(a). The flow in the inner layer is majorly governed by the fluid properties, the wall shear stress and on the distance away from the wall. It is called the viscous sublayer and the dimensionless form of the governing equation is given by equation 2.1, where u^+ and y^+ are defined in equation 2.4.

$$u^+ = y^+ \qquad for \qquad y^+ \leq 5 \tag{2.1}$$

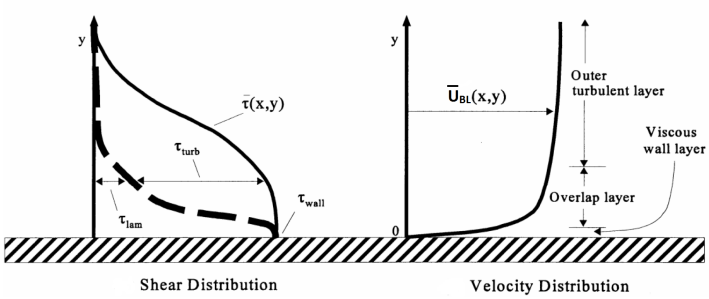

(a) Typical shear stress and velocity profile for turbulent boundary layer Norfleet and Savannah (2005).

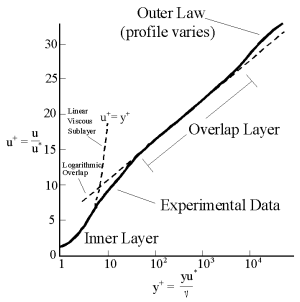

(b) Viscous sublayer and Logarithmic law in overlap region Norfleet (1998).

Figure 2.1: Turbulent Boundary layer profiles.

On the other hand, for the outer layer, the wall is just a source of retardation, reducing the local velocity $\overline{u}_{BL}(y)$ depending on the wall shear stress, freestream pressure gradient and the boundary layer thickness. The outer law is often called the velocity defect law and is given by equation 2.2.

$$\frac{U_\infty - \overline{u}_{BL}}{v^*} = -\frac{1}{\kappa}\ln\left(\frac{y}{\delta_{99}}\right) + A \tag{2.2}$$

where U_∞ is the freestream velocity, $\overline{u}_{BL}$ is the mean horizontal flow velocity in boundary layer and δ_{99} is the boundary layer thickness. A is constant that varies primarily with the pressure gradient in the flow but also depends on other flow parameters.
The overlap layer is the region where the the profiles defined by the outer law and inner law merge. It is defined by a logarithmic region using dimensionless parameters, and is called the log-law (equation 2.3). The non-dimensonal velocity profile showing log law is shown in figure 2.1(b).

$$u^+ = \frac{1}{\kappa}\ln(y^+) + B \qquad for \qquad y^+ \geq 30 \tag{2.3}$$

where κ and B are near universal constants for turbulent flows having typical values of 0.41 and 5, respectively.

The non-dimensional parameters used in the equations for velocity profiles are defined as follows:

$$u^+ = \frac{\overline{u}_{BL}}{u_\tau} \qquad y^+ = \frac{y u_\tau}{\nu} \qquad u_\tau = \left(\frac{\tau_w}{\rho_f}\right)^{\frac{1}{2}} \tag{2.4}$$

where u_τ is the wall friction velocity , ν is the kinematic viscosity of the fluid, τ_w is the wall shear stress and ρ_f is the density of the fluid.

For compressible flows, Van Driest (1951) defined an equivalent effective velocity u_{eq} for

adiabatic walls replacing the $\overline{u}_{BL}$ in the left hand side of equation 2.3, i.e. $u^+ = \frac{u_{eq}}{u_\tau}$.

$$u_{eq} = \frac{U_\infty}{a}\sin^{-1}\left(\frac{a\overline{u}_{BL}}{U_\infty}\right) \qquad a^2 = 1 - \frac{T_\infty}{T_w} \tag{2.5}$$

where T_∞ is the temperature in freestream and T_w is the wall temperature.
The turbulent velocity profile can be described with a limited number of boundary layer parameters, typically the boundary layer thickness δ_{99}, momentum thickness θ, the incompressible shape factor H_{inc} and the skin-friction coefficient C_f.
The boundary layer thickness δ_{99} is the y-location where the value of the u-velocity is 99% of the freestream value U_∞. The displacement thickness, denoted by δ^*, is the distance by which the surface needs to be moved away from a reference plane in an inviscid flow of velocity U_∞ to give the same flow rate as occurs between the surface and the reference plane in viscous (real) fluid. The compressible and incompressible displacement thickness, as described by Anderson Jr (1985), are given as

$$\delta^* = \int_o^\infty \left(1 - \frac{\rho u}{\rho_\infty U_\infty}\right) dy \tag{2.6a}$$

$$\delta^*_{inc} = \int_o^\infty \left(1 - \frac{u}{U_\infty}\right) dy \tag{2.6b}$$

Momentum thickness or θ is the distance by which a surface would be moved towards the reference plane in an inviscid fluid of velocity U_∞ to give the same momentum as exists between the surface and reference plane in viscous (real) fluid. The compressible and incompressible momentum thickness (Anderson Jr (1985)) are given as

$$\theta = \int_o^\infty \frac{\rho u}{\rho_\infty U_\infty}\left(1 - \frac{u}{U_\infty}\right) dy \tag{2.7a}$$

$$\theta_{inc} = \int_o^\infty \frac{u}{u_\infty}\left(1 - \frac{u}{U_\infty}\right) dy \tag{2.7b}$$

Skin friction coefficient C_f is a measure of the friction arising due to interaction between the wall and fluid and is related to τ_w by the relation $C_f = \frac{\tau_w}{\frac{1}{2}\rho_\infty U_\infty^2}$ and hence, it is also related to friction velocity (refer to equation 2.4). The skin friction coefficient for a flat plate turbulent boundary layer, as reported by Cousteix (1989), varies as a function of the unit Reynolds number and the Mach number. It decreases with increase in Reynolds number (for a fixed Mach number) and it increases with Mach number (at a fixed unit Reynolds number).

Humble (2009) pointed out that a higher skin friction coefficient C_f results in an increase of the boundary layer's resistance to adverse pressure gradients. However, the shape factor H_{inc}, characterizing the fullness of boundary layer profile, also varies when flow conditions are changed to vary C_f. At higher Reynolds number in turbulent flows, the C_f is lower (increase in the denominator ρ_∞ dominates the increase in τ_w with increasing Reynolds number). However, the boundary layer is fuller near the wall (Schlichting et al. (2000)) and the subsonic region in boundary layer is smaller, thus, reducing the chances of separation (as explained in next section).

2.2 Shock Wave Boundary Layer Interactions

When an incident shock interacts with a turbulent boundary layer, the boundary layer goes through a region of adverse pressure gradient which may strongly distort the boundary layer velocity profile. Before starting with micro-ramp vortex generator control of shock induced separation, it is required to understand the physics of Shock Wave Boundary Layer Interaction.

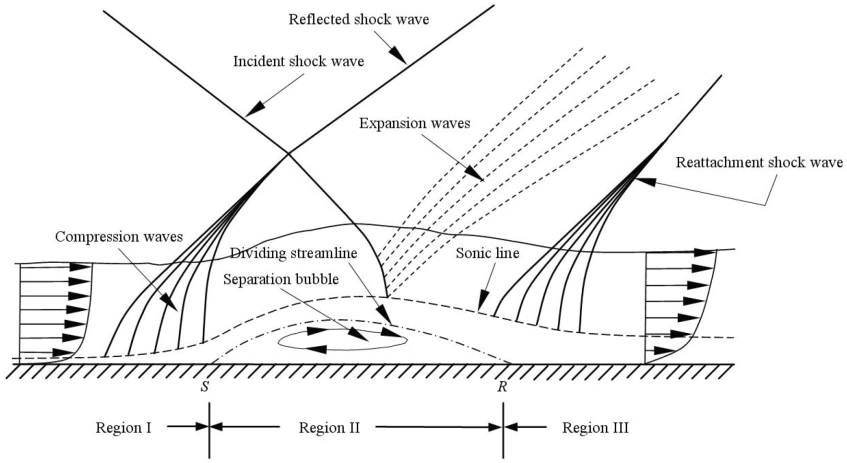

Figure 2.2: Flow topology of the separated incident shock wave turbulent boundary layer interaction from Humble (2009). Based on the schematic of Délery and Bur (2000).

The schematics of SWBLI, which leads to separation, are shown in figure 2.2 reproduced from Humble (2009). The interaction region can be subdivided into three parts, as shown in the figure. In **region I**, when the incident shock strikes the surface downstream, the information about the pressure change across it is transmitted upstream through the subsonic portion of the boundary layer (below the dashed line). Due to the pressure rise, the streamlines in the low-momentum fluid near the wall begin to separate. The compression waves start forming in the region I before the flow separates and coalesce to form the reflected shock. In **region II**, the flow starts turning upstream due to separation and the skin friction coefficient becomes zero at the separation point **S**. Downstream of this point, there exists a separation bubble containing the recirculating fluid, bounded by the wall and a dividing streamline stretching from separation point **S** and reattachment point **R**, as shown in the figure. The separation region's size depends on the ability of the local shear layer to overcome the adverse pressure gradient. The reverse flow in the separated region and the shear layer interact, transferring momentum to the flow near the wall. As the separating streamline gains more momentum, it overcomes the adverse pressure gradient and reattaches to the surface. **Region III** contains a series of compression waves (coalescing to form the recompression shock) due to the flow turning parallel to the wall after the reattachment point R. The mean properties of the boundary layer take a long time to recover (O(10) of the undisturbed boundary layer thickness, Wu and Martin (2007)) to the original values after reattachment occurs.

2.3 Micro-ramp Vortex Generators

The micro-ramp devices used in this thesis project are a result of the optimization study performed by Anderson et al. (2006). They used Reynolds Averaged Navier Stokes (RANS) analysis, combined with experiments in NASA Glenn Research Center and Design of Experiments methodologies (Central Composite Face Centered design) for their study. Anderson used *Response Surface Methodology* to arrive at an optimal design of micro-array actuators which could effectively control shock wave turbulent boundary layer interactions. They tested three different micro-devices, standard micro-vanes, tapered micro-vanes and standard micro-ramps as shown in figure 2.3.

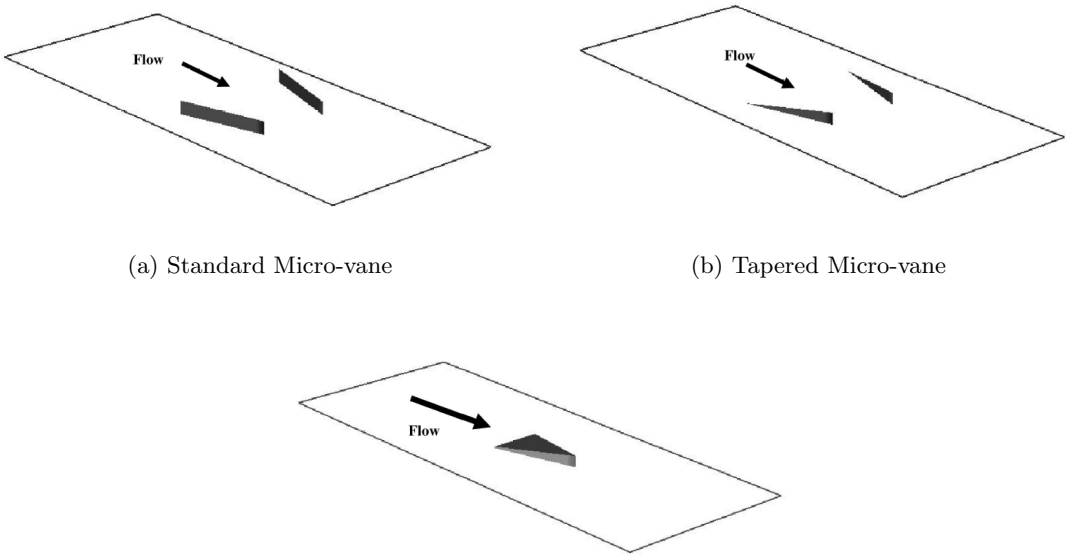

(a) Standard Micro-vane

(b) Tapered Micro-vane

(c) Standard Micro-ramp

Figure 2.3: Schematic diagram showing different micro-devices used by Anderson et al. (2006).

The micro-devices were tested by measuring the shock interaction downstream of the device using a 10° shock generator in a Mach 2.0 flow, which was strong enough to separate a turbulent supersonic boundary layer. The main objective was to vary the geometry of the devices in such a way that the total pressure recovery ($\frac{DP}{P_o}$) is maximized and the incompressible shape factor (H_{inc}) is minimized downstream of the shock boundary layer interaction. These two variables were chosen because total pressure recovery ($\frac{DP}{P_o}$) denotes the amount of 'work' present in the flow and higher the total pressure, the more energy can be extracted from it, thus giving the flow ability to recover from the adverse pressure gradient due to the shock. A lower incompressible shape factor H_{inc} results in a fuller turbulent profile with smaller subsonic region, thus being less prone to separation due to SWBLI. All the different devices were found to have comparable effects to the boundary layer bleed technique. Counter rotating vanes separated by a gap of 1 device height were most effective in reducing the extent of the flow separation (Anderson et al. (2006)). However, micro-ramps can still be considered to be

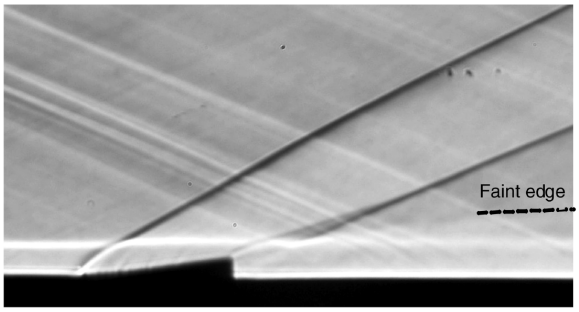

Figure 2.4: Schlieren picture from Babinsky et al. (2009).

the most practical flow control device in supersonic inlets due to its ease of mounting on the surface and its robustness. For micro-ramp geometry, as shown in figure 1.4, the half-angle α, micro-ramp height h and $\frac{c}{h}$ ratio were varied. From the DOE tests, a micro-ramp geometry with $\alpha = 24°$ and $\frac{c}{h} = 7.2$ was arrived which formed the basis of tests for subsequent research.

2.3.1 Flow features in the Micro-ramp's wake

Many researchers have done detailed study of the wake behind a micro-ramp and the flow features existing in the region. Babinsky et al. (2009) performed experimental studies on micro-ramps at Mach 2.5 and unit Reynolds number 40 million. They took Schlieren images and measured streamwise velocity profiles using one component Laser Doppler anemometry (LDA). The schlieren image by Babinsky can be seen in figure 2.4. The boundary layer is clearly discernible in the flow field. The faint edge, as reported by Babinsky, is the upper boundary of the low momentum region in the micro-ramp's wake. The measured shock angles from Babinsky's experiments are: 26.8° for the first shock at the leading edge of the micro-ramp and 21.9° for the re-compression shock at the trailing edge.
Babinsky et al. (2009), through surface flow visualization, schlieren measurements and Laser Doppler Velocimetry, proposed the vortex model for the mean flow behind the micro-ramp. Figure 2.6 shows that there exist two primary vortex structure arising from the edge of the micro-ramp. There is a secondary vortex arising from the leading edge corner of the ramp on each side, forming horse-shoe vortex downstream; and two counter-rotating secondary vortices, on each side, arising from the 90° sharp trailing edge at the micro-ramp center line(figure 2.7(a)).

Li and Liu (2010) did LES study on similar micro-ramp with the declining part of the trailing edge at an angle of 70° instead of 90° as used by Babinsky. They had comparable leading edge shock angle as 26.9° and re-compression shock angle as 24.6°. Li and Liu (2010) also confirmed a vortex structure similar to the one proposed by Babinsky et al. (2009) from their LES studies. They gave a view of the possible 3-D structure of the shocks in figure 2.5 by instantaneous cross-section pressure contours. The first section shows the shock due to the micro-ramp leading edge. The second section shows the leading edge shock on top and an expansion fan structure in the bottom near the trailing edge of the micro-ramp. Rest of the sections show the evolution of the leading edge shock (in orange) and the re-compression shock

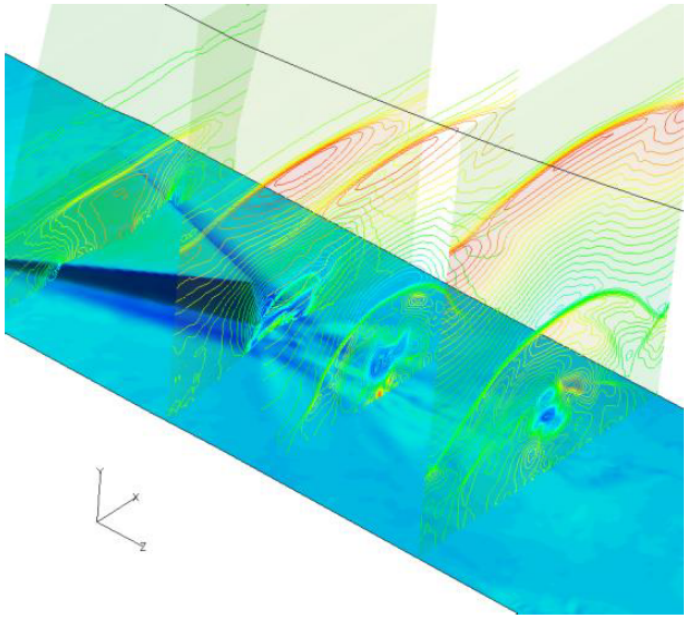

Figure 2.5: Overview of 3D shock structure behind micro-ramp given by instantaneous cross-section pressure contours Li and Liu (2010).

(in green). The arc-like shape of re-compression shocks implies that the re-compression shock makes the expansion flow from the micro-ramp edges satisfy the virtual boundary condition created by streamwise vortices. The expanded flow forms a shear layer around the streamwise primary vortices at least at the initial stage of formation of shock wave.

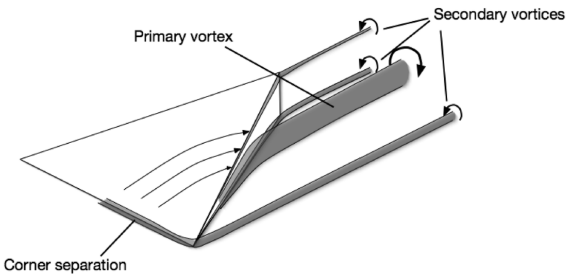

Figure 2.6: Sketch of main flow features suggested by Babinsky et al. (2009) (one side only for clarity).

Li et al. (2011), however, in a later paper proposed a revised dynamic vortex model which can be seen in figure 2.7(b). They labelled the secondary vortices arising from the trailing edge as the *first secondary vortices*. In their numerical study, they found that these two vortices merge with the primary vortex. The *second secondary vortex* is a newly generated vortex under the primary streamwise vortex. This secondary vortex is independent of the first secondary vortices. This dynamic vortex model has also been confirmed by Saad et al. (2012) in their experimental work. Sun et al. (2012) used tomographic Particle Image Velocimetry (3-dimensional) and showed that the mean flow displays a streamwise wake region coming

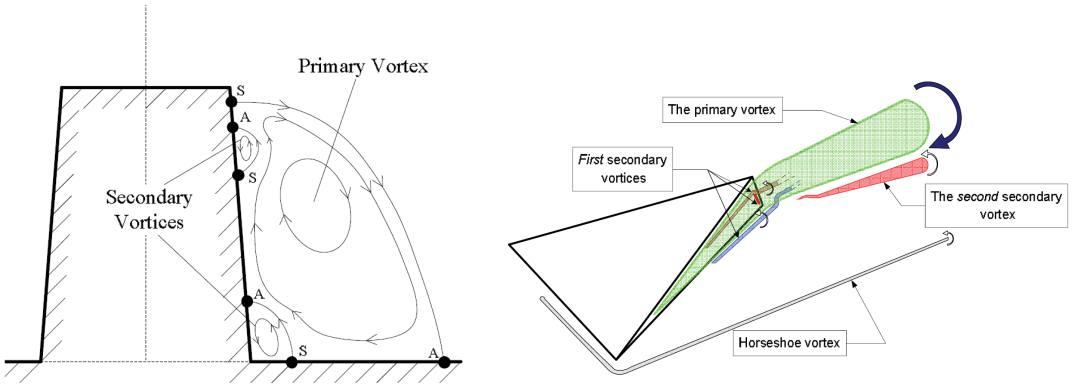

(a) The cross-section separation pattern near TE. **S** denotes separation and **A** denotes re-attachment(Li et al. (2011)).

(b) Revised Vortex Model by Li et al. (2011).

Figure 2.7: Separation location and vortex flow structure for secondary vortex as proposed by Li et al. (2011).

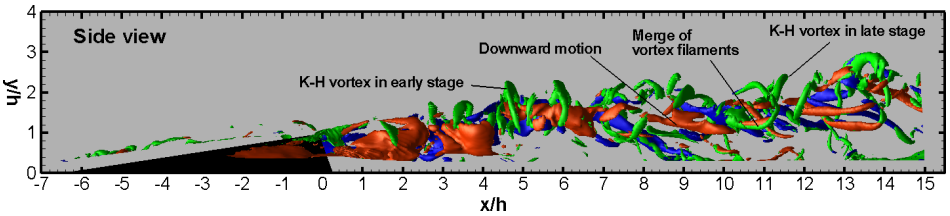

Figure 2.8: Side View of Vortical Field (Sun et al. (2013)).

from the trailing edge of the micro-ramp. The counter-rotating vortex pair is contained within the wake region. Both the wake and the vortices lift up when moving downstream.
In the instantaneous measurements, the flow exhibits features which are significantly different from mean flow organization. Kelvin-Helmholtz instabilities produce a train of arc-shaped vortices in the shear layer around the wake. The K-H vortices are not visible in the mean flow due to averaging process. Even the two primary vortices are not symmetrical in instantaneous measurements and exhibit undulating behaviour as observed by Sun et al. (2012). The K-H vortices influence the streamwise vortices as can be seen in figure 2.8. The streamwise vortex filaments, in the locations where K-H vortices were produced, tend to show a vertically downward motion and a laterally outward motion which merged with the feet of K-H vortices. Yan et al. (2014) showed similar flow structures in their LES studies. Liu et al. (2013) also investigated the vortical structures in the wake region of a micro-ramp in a supersonic boundary layer. In the wake of the micro-ramp, a momentum deficit exists surrounded by a curved shear layer which generates the arch shaped K-H vortices. Using the vortex-line method, they proposed that the small-scale vortices in the near-wake of micro-ramp take an Ω shape and wrap the low momentum region as shown in figure 2.9 (also shown in red in figure 2.10), suggesting that these structures receive vorticity from the viscous interactions near the wall. Further downstream of the micro-ramp, the Ω-shaped vortices show an extended leg stretching upstream (green and black in figure 2.10) , which implies that these vortices get

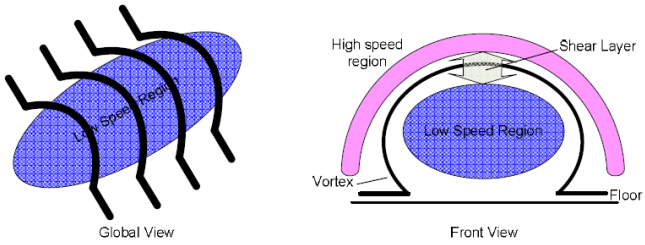

Figure 2.9: Conceptual model of flow topology as proposed by Liu et al. (2013).

the energy from primary streamwise vortices.

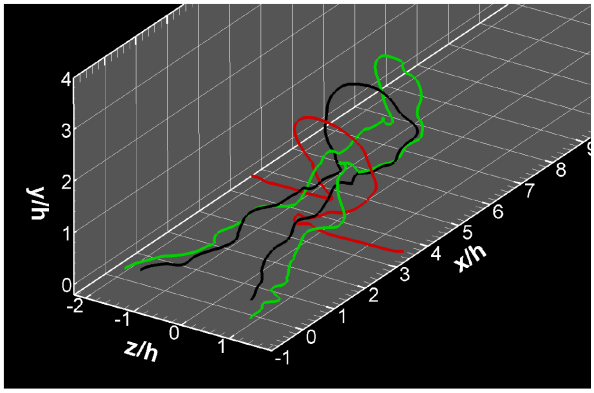

Figure 2.10: Vortex lines in the micro-ramp wake (Liu et al. (2013)). '0' on x-axis denoted the trailing edge of the micro-ramp.

Figure 2.11 shows the PIV and LES wake profiles obtained by Sun et al. (2013). It can be seen that the wake location, i.e. the location of minimum u in the profile keeps moving away from the wall as the flow moves downstream. It can also be seen that the minimum u at $x/h = 10$ is approximately $0.64U_\infty$ where as at $x/h = 14$, it is approximately $0.70U_\infty$, thus showing that the velocity deficit in the wake gets smaller downstream. A stronger vortex in the low momentum region will give a higher vertical velocity to the flow. The wake location gives the approximate height of the center of the low momentum region existing in the wake (Babinsky et al. (2009)). Upwash strength and wake location, in addition to incompressible shape factor, are important parameter in measuring the effects of micro-ramp.
Sun et al. (2013) measured the streamwise evolution of circulation (Γ) behind the micro-ramp. Also, the ESDU technical report 93024 (1995) suggests the following simple equation for the decay of vortex strength downstream of a vortex generator's trailing edge:

$$\frac{d\Gamma}{dx} = -KC_f\frac{\Gamma}{h_v} \tag{2.8}$$

where K is a constant depending on the type of vortex generator used, C_f is local skin friction coefficient in absence of device and h_v is the height of the vortex core.
Ashill et al. (2011) categorized the vortex strength in subsonic flow by calculating the circulation Γ in the wake region and showed that the circulation at a particular streamwise position scales with the wall friction velocity u_τ and the device height h. For counter-rotating devices,

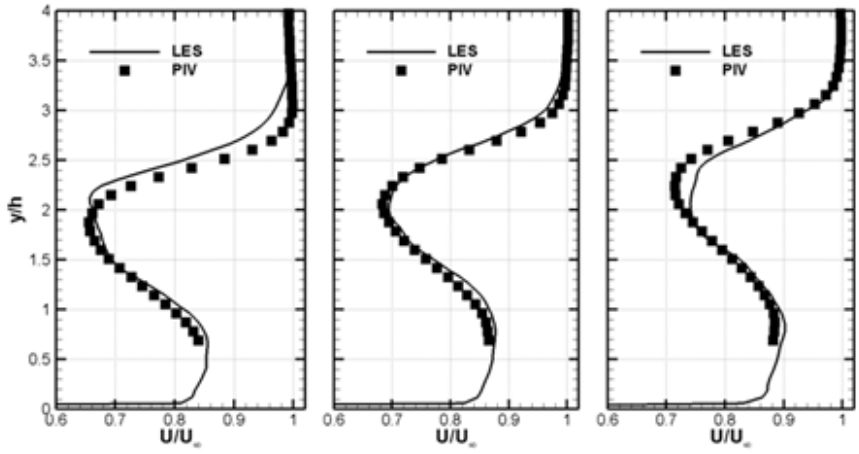

Figure 2.11: Profiles of u within the center plane: (a) x/h=10 (b) x/h=12 (c) x/h=14 (Sun et al. (2013)).

he defined circulation as the arithmetic mean of the absolute values of the vortex circulations on either side of the geometry. He deduced that the circulation around one of the vortices in streamwise location correlates with the device height by the relation

$$\frac{\Gamma}{u_\tau h} = f(h_e^+) \tag{2.9}$$

where u_τ is the wall friction velocity in absence of device and $h_e^+ = \frac{u_\tau h_e}{\nu}$ is the effective device Reynolds number using effective device height. For micro-ramps, the effective device height is the actual micro-ramp height. They used the concept of effective device height to normalize the device heights of other micro actuators with the micro-ramp height such that the circulation change falls on the same curve, as shown in figure 2.12.[1] Above the critical device Reynolds number ($h_e^+ \approx 1500$), it was seen that the circulation scaled linearly with device height h and u_τ. For the vortex generators with the device Reynolds number less than the critical Reynolds number, the circulation was less than the constant non-dimensionalized circulation at higher h_e^+.

Nolan in his PhD thesis (Nolan (2013)) has suggested a modeling method for upwash using inviscid Lamb-Oseen vortex model (Saffman (1992))

$$u_\theta(r) = \frac{\Gamma}{2\pi r}\left[1 - \exp\left(-1.256\frac{r^2}{r_c^2}\right)\right] \tag{2.10}$$

where Γ is the circulation contained in the vortex, r is the the distance from vortex center and r_c is the core radius of the vortex. Since the vortices modeled were near the floor, interference effects were expected and hence a mirror vortex was used to simulate a solid wall with no

[1] Effective height for a forward wedge is taken as a datum. The effective height of other devices was then selected by ensuring that the maximum value of non-dimensional circulation based on effective height becomes independent of the device geometry.(Ashill et al. (2011))

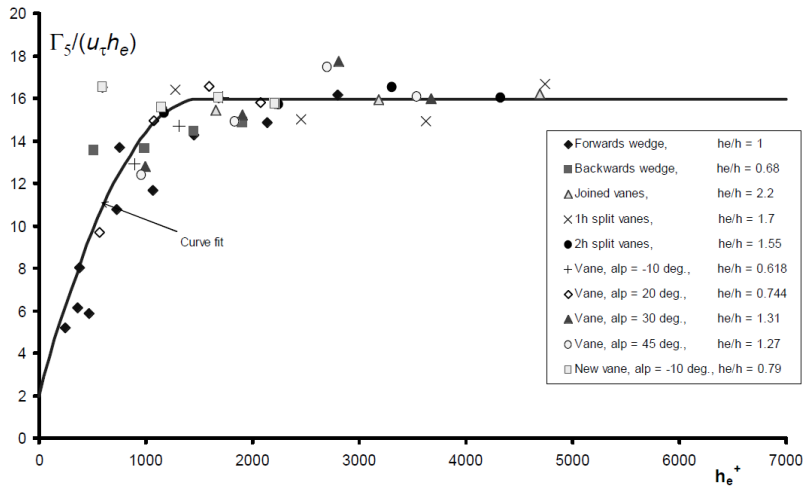

Figure 2.12: Generalised correlation of vortex strength against Reynolds number based on device effective height (Ashill et al. (2005)).

wall-normal velocity. First, the initial estimates of the vortex parameters (Γ, r_c) and vortex locations (y_v and z_v) are made. In the second step, the velocity field is calculated from the vortex model at two different spanwise locations (figure 2.13(a)) and then a sum of the velocity fields is used to account for their superposition in the VG model. As a third step, he suggested to subtract the corresponding modeled velocities from the experimental data (figure 2.13(b)) at the spanwise locations. The mean of the resulting values estimates the bulk flow, which acts as a constraint in the model. Finally, the bulk flow can be subtracted from the experimental data and compared with vortex model. The steps are repeated with changing the vortex parameters until a best fit is found as in figure 2.13(b).

The inviscid vortex modeling, as defined by Nolan (2013), can be used as a good starting point to get estimates of the vortex circulation.

2.3.2 Micro-ramp height effects

Babinsky et al. (2009) showed that the low-momentum wake deficit region behind the micro-ramp scales with device height (heights from 30-90% of boundary-layer thickness). No fundamental change in flow structures was observed by changing micro-ramp height and the flow development is similar in all cases, as can be seen in figure 2.14. The low momentum region, in each case, gradually moves upward as one moves to a downstream section. However, the rate at which the low momentum region moves upwards depends on the device height, as evident from the figure. The largest ramp size had the strongest effect in giving a fuller velocity profile, but it also incurred the greatest drag (assumption from the larger wake size). The smallest device height was able to have almost similar beneficial effects without incurring significant device drag. Lee et al. (2007) from LES and RANS simulations also concluded that smaller micro-ramps produced less disturbances in the flow resulting in thinner displacement thickness.

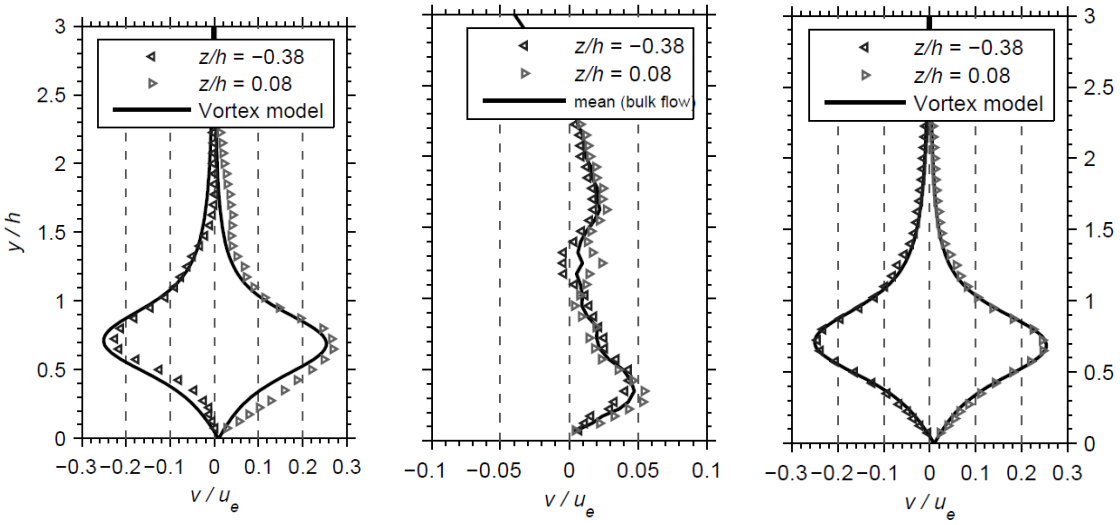

(a) Comparison of experimental data and vortex model.

(b) Vortex model subtracted from data.

(c) Bulk flow subtracted from data.

Figure 2.13: Vortex Generator wake model as reported by Nolan (2013).

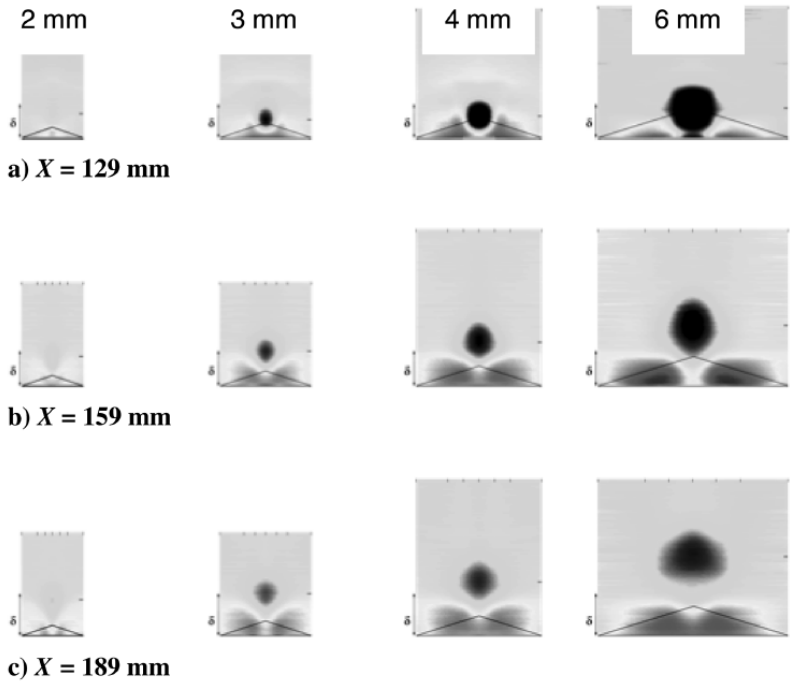

Figure 2.14: Streamwise momentum deficit at various downstream locations fo micro-ramps of different heights (Babinsky et al. (2009)).

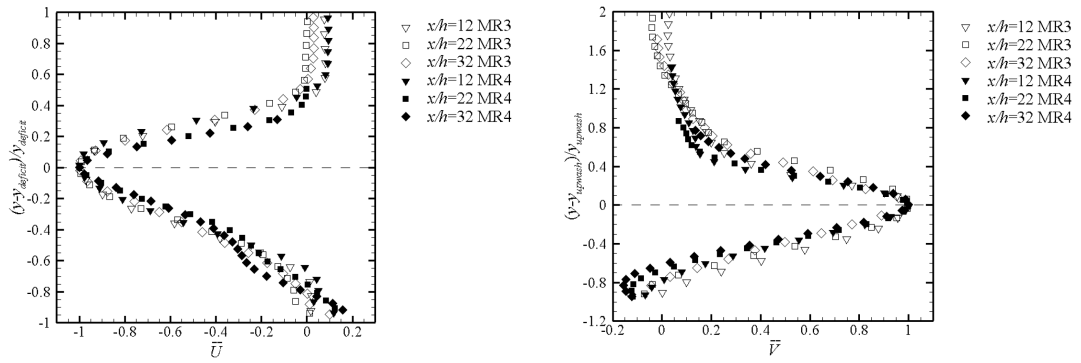

(a) Normalized deficit velocity profiles.

(b) Normalized upwash velocity profiles.

Figure 2.15: Self-similar profiles as reported bu Sun et al. (2014).

Sun et al. (2014), as discussed in previous section, observed that the momentum deficit region in the wake of the micro-ramp moves away from the wall non-linearly with respect to distance behind the micro-ramp. As the flow moves downstream, the vortex strength decreases (resulting in decreased upwash) and hence the rate of lift-off of the momentum deficit region also decreases. They also reported power law fits for the decay of the velocity deficit as shown by equation 2.11 and for the decay of maximum upwash velocity, as given in equation 2.12.

$$\frac{U_{\min}}{U_\infty} = 1 - 2.1\left(\frac{x}{h}\right)^{-0.73} \qquad (MR-3mm) \tag{2.11a}$$

$$\frac{U_{\min}}{U_\infty} = 1 - 2.2\left(\frac{x}{h}\right)^{-0.78} \qquad (MR-4mm) \tag{2.11b}$$

$$\frac{V_{\max}}{U_\infty} = 20\left(\frac{x}{h}\right)^{-1.7} \qquad (MR-3mm) \tag{2.12a}$$

$$\frac{V_{\max}}{U_\infty} = 25\left(\frac{x}{h}\right)^{-1.6} \qquad (MR-4mm) \tag{2.12b}$$

Sun et al. also reported that the velocity profiles at their test conditions of Mach 2.0 and $Re_\theta = 13600$ are self-similar, as shown in figure 2.15. For streamwise component, the normalized parameters are given in equation 2.13

$$\overline{U}(y) = \frac{U(y) - \overline{u}_{BL}(y)}{\Delta U_{deficit}} \tag{2.13a}$$

$$\overline{y} = \frac{y - y_{deficit}}{y_{deficit}} \tag{2.13b}$$

where $\overline{u}_{BL}$ is the undisturbed boundary layer velocity, $\Delta U_{deficit}$ is the difference between the minimum velocity and the undisturbed boundary layer velocity existing at the location $(U_{min} - \overline{u}_{BL}(x, y_{deficit}))$, and $y_{deficit}$ is the location of maximum deficit. Similarly, for the

wall-normal velocity, the normalization parameters are given in equation 2.14

$$\overline{V}(y) = \frac{V(y)}{V_{max}} \tag{2.14a}$$

$$\overline{y} = \frac{y - y_{upwash}}{y_{upwash}} \tag{2.14b}$$

where V_{max} is the peak upwash value and y_{upwash} is the location of the maximum upwash. Their results, thus, show that at the same Mach number and Reynolds number, the flow features are similar and scale with the height of the micro-ramp.

Giepman et al. (2013) conducted experiments to investigate the effects of micro-ramp height on the size of shock-induced separation bubble and the unsteadiness of the reflected shock. They used planar PIV and the results obtained are compared with Babinsky's (Babinsky et al. (2009)) results in Figure 2.16. The wake location obtained by Giepman et al. and by Sun et al. (2014) for different device height agree with each other but differ slightly from Babinsky et al. (2009)'s and Nolan and Babinsky (2011)'s results.[2] There might be two reasons to this difference. The main reason, probably, is the difference in the Mach number (M=2 for Giepman et al., M=2.5 for Babinsky et al. and M=1.5 for Nolan et al.) for the experiments. Another factor might be the fact that Babinsky's curve is a best-fit curve on wake location data with different micro-ramp heights (hence different $\frac{h}{\delta_{99}}$) based on values obtained at three downstream locations. The results by Lee and Loth (2011) are quite different probably because the LES code was not able to resolve all the turbulence scales existing in the undisturbed flow. Also, the Re_θ for them was quite low compared to the experiments. Giepman also found that the minimum distance required between the micro-ramp and SWBLI to reduce shock induced separation was independent of the micro-ramp height and instead scaled with the boundary layer height which is contrary to Babinsky's hypothesis that the minimum distance depends on device height.

2.3.3 Mach number and Reynolds number effects

Effects of Mach number have been investigated by Lee and Loth (2011) using Large Eddy Simulation and by means of oil flow visualization. At higher Mach number there is a higher density variation in the wake which is consistent with the increased compressibility effects at wider Mach range (from no slip at boundary to freestream at specified Mach number). At the lower Mach number of M=1.4, as shown in figure 2.17 , the flow reaches higher velocities (relative to freestream velocity) close to the wall earlier than the M=3.0 case. This happens because the flow spills on the sides of the micro-ramp, due to low pressure at the side edges (because of separation at the micro-ramp edges). For lower Mach number, due to the modest freestream velocity (and hence larger subsonic region in the boundary layer profile) and higher wave angle, the information on the micro-ramp sides is easily communicated upstream to the ramp surface. It, thus, sends the information of the pressure change at the sides of the micro-ramp to the flow upstream, causing the flow to become more parallel with the freestream and thus accelerate.

[2]Wake locations from Nolan and Babinsky (2011) are approximated from the contour plots and hence the error bars.

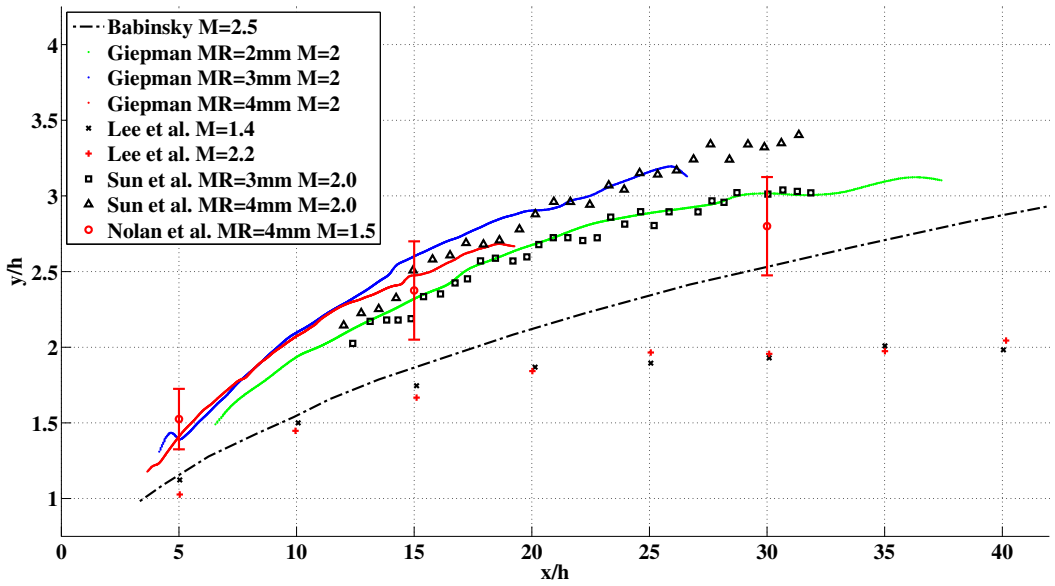

Figure 2.16: Comparison of location of wake, as reported by Babinsky et al. (2009) (M=2.5 $Re_{\theta_{inc}}$=28.8x10^3), Giepman et al. (2013)(M=2.0 $Re_{\theta_{inc}}$=21.8x10^3), Lee and Loth (2011) (M=1.4,2.5 $Re_{\delta*}$=3.8x10^3), Sun et al. (2014)(M=2.0 $Re_{\theta_{inc}}$=20.2x10^3) and Nolan and Babinsky (2011)(M=1.5 $Re_{\theta_{inc}}$=18.2x10^3).

Figure 2.18 shows the oil flow visualisation images from Herges et al. (2010) and Babinsky et al. (2009) compared with instantaneous streamlines computed by Lee and Loth (2011). As discussed in previous paragraph, it can be seen that for the lower Mach number case, the flow starts turning earlier and slightly upstream of the ramp leading edge due to better upstream communication of information from the subsonic region of the boundary layer. At lower speeds, the vortices tend to roll up tightly along the edge, as shown in figure 2.18c creating an hourglass kind of feature, as shown by the arrows. It was shown that at lower speed vortices have more time to curl up and rotate for the same given distance. This can also be observed by comparing the results by Babinsky et al. (2009), Nolan and Babinsky (2011), Sun et al. (2014) and Giepman et al. (2013), as shown in figure 2.16. The wake locations for higher mach number (M=2.5) by Babinsky is lower when compared to the results by Giepman et al. and Sun et al. at Mach 2.0. The wake location obtained by Nolan and Babinsky (2011) at M=1.5 is also higher than those obtained by Babinsky et al. at M=2.5, which confirms the affects of Mach number on wake locations.

Nolan (2013) measured the circulation strength for micro-ramps at different Mach numbers. The non-dimensional circulation showed a slight decrease with increase in Mach number as can be seen in figure 2.19(a). The vortex core radius showed a slight decrease with increasing Mach number at the same downstream location. An increase in Mach number slightly lowered the height of the vortex core y_v for same x-location, as can be seen in figure 2.19(b). It can also be seen from the figure that the primary vortex cores are closer spanwise for higher Mach number case. In his thesis, Nolan added a remark that there was no observable trend in the

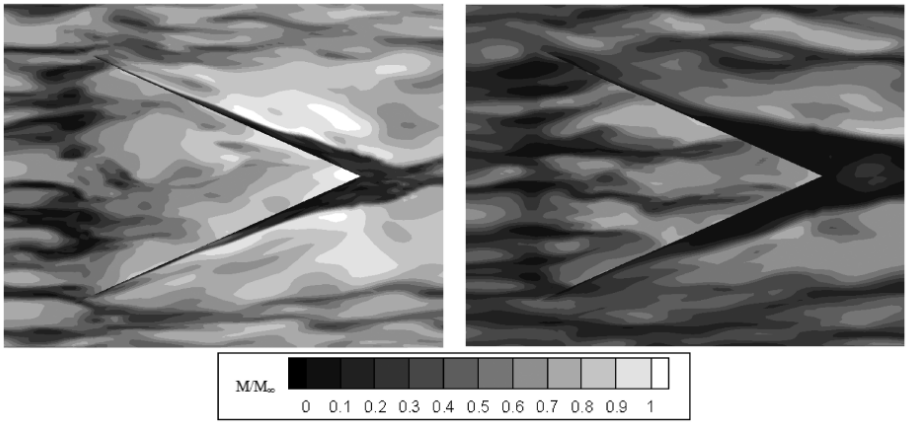

Figure 2.17: Mach contours of instantaneous LES flow solution at $y^+ = 12$ (above the floor and the top surface of the microramp) for M=1.4(left) and M=3.0(right). The streamwise (x) and the spanwise (z) extent of the figures range from -8.2h to 1.9h and -3.9h to 3.9h, respectively (Lee and Loth (2011)).

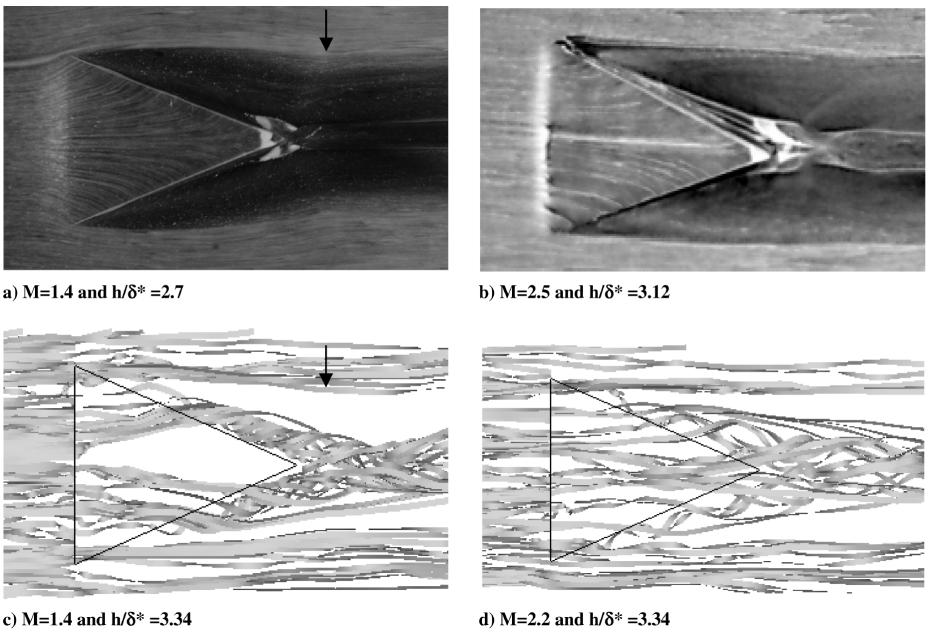

Figure 2.18: Oil flow visualisation (Herges et al. (2010),Babinsky et al. (2009)) images (top) and instantaneous streamlines of LES (bottom) from Lee and Loth (2011).

vortex parameters at x/h=5 due to the scatter in the data. Though the Mach number effects on vortex parameters were minor, it did have more influence on the skin friction in the flow behind the micro-ramp as can be seen in figure 2.20. The mean of the maximum velocity defect in both vortices did not show any discernible trend.

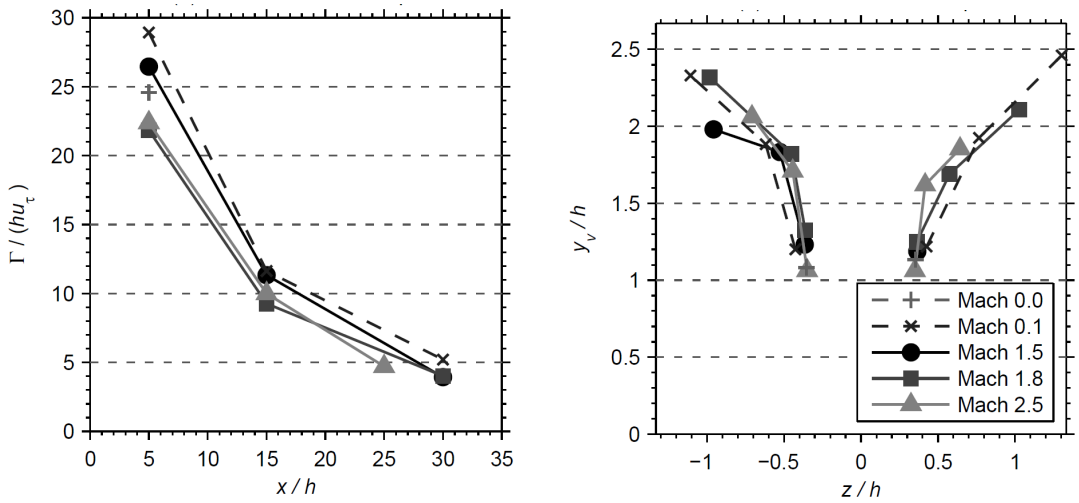

(a) Non-dimensional circulation in the micro-ramp wake measured at different Mach numbers.

(b) Vortex core trajectories behind micro-ramp at different Mach numbers. The x-locations of the measurement planes can be seen in 2.19(a).

Figure 2.19: Non-dimensional circulation and vortex core trajectories, as measured by Nolan (2013).

Not much work has been done to observe the Reynolds number effects on the flow behind the micro-ramp. The boundary layer thickness (δ_{99}) does change with Reynolds number. Hence, for the same micro-ramp at different Reynolds number, the $\frac{h}{\delta_{99}}$ ratio will be different. But at larger Reynolds number, the turbulent scales are smaller which could affect the instantaneous vortical structures downstream of the micro-ramp. Since this study will use planar PIV measurements, it will be very difficult to guess the 3D structures existing in the wake at different Reynolds number and whether or not they have an effect on mean flow field. However, it will still be of interest to report the effects in the mean 2D flow field at the center line behind the micro-ramp so that it can act as a reference for future studies.

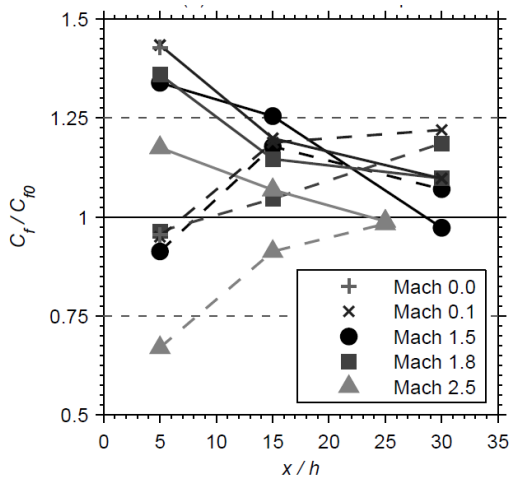

Figure 2.20: Downstream development of $\frac{C_f}{C_{f0}}$ behind the micro-ramp (Nolan (2013)). C_{f0} is the skin friction coefficient for undisturbed boundary layer. Solid lines are the arithmetic mean of the traverses at the spanwise location of vortex induced downwash; dashed lines are along the center where the vortices induce common upwash. The x-locations of the measurement planes can be seen in 2.19(a).

2.4 Synopsis

As explained in the previous section, micro-ramps can be used to introduce high momentum fluid in the near wall region by the action of two streamwise primary vortices. A rear view of the micro-ramp wake reproduced from Sun (2014) is shown in figure 2.21. An upwash is present along the center line, due to the primary vortices, which transports the low momentum fluid away from the wall. The downwash by the vortex, on the other hand, entrains high momentum fluid towards the wall. This transfer of momentum gives a fuller velocity profile to the region close to the wall. This high momentum fluid near the wall can overcome larger adverse pressure gradients due to shocks and can, hence, mitigate shock wave induced boundary layer separations.

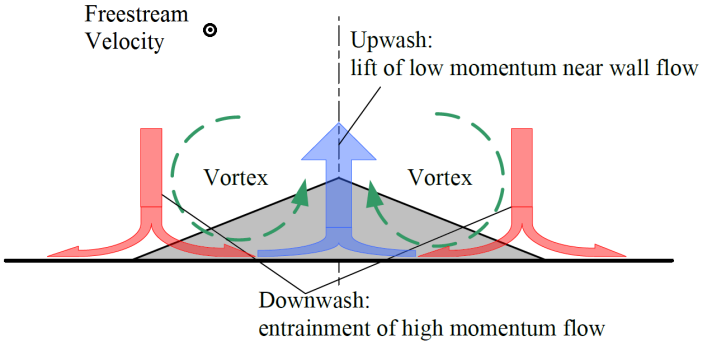

Figure 2.21: Rear view of the micro-ramp wake. Freestream velocity is out of the plane Sun (2014).

The effects of changing micro-ramp heights has been categorized well by different researchers (Babinsky et al. (2009); Giepman et al. (2013); Ashill et al. (2011); Sun (2014)). Although, not much work has been done to categorize the effects of changing Reynolds number, research carried out by Nolan (2013) has shown that Mach number does have an influence on the micro-ramp's wake. The experiments on micro-ramps are being carried out in different test facilities all over the world. Also, as explained in the introduction, industrial use of micro-ramps is not limited to a fixed Mach number or Reynolds number. Therefore, it is pertinent to introduce the main research question which is:

> "Determine the influence of micro-ramp height, the freestream Mach number and the Reynolds number on the flow field downstream of a micro-ramp and report and explain the trends that are observed"

In the course of this thesis, change in the span-wise gap between the primary vortex cores with Mach number is estimated by observing the vortex footprints from oil flow visualization. Parameters like wake location, upwash strength and wake velocity deficit along the center line are extracted from the mean velocity profiles obtained through planar PIV measurements at different test conditions. The research question is answered on the basis of results obtained from experimental measurements. The trends in the wake properties with changing test conditions are then reported and analysed.

Chapter 3

Experimental Arrangement

This chapter contains the description of the experimental instruments and techniques, starting with a description of the experimental flow facility followed by the description of the micro-ramp geometry used for this study. An outline of the working principles and the experimental considerations for planar PIV is then provided in section 3.3. It is followed by a brief description of oil flow visualization technique in section 3.4. Finally, section 3.5 lists the test-matrix for the current study.

3.1 Flow Facility

All experiments were performed in the blow-down transonic-supersonic wind tunnel (TST-27) of the High Speed Aerodynamics Laboratory at Delft University of Technology. A schematic of the experimental facility is shown in figure 3.1. The flow direction is from left to right. The throat can be varied by using an electrical motor which also varies the contraction part of the tunnel to set the Mach number. The flexible plate is shown in black and it moves to give a smooth surface from the throat to the test section. The facility generates flows in the Mach number range 0.5-4.2, in a test section of maximum dimensions 280mm(W)x270mm(H), and exhausts through the outlet diffuser to atmospheric pressure. The tunnel operates at unit Reynolds numbers typically ranging from $30\text{x}10^6$ to $130\text{x}10^6$.

The stagnation or settling chamber of the tunnel is connected to an external 300 m^3 vessel at pressures within the range of 20-40 bars. The air is delivered by a computer controlled compressor plant and is dried by a high-pressure dryer. To remove small particles from the air, there is a 5 μm dust filter present between the vessel and the settling chamber. A fully charged vessel contains approximately 14,300 kg of air. The tunnel can be operated continuously or intermittently till the total pressure of the pressure vessel drops below 20 bars. Hot wire measurements by Giepman et al. (2014) found that the RMS level for mass flux was 1.39% of $\rho_\infty U_\infty$, for $M_\infty = 1.7$ which is acceptable for the current experiments. The

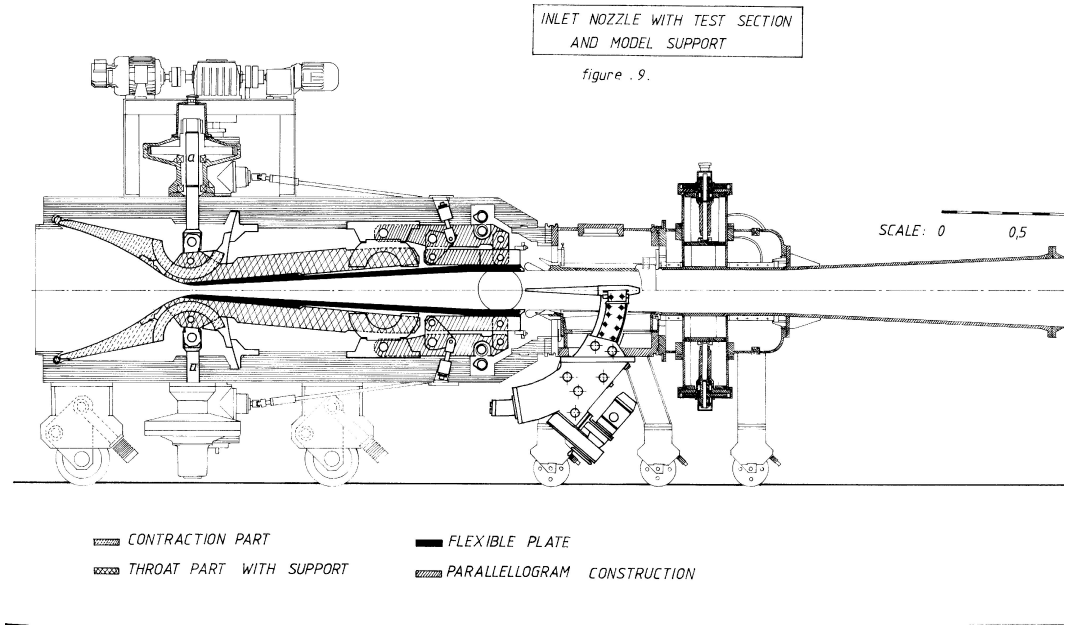

Figure 3.1: TST-27 Cross Section with variable throat and moving walls highlighted in black. (Reproduced with permission from Ing. F.J. Donker Duyvis).The model shown in the test-section is for illustrative purpose and is not related to current experimental set-up.

turbulence intensity also varies with Mach number and Reynolds number.

A seeding rake is also present in the settling chamber consisting of multi-orifice distribution pipe as shown in figure 3.2(a). The seeding rake is positioned in its most upward position so that maximum seeding is available near the tunnel upper wall where the micro-ramp was fixed. The position of rake in the settling chamber is shown in figure 3.2(b).

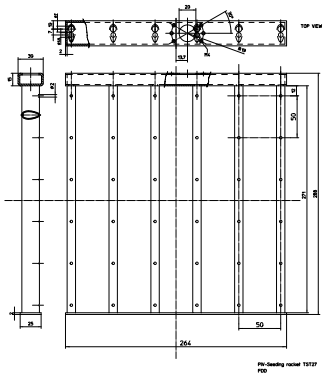

(a) PIV Seeding rake used in the experiments.

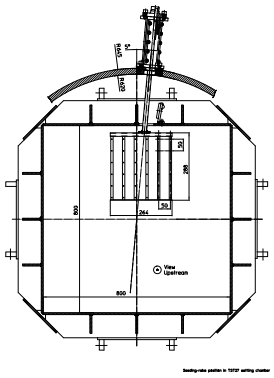

(b) Seeding rake in rised position in the stagnation chamber of TST27. The flow direction is normal to the surface coming outwards.

Figure 3.2: Seeding rake schematic in the wind-tunnel.

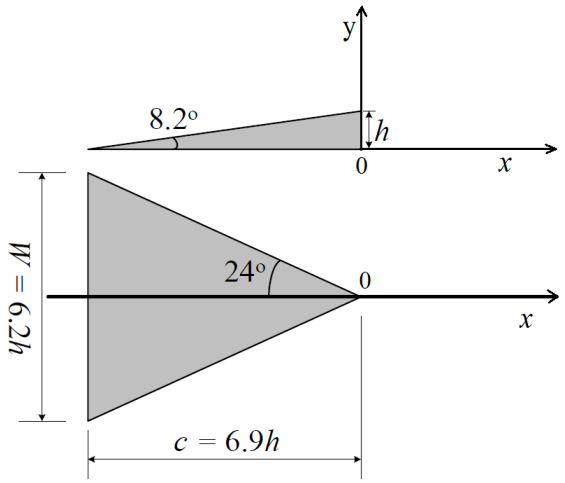

Figure 3.3: Micro-ramp used for the experiments.

3.2 Micro-ramp Geometry

The micro-ramps that are investigated in the current experimental study follow from the works of Anderson et al. (2006). The half span angle is $\alpha = 24°$ and the chord length is $c = 7.5h$. A schematic of the micro-ramp along with the axis definition, is shown in figure 3.3[1]. The locations are measured with the origin at the trailing edge of the micro-ramp. Micro-ramps of three different heights have been used in the course of this experiment with h =6mm, 8mm and 10 mm. The micro-ramps were fixed on the upper wall of the test section.

3.3 Particle Image Velocimetry

In this section, the basics of PIV experimental technique is explained, followed by a discussion on the experimental set-up used for this experiment. It is then succeeded by an explanation of the image pre-processing that was applied on the raw images.

3.3.1 Working Principles

Particle Image Velocimetry is a non-intrusive method to provide a quantitative description of the instantaneous flow characteristics in a flow field. The working principle is based on suspending tracer particles in the fluid flow, which do not affect the fluid properties. Quantitative velocity field data can then be obtained when these particles are illuminated by monochromatic light sheets, usually created by pulsed lasers. Successive photographs are made of the

[1]Based on schematic given by Sun (2014).

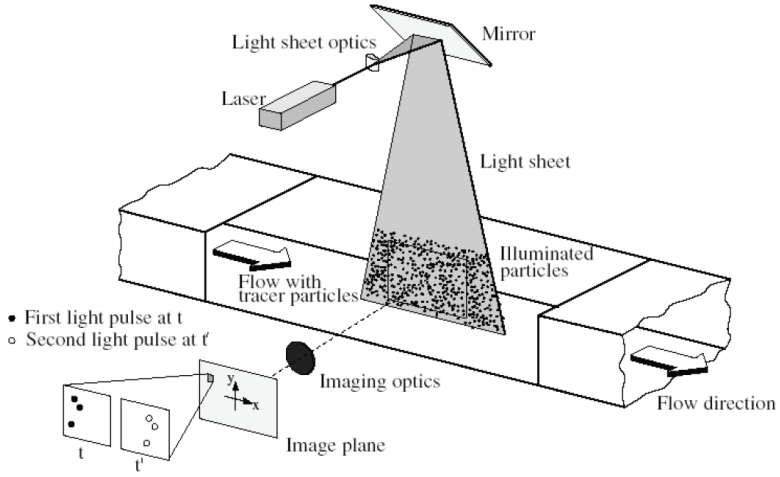

Figure 3.4: Theoretical PIV setup (Raffel (2007)).

scattered light emitted by particles in the seeded flow. From these captured images the particle displacement field over the short time separation is deduced through cross-correlation of the image data. Upon dividing the particle displacement field with the time separation, the velocity field is eventually attained. The theoretical PIV setup is shown in figure 3.4.

Tracer Particles

The tracer particles should have a low time lag so that the particle velocity is nearly equal to the actual velocity field. The relative particle velocity $(u_p - u_f)$ is related to instantaneous particle velocity u_p by the equation 3.1

$$u_p - u_f = \frac{2}{9}\frac{r_p^2(\rho_p - \rho_f)}{\mu_f}\frac{du_p}{dt} \tag{3.1}$$

where r_p is the tracer particle radius, μ_f is the viscosity of the fluid and ρ_f and ρ_p are the fluid and seeder particle density respectively. Since in gas flows the particle density is of $O(10^3)$, to get negligible relative velocity, particles of small radius are employed. The accuracy of the tracer particles in turbulent flows can be quantified by particle Stokes number S_k defined as the ratio of particle response time τ_p to characteristic flow time scale τ_f. The particle response time is the time in which the particle velocity can change to 63% $(1 - e^{-1})$ of the instant step variation (ΔU_f) in the flow velocity. The DEHS (Di-Ethyl-Hexyl-Sebacat) particles have a τ_p of 1.92-2.03 μs as measured by Ragni et al. (2011) through an oblique shock wave, inclined at 37.2° at Mach 2.0. For a turbulent boundary layer, the flow characteristic time τ_f can be expressed as $\tau_f = \frac{\delta_{99}}{U_\infty}$.

For seeding the flow, DEHS was used. Di-Ethyl-Hexyl-Sebacat (DEHS) is a non-soluble, colourless and odourless liquid which is suitable for producing steady aerosols. The particle size is below 1 μm with a droplet of 0.3 μm having a life time of 4 hours. After 4 hours DEHS evaporates completely. PIVTEC Aerosol Generator PivPart45 (shown in figure 3.5(a)) was used to generate the seeding with a maximum overpressure setting of 5 bars.

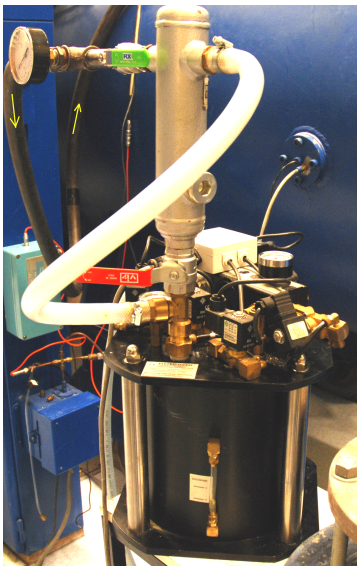

(a) Seeding Generator used for the experiment. The black pipe(yellow arrows for visibility) leads the tracer particles to the seeding rake in the settling chamber.

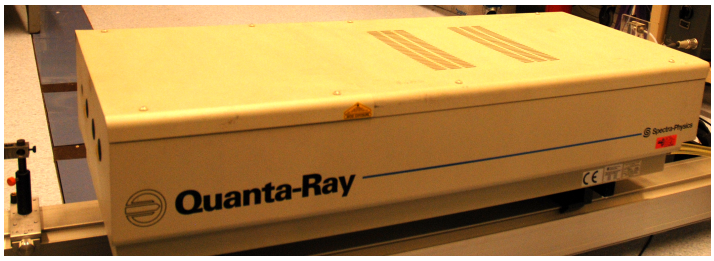

(b) Spectra Physics Quanta-Ray laser used for the experiment.

Figure 3.5: Seeding generator and Laser.

Laser

Spectra Physics Quanta-Ray double pulsed laser was used for the current experiment and is shown in figure 3.5(b). It is a Nd:YAG laser equipped with frequency doubler to emit laser light with wavelength $\lambda = 532nm$. The green laser has a pulse duration of 7 ns with a maximum repition rate of 10 Hz. The laser was combined with a set of mirrors and lenses to give a diverging laser sheet in the test section. The laser sheet had a width of 1.5mm in the middle of the test section.

Camera

The images were captured using four Imperx Bobcat IGV-B1610 cameras. The specifications of the camera are given in the table below: The cameras had a maximum acquisition rate

Table 3.1: Specifications of Imperx Bobcat IGV-B1610 2.0 megapixel camera.

Amount of pixels	1628 x 1236
Pixel size	4.40 μm
Sensor Type	1/1.8" CCD
Maximum Frame Rate	212 FPS
Shutter Speed	1/200,000 to 1/17 sec

of 5.1Hz in double frame operation with full field of view. The images were recorded using Davis 8.1 acquisition software. A 3-dimensional overview of the experimental set-up is given in figure 3.6. The relative positions of the cameras can be seen from the top-view of the set-up in figure 3.7.

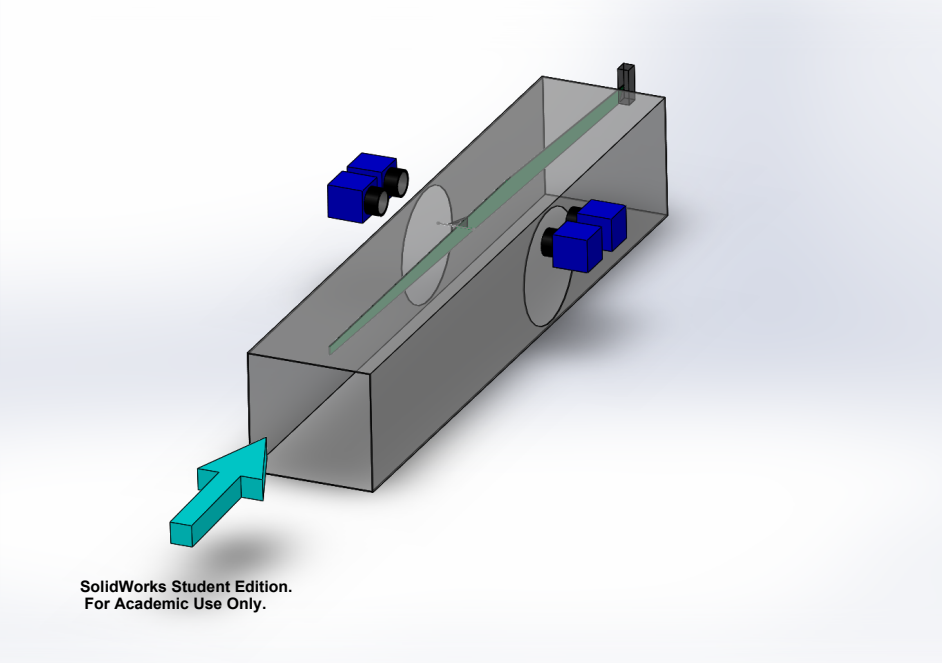

Figure 3.6: An overview of the experimental set-up. The flow direction is denoted by the blue arrow, the laser sheet is colored green and passes along the center-line of the micro-ramp. The laser sheet is introduced in the tunnel through a probe containing two cylindrical lenses and a mirror. The micro-ramp is mounted on the top horizontal wall.

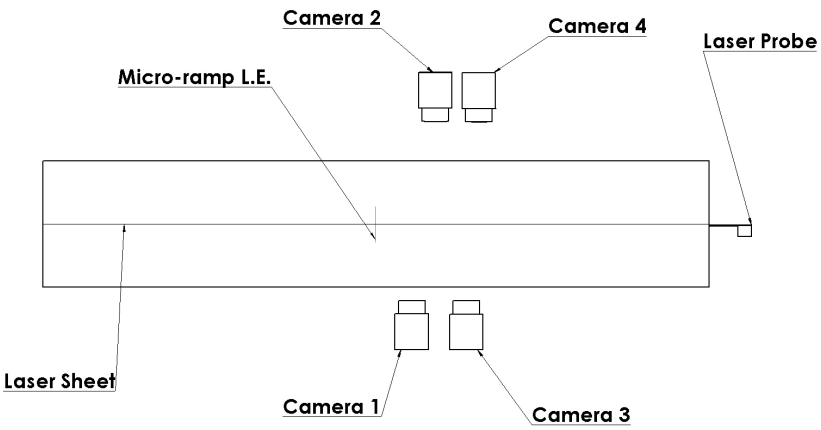

Figure 3.7: Top-view of the set-up. Flow direction is from left to right.

Magnification Factor and F-stop

The magnification factor (M) is a scaling factor which can be seen as the ratio between the sensor size and the imaged object size. Since knowledge of the amount of pixels and their size are available, this quantity is determined as:

$$M = \frac{pixel\ size\ \times\ \#pixels_{x-direction}}{FOV_{x-direction}} \tag{3.2}$$

For this experiment, the Resolution defined by equation 3.3 in mm/pixel is listed in table 3.2

$$Resolution = \frac{FOV_{x-direction}}{\#pixels_{x-direction}} \tag{3.3}$$

The f-stop ($f_{\#}$) of the camera is the ratio between the focal length of the lens (f) and the aperture diameter (D). Choosing the value for f-stop is not straight forward since it depends on multiple factors. These are:

- Depth of field, the range in which particles are imaged in focus: higher f-stop leads to a larger depth of field
- Diffraction, governs the particle image diameter: lower f-stop leads to lower diffraction and hence a smaller pixel radius for the particle
- Brightness, governed by the aperture diameter (D): lower f-stop leads to a brighter image due to a larger aperture diameter

Considering the above parameters, the $f_{\#}$ was chosen to be 8 for all the cameras.

Field of View

The field of view is the area that is captured by the camera and therefore this quantity depends on the investigated flow. For this experiment, the aim of the experiment was to capture the wake of the micro-ramp. The micro-ramp was mounted on the top wall of the tunnel. It was done because the seeding rake could only be put close to the top wall (figure 3.2(b)) and hence the flow near the top wall will have better seeding than the bottom wall. Since 4 different cameras were used, it was necessary to have an overlap between the four cameras so that the results from each camera could be stitched to give a full overview of the flow-field. The field of view for each camera is shown as a schematic diagram in figure 3.8. The field of view and their corresponding locations, along with the focal length of the camera lenses and the resolution, is given in table 3.2. For the undisturbed boundary layer cases and the 6mm micro-ramp cases, the images were cropped in y-direction to obtain a higher acquisition rate from the cameras.

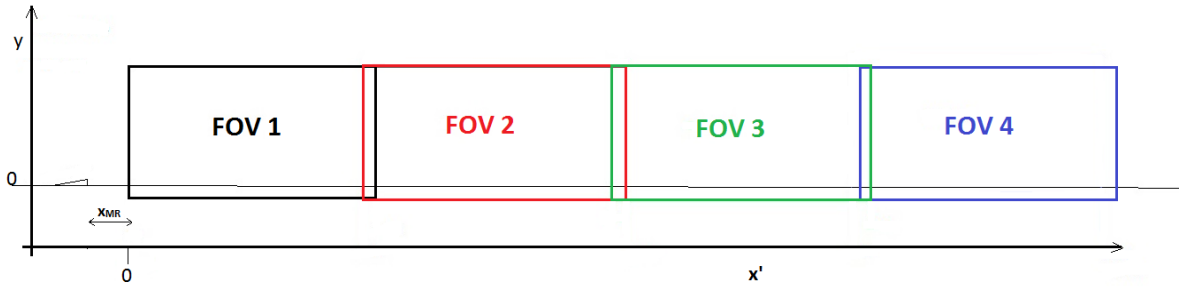

Figure 3.8: Schematic of the field of view for each camera. x_{MR} is the distance between micro-ramp trailing edge and the start of the first field of view. x' is the axis starting from the starting point of first FOV.

Table 3.2: Field of View Setup. Size in $pixel^2$, Lens focal length in mm, Resolution in mm/pixel and x' as shown in figure 3.8.

		Undisturbed	6mm MR	8mm MR	10mm MR
FOV #1	Size	1628 x 850	1628 x 1020	1628 x 1236	1628x 1236
	Lens	35	35	35	35
	$f_\#$	8	8	8	8
	Resolution	0.0331	0.0334	0.0336	0.0328
	x'	0-53.8	0-54.3	0-54.6	0-53.4
FOV #2	Size	1628 x 850	1628 x 1020	1628 x 1236	1628 x 1236
	Lens	50	50	50	50
	$f_\#$	8	8	8	8
	Resolution	0.0327	0.0346	0.0345	0.0347
	x'	46.7-99.8	44.3-100.5	48.5-104.6	43.7-100.2
FOV #3	Size	1628 x 850	1628 x 1020	1628 x 1236	1628 x 1236
	Lens	35	35	35	35
	$f_\#$	8	8	8	8
	Resolution	0.0332	0.0332	0.0333	0.0332
	x'	88.8-142.7	90.3-144.2	91.0-145.2	90.2-144.1
FOV #4	Size	1628 x 850	1628 x 1020	1628 x 1236	1628 x 1236
	Lens	50	50	50	50
	$f_\#$	8	8	8	8
	Resolution	0.0332	0.0349	0.0347	0.0350
	x'	133.6-187.6	130.1-186.8	136.3-192.8	129.9-186.8

3.3.2 Image Pre-processing

The obtained PIV images were converted from Davis' '.im7' format to '.h5i' format for 'Fluere'. 'Fluere' is an in-house PIV cross-correlation tool developed by Ir.K.P.Lynch at the faculty of Aerospace Engineering, TU Delft. The raw PIV images were pre-processed to get the best quality results from cross-correlation. The pre-processing steps are listed as follows:

- Rotation: The obtained images, if tilted, were first rotated to give a horizontal wall.
- Minima Subtraction: Minimum intensity levels for each pixel location over the complete set of images were identified and subtracted from each individual image pair, to remove background noise and get a cleaner raw image.
- Readout noise removal: The camera contains a constant fixed pattern read-out noise of the CCD chip. Giepman et al. (2014) lists the steps to remove this noise by transforming the camera image to frequency domain using Fourier transform. The background noise peaks are estimated from the frequency domain to be the locations outside the central peak region. These noise peaks are removed from the frequency domain and inverse Fourier transform is then used to get the original image with the read-out noise removed.

The raw image and the image obtained after processing are shown in figure 3.9.

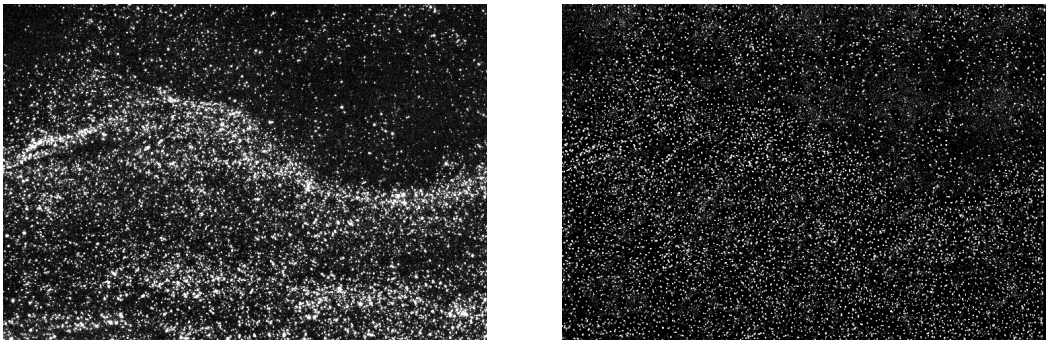

(a) PIV image before processing.

(b) PIV image after processing.

Figure 3.9: PIV Processing. Flow direction is from left to right.

3.3.3 PIV Considerations

For getting good results from PIV measurements, several factors need to be considered. This sub section lists the considerations taken into account to choose a good correlation window size, the pulse separation between the image pairs and the ensemble size to get a good mean flow result.

Correlation Window

The size of the interrogation window is an important aspect in getting good cross-correlation results. On the one hand, the size of the correlation windows should be small enough to give a high spatial resolution but the output vectors of small correlation windows are less stable and more prone to errors. To get good quality results, the correlation window should contain reasonable number of particles (usually at least 9-10). However, on the other hand,

if large correlation windows are used, more reliable vectors would be obtained as output, but they will be averaged over more pixels, and hence there is a risk of losing information. The particle per pixel (PPP) levels in the images can be tested and used as a starting point for determining the window size.
In all the cases (except M3Re40) for undisturbed boundary layer, the PPP levels were close to 0.005 near the wall and approximately 0.01 in the free-stream, as can be seen in figure 3.10(a). The cases with micro-ramp also had similar levels of PPP in the free-stream, as can be seen in figure 5.6. Hence, a correlation window size of 128x32 pixels was chosen, which on average, will enclose 20 particles at PPP levels of 0.005. The window size was chosen to be shorter in y-direction because the aim was to capture the velocity profiles as accurately as possible, without introducing too much noise. To get good vector results, multi-pass sum of correlation with 75% overlap, was performed on all the undisturbed boundary layer cases. Sum of correlation technique was not useful in the cases with micro-ramps because it was difficult to get a good correlation peak in the highly unsteady wake region. Hence, for the cases with micro-ramp, single image pair cross-correlation was done to get instantaneous vector fields and then the vector field results were processed to give a mean velocity field.
For cases at Mach 3, the PPP levels observed were quite low, to the order of 0.001, as can

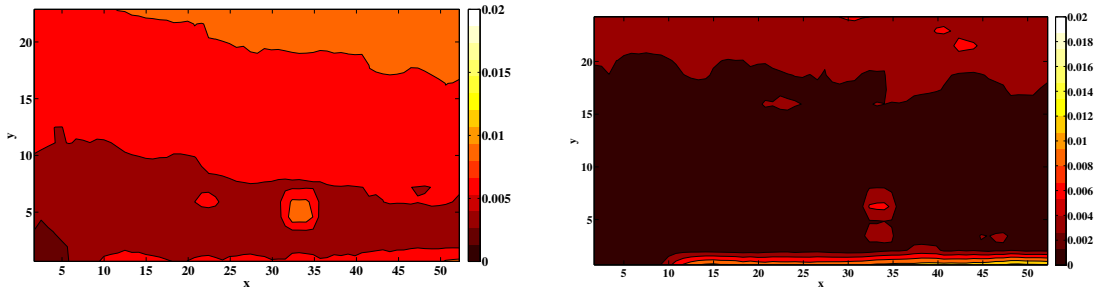

(a) Case M2Re28

(b) Case M3Re40

Figure 3.10: Particles per Pixel levels for two test cases (Using Camera 1).

be seen in figure 3.10(b). This was too low level to get any useful information and hence the cases at Mach 3 (M3Re40 and h8M3Re40) are not included in PIV results.

Pulse Separation

The pulse separation Δt is chosen such that:

- *the motion of the particles outside the measurement is minimized*;
  The laser sheet has a thickness of the order of 1.5mm. The out of plane motion should be limited to a fourth of the laser sheet thickness. Sun et al. (2012) at Mach 2 were used to approximate the out of plane velocity component, which was approximately $0.2U_\infty$. From the relation $\Delta t \leq \frac{\frac{1}{4}1.5e^{-3}}{0.2U_\infty}$ with $U_\infty = 500m/s$, the limiting pulse separation was 3.75 μs.

- *the pixel/pixel shear is* < 0.3;
  The main source of errors in PIV algorithms is linked to the width and maximum value of the correlation peak. If the particles in a correlation window have a very large velocity gradient, the correlation peak for each particle will be different and an average of the correlation functions for all particles in the window will cause the peak to become wider with a lower maximum value. If the displacements of two particles at a gap of Δy is Δx_1 ($=\Delta t u_1$) and Δx_2 ($=\Delta t u_2$), respectively, the displacement shear in pixels per pixel can be given by

$$\frac{\Delta x}{\Delta y} = \frac{\Delta t \left| u_1 - u_2 \right|}{\Delta y} \tag{3.4}$$

  A way to minimize this is to keep the particle displacements to such an order which keeps the pixel/pixel shear to be lower than 0.3 (Meunier and Leweke (2003)). Results by Sun et al. (2012) have been used to get an approximation of the Δt limited by the shear. The maximum $\frac{\Delta u}{\Delta y}$ was observed to be around 40000 s^{-1}. The maximum value of Δt which satisfies the given criteria was found to be 7.5 μs.
- *the relative error is as low as possible.*
  The PIV method is accurate to the order of 0.1 pixels. Thus, a larger pulse separation, and hence larger particle displacement will lead to a lower relative error in terms of pixel displacement.

Starting with the above observations and results, the pulse separation for the cases at Mach 1.5 and Mach 2.0 was determined to be 1.4 μs and for the cases at Mach 2.5 and Mach 3, it was determined to be 1.3 μs.

Ensemble Size

The ensemble size is the number of image pairs used when deriving a mean vector flow field in the cross correlation process. A large ensemble size gives a more converged result but it also requires a longer tunnel run-time. The test case M2Re40 was used to get to a proper ensemble size. A convergence criteria 'C' was used to ascertain the quality of results, which is defined as follows:

$$C(n) = \frac{\sigma([\overline{u}_i])}{\overline{u}_{300}} \qquad where \quad i = [n-10, n] \tag{3.5}$$

where $[\overline{u}_i]$ is a vector of mean velocities at a particular location from 'i' images and $\overline{u}_{300}$ is the mean from all 300 images. This criteria, essentially measures standard deviation of mean flow velocity obtained from n-10,n-9,...n image pairs at a fixed location in the measurement plane. For good convergence, the value 'C' will decrease with increasing ensemble size 'n'. Three y-locations ($0.15\delta_{99}$, $0.70\delta_{99}$ and $1.25\delta_{99}$) locations were identified in case M2Re40 to study the convergence of the mean velocity profile at a fixed x-location (60 mm from the start of the first FOV). Table 3.3 lists the values of 'C' obtained for these 3 locations. It can be seen from the table that the location outside the boundary layer, i.e., the free-stream location ($1.25\delta_{99}$) converges faster than the location close to the wall. It can also be seen that after a particular ensemble size 'n', in this case 125, the order of criteria 'C' does not change (though

Table 3.3: Criteria 'C' variation at 3 different y-locations with ensemble size 'n'.

Ensemble Size	$0.15\delta_{99}$	$0.70\delta_{99}$	$1.25\delta_{99}$
100	1.6E-03	4.1E-04	7.4E-05
125	7.6E-04	4.9E-04	1.9E-05
150	6.3E-04	7.2E-04	1.2E-05
200	4.5E-04	1.7E-04	1.7E-05
250	2.8E-04	1.1E-04	1.2E-05
300	3.2E-04	7.40E-05	1.4E-05

the exact values do not show a monotic decrease due to possible outliers around a particular value of 'n'). Hence, from this analysis it was determined that for the cases considered for this experiment, 150 image pairs should give good mean velocity field data.[2]

[2]For cases M2Re52 and M2Re64, 125 image pairs were used since some images were not good due to fluctuation of pressure levels during the start of the flow.

3.4 Oil Flow Visualization

Oil Flow visualization is used to determine the direction (not magnitude) of the velocity field on the wall. The working principal is based on the fact that a thin layer of viscous fluid like oil will move under the shear stress exerted by the air flowing over it. For this experiment, Shell oil 'Tellus 29' was used, mixed with TiO_2 grains to achieve the necessary viscosity. Few drops of Oleic acid were also added to act as an anti-coagulant. The wind tunnel wall was made black by sticking thin black sheet. The micro-ramp was also painted black. Before applying oil, a thin coat of Oleic acid was applied on the surface. Oleic acid makes the surface smoother to remove any small roughness on the surface which might influence the oil pattern.

The oil is a viscous medium and the velocity gradient in it is much smaller than air. Thus, the momentum equation for highly viscous flows like this reduces to a balance between pressure gradient and viscous forces. When the pressure gradient is small, the motion of the oil-layer indicates the direction of flow near the surface. However, when there is large pressure gradient, causing the flow to separate, the local shear stress vanishes and the oil layer moves due to the pressure gradient. This was also observed during the experiment as can be seen in figure 3.11. The oil flow pattern changes from the original pattern during the run (figure 3.11(a))

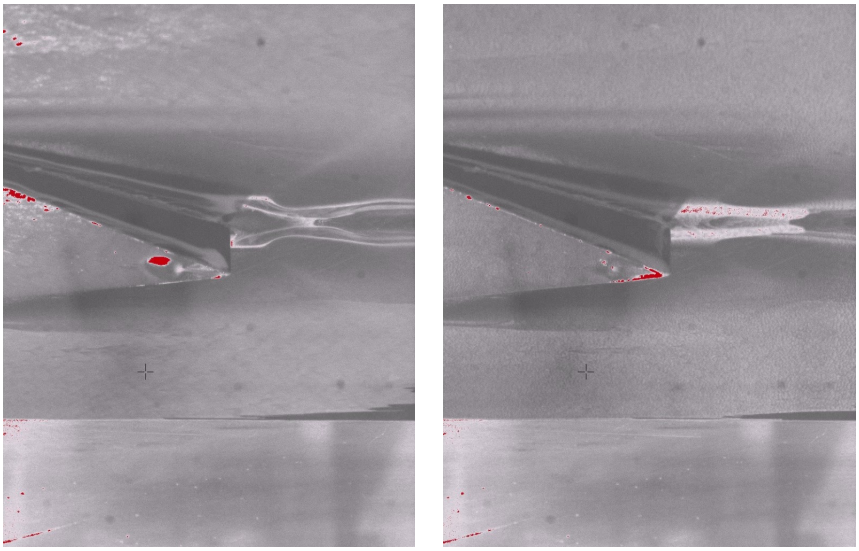

(a) Oil pattern during the run.

(b) Final Oil flow pattern after the tunnel is shut down.

Figure 3.11: Change in oil flow pattern as observed during the tunnel run. Flow direction is from left to right.

at the testing condition. When the valve between the pressure vessel and the stagnation chamber is closed, a compression shock runs through the tunnel. This pushes the oil trapped in the separation region near the micro-ramp edges to modify the pattern, as shown in figure 3.11(b). However, this effect is very small and the general features of the surface flow remain preserved to give useful qualitative insight.

3.5 Test Matrix

To get useful information about the effects of varying micro-ramp height, Mach number and unit Reynolds number, the campaign was divided into three test objectives.
First objective was to test the effects of varying micro-ramp height at a fixed Mach number and unit Reynolds number as shown in table 3.4[3]. x_{MR} is the distance between the micro-ramp trailing edge and the start location of the first field of view.

Table 3.4: Test matrix for varying micro-ramp height, at fixed Mach number and unit Reynolds number.

Exp. No.	**Case Designation**	**Mach Number**	**Reynolds Number (Unit)**	**Micro-ramp Height (in mm)**	x_{MR} **(in mm)**	Δt **(in** μ**s)**
1	M2Re40	2.0	4.00×10^7	-	-	1.4
2	h6M2Re40	2.0	4.00×10^7	6.0	14.5	1.4
3	h8M2Re40	2.0	4.00×10^7	8.0	18	1.4
4	h10M2Re40	2.0	4.00×10^7	10.0	24	1.4

Second objective was to quantify the effects of Mach number on the micro-ramp wake, keeping the micro-ramp height and the unit Reynolds number constant for the incoming flow as shown in table 3.5.
The **third** and final objective of the campaign dealt with categorizing the effects of changing

Table 3.5: Test matrix for varying Mach number, keeping the micro-ramp height and unit Reynolds number fixed.

Exp. No.	**Case Designation**	**Mach Number**	**Reynolds Number (Unit)**	**Micro-ramp Height (in mm)**	x_{MR} **(in mm)**	Δt **(in** μ**s)**
5	M1.5Re40	1.5	4.00×10^7	-	-	1.4
6	h8M1.5Re40	1.5	4.00×10^7	8.0	18	1.4
7^1	M2Re40	2.0	4.00×10^7	-	-	1.4
8^3	h8M2Re40	2.0	4.00×10^7	8.0	18	1.4
9	M2.5Re40	2.5	4.00×10^7	-	-	1.3
10	h8M2.5Re40	2.5	4.00×10^7	8.0	18	1.3
11	M3Re40	3.0	4.00×10^7	-	-	1.3
12	h8M3Re40	3.0	4.00×10^7	8.0	18	1.3

unit Reynolds number on micro-ramp wake. It is to be noted that test conditions for experiments number 1 and 3 are repeated as indicated in superscripts of the experiment numbers in table 3.5 and 3.6. They have been reproduced in the different tables for ease of understanding the trend of test conditions.

[3]Micro-ramp height with '-' in all tables implies the testing would be done without any disturbance in the tunnel to get a flat plate turbulent boundary layer profile for the specified condition of Mach and Reynolds number.

Table 3.6: Test matrix for varying Reynolds number, with fixed micro-ramp height and fixed Mach number.

Exp. No.	**Case Designation**	**Mach Number**	**Reynolds Number (Unit)**	**Micro-ramp Height (in mm)**	x_{MR} **(in mm)**	Δt **(in** μ**s)**
13	M2Re28	2.0	2.80×10^7	-	-	1.4
14	h8M2Re28	2.0	2.80×10^7	8.0	18	1.4
15[1]	M2Re40	2.0	4.00×10^7	-	-	1.4
16[3]	h8M2Re40	2.0	4.00×10^7	8.0	18	1.4
17	M2Re52	2.0	5.40×10^7	-	-	1.4
18	h8M2Re52	2.0	5.40×10^7	8.0	18	1.4
19	M2Re64	2.0	6.40×10^7	-	-	1.4
20	h8M2Re64	2.0	6.40×10^7	8.0	18	1.4

Chapter 4

Results : Undisturbed Boundary Layer

In this chapter, the test results for undisturbed boundary layer cases are presented in table 4.1. Measurements at Mach 3.0 did not have enough seeding to get good PIV results and hence those results will not be used for comparison henceforth. The first section 4.1 discusses the boundary layer profiles and their integral properties. In section 4.2, the skin friction coefficient is discussed and finally, section 4.3 presents the fluctuation level present in the tunnel. The undisturbed boundary layer properties are obtained as an average of the profiles between 40-50mm from the start of the first field of view.

Table 4.1: Experimental conditions and undisturbed boundary layer properties.

Parameters	**M1.5Re40**	**M2Re28**	**M2Re40**	**M2Re52**	**M2Re64**	**M2.5Re40**
M_∞	1.5	2.0	2.0	2.0	2.0	2.52
U_∞ (m/s)	417	498	498	498	498	559
P_o (Pa)	$2.48\text{x}10^5$	$2.06\text{x}10^5$	$2.94\text{x}10^5$	$3.82\text{x}10^5$	$4.70\text{x}10^5$	$3.72\text{x}10^5$
T_o (K)	278	278	278	278	278	278
T_∞ (K)	191	154	154	154	154	122
ρ_∞ (kg/m^3)	1.231	0.593	0.848	1.102	1.357	0.614
δ_{99} (mm)	16.4	17.4	17.5	17.0	16.2	18.2
δ^* (mm)	2.77	3.86	3.82	3.66	3.48	4.43
θ (mm)	1.32	1.37	1.34	1.31	1.23	1.27
H	2.1	2.82	2.85	2.79	2.82	3.48
δ^*_{inc} (mm)	1.79	2.05	1.99	1.93	1.83	2.05
θ_{inc} (mm)	1.47	1.65	1.62	1.57	1.48	1.65
H_{inc}	1.22	1.24	1.23	1.22	1.22	1.24
u_τ (m/s)	14.65	18.7	18.3	18.0	17.8	21.6
C_f	$1.76\text{x}10^{-3}$	$1.64\text{x}10^{-3}$	$1.57\text{x}10^{-3}$	$1.52\text{x}10^{-3}$	$1.49\text{x}10^{-3}$	$1.41\text{x}10^{-3}$
C_f (Cousteix)	$1.57\text{x}10^{-3}$	$1.46\text{x}10^{-3}$	$1.37\text{x}10^{-3}$	$1.31\text{x}10^{-3}$	$1.27\text{x}10^{-3}$	$1.18\text{x}10^{-3}$
Re (1/m)	$39.9\text{x}10^6$	$28.0\text{x}10^6$	$39.9\text{x}10^6$	$52.0\text{x}10^6$	$63.9\text{x}10^6$	$39.7\text{x}10^6$
$Re_{\theta_{inc}}$	$58.7\text{x}10^3$	$46.2\text{x}10^3$	$64.6\text{x}10^3$	$81.6\text{x}10^3$	$94.6\text{x}10^3$	$65.5\text{x}10^3$
Re_θ	$52.7\text{x}10^3$	$38.4\text{x}10^3$	$53.5\text{x}10^3$	$68.1\text{x}10^3$	$78.6\text{x}10^3$	$50.4\text{x}10^3$

4.1 Boundary Layer profiles

Typical boundary layer properties for turbulent flows were defined in section 2.1. Trapezoidal method is one of the ways to calculate the integral boundary layer properties. The density variation in the boundary layer can be given by the Crocco-Busemann (White and Corfield (2006)) relation for adiabatic wall, which is given as follows:

$$\frac{\rho_w}{\rho} = \frac{T}{T_w} = 1 + \left(\frac{T_{aw}}{T_w} - 1\right)\frac{u_{BL}}{U_\infty} - \frac{r{u_{BL}}^2}{2T_w C_p} \tag{4.1}$$

The trapezoidal integration between the wall and first measured data point linearly interpolates the velocity from the wall to that data point. This is the region where velocity gradient is expected to change most and a wrong estimate would affect the values of the δ^*_{inc} and θ_{inc}. Hence, for near wall region, an approximation of the form $u_{nearwall}(y) = ay^b$ was used, taking the wall point and the first 5 measured data points to get the values of the constants a and b. The power law approximation comes from the log law, and the obtained values were in good agreement with the value of $b \approx 1/7$ as reported by Schlichting et al. (2000). The obtained velocity profile for case M1.5Re40 is shown in figure 4.1 zoomed to a region close to the wall. This figure also shows interpolated data between the experimentally obtained velocity values.

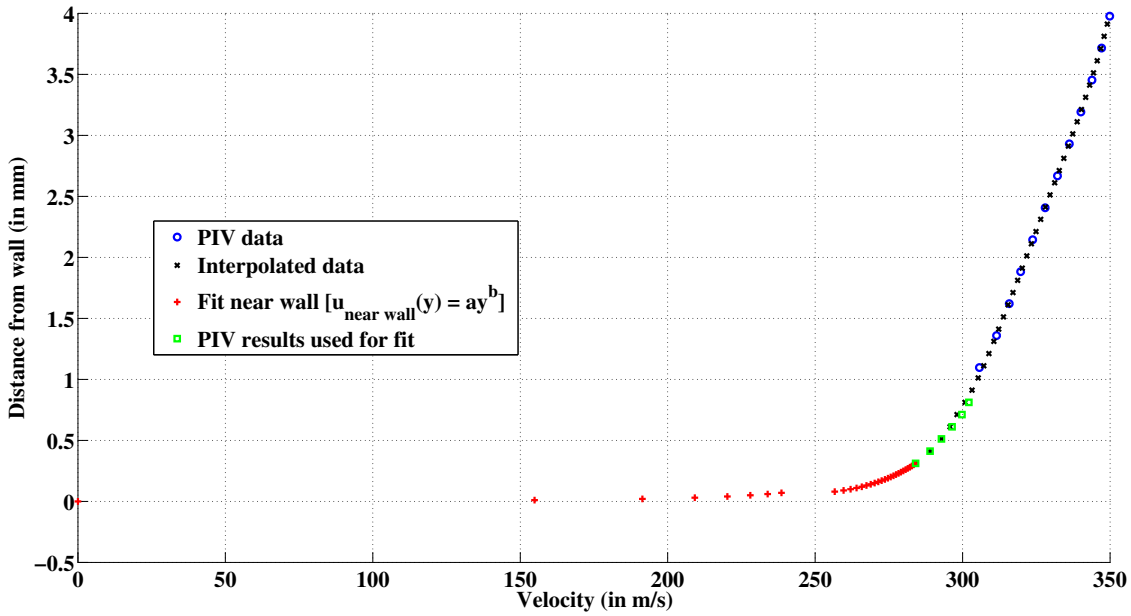

Figure 4.1: Velocity profile for case M1.5Re40. Blue circles denote PIV data, black crosses denote the interpolated velocity data, red plus signs denote the fit near the wall and green squares denote the near wall PIV values used to obtain the pwoer law fit.

4.1.1 Mach number effects

The contour plots obtained from the PIV experiment, for the undisturbed cases with changing Mach number and are given in figure Appendix A. A clear indication of the thickening of the boundary layer with increasing Mach number can be deduced when comparing figure A.1(a) with A.1(c).

The effect of increasing the Mach number on the velocity profile can be ascribed to the decrease in the density ($\frac{\rho}{\rho_\infty}$) (see equation 4.1) as one moves towards the wall. The boundary layer thickness increases with Mach number to compensate the lower density, confirming the Mach number effect on δ_{99} reported by Schlichting et al. (2000). It can be seen that for the lower Mach number (figure 4.2), the velocity profile ($\frac{u}{U_\infty}$) is fuller away from the wall which agrees with the results reported in Matting et al. (1961). This also implies that the incompressible displacement thickness, momentum thickness and shape factor for lower Mach number should be lower, which is verified from the data as given in table 4.1.

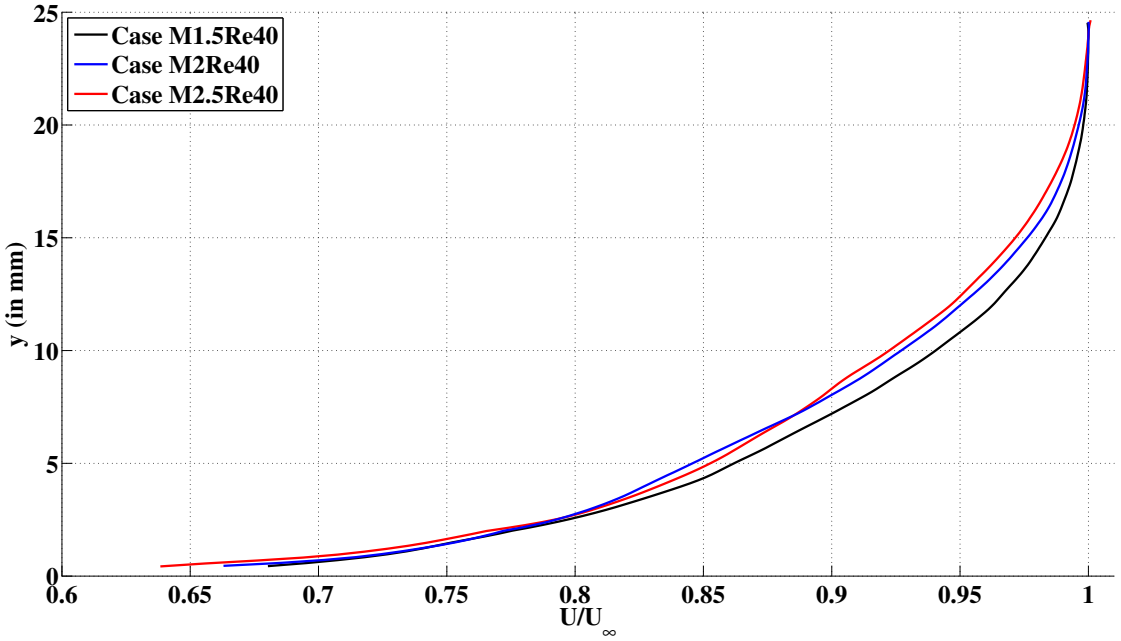

Figure 4.2: Velocity profiles for varying Mach number cases M1.5Re40, M2Re40 and M2.5Re40.

4.1.2 Reynolds number effects

Figure A.2 in appendix A shows the comparison of the contour plots for varying Reynolds number at constant Mach number. Figure 4.3 shows the velocity profiles with increasing Reynolds number. The velocity profiles become fuller with increasing Reynolds number, agreeing with the trend reported in Schlichting et al. (2000). This is the consequence of the

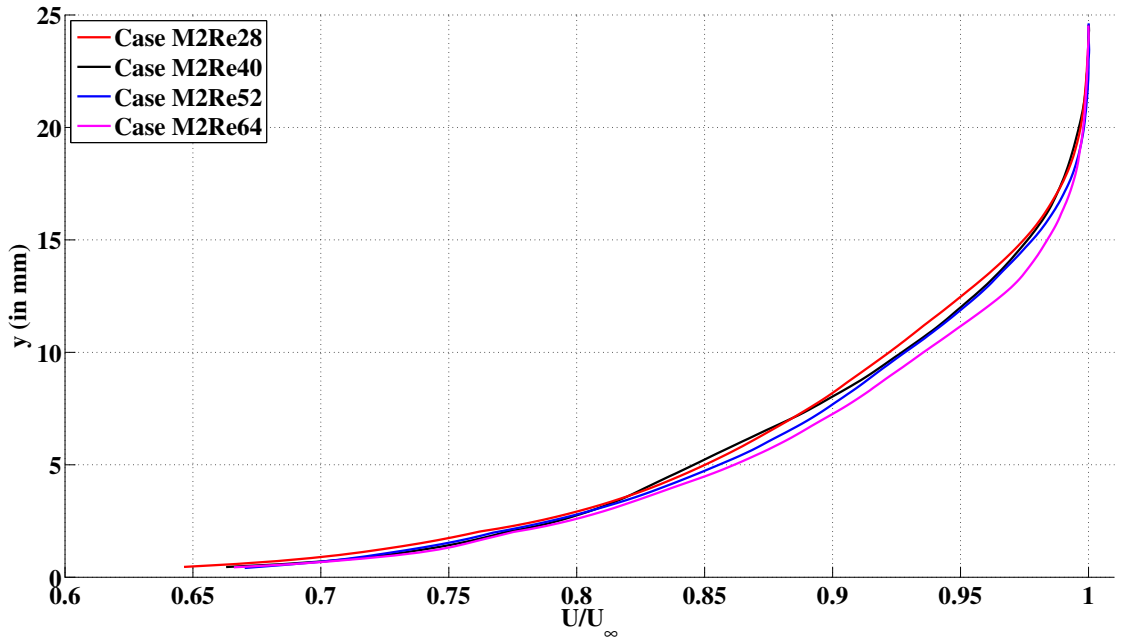

Figure 4.3: Velocity profiles for varying Reynolds number cases M2Re28, M2Re40, M2Re52 and M2Re64.

decrease in viscous forces with increasing Reynolds number, which implies the outer region of the turbulent boundary layer profile is retarded less due to lower wall shear (White and Corfield (2006)). Further, the shape factor H_{inc} (from 1.24 to 1.22) and boundary layer thickness δ_{99} (from 17.4 to 16.2) decreases as the Reynolds number increases.

Schlichting et al. (2000) also reports that velocity profiles for changing Reynolds number become similar if u/U_∞ is plotted against y/δ^*. These results are confirmed from the experiments as can be seen in figure 4.4.

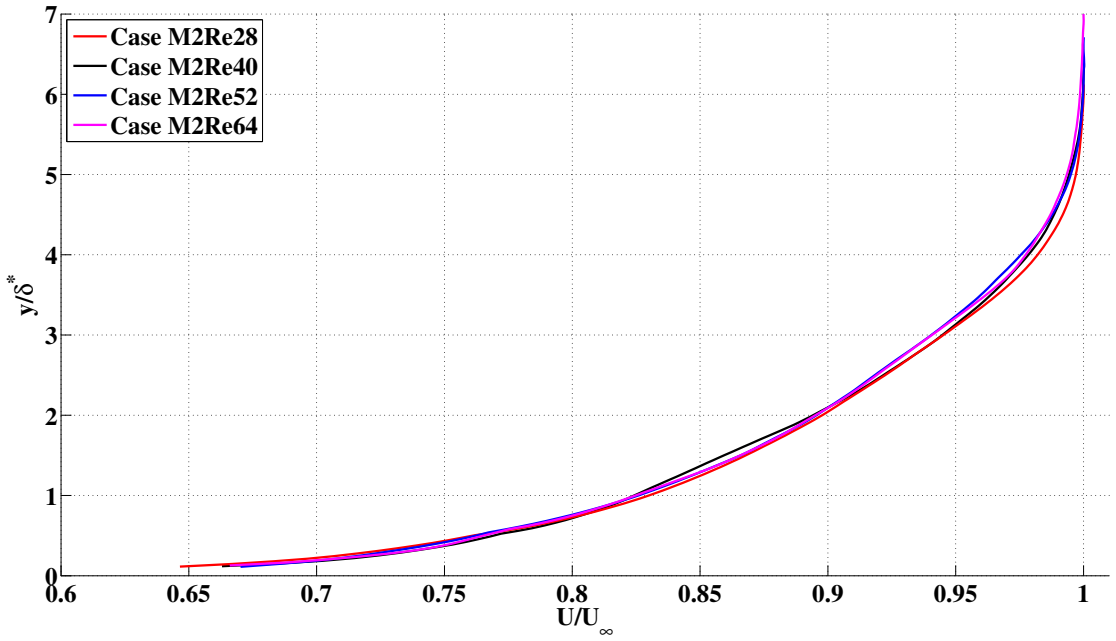

Figure 4.4: Velocity profiles scaled with displacement thickness in wall normal direction (Schlichting et al. (2000)) for varying Reynolds number cases M2Re28, M2Re40, M2Re52 and M2Re64.

4.2 Skin Friction Coefficient

The skin-friction coefficient C_f can be calculated from the u_τ for the best fit of Van-Driest's log law (section 2.1) on the velocity profile and using the relation $C_f = 2\frac{\rho_w}{\rho_e}\left(\frac{u_\tau}{U_e}\right)^2$. The log law fit for case M2Re40 is shown in figure 4.5. The fits for all other case are presented in appendix B.

Due to increasing viscous dissipation in compressible boundary layer, the skin-friction coefficient decreases with increasing Mach number at fixed Reynolds number (Smits and Dussauge (2006)). A similar trend for increasing Mach numbers has been observed in the experiments. The results for case M2Re40 have also been compared with the tests performed by Humble (2009) in the same facility at almost similar flow conditions (M=2.07, P_o=2.76x10^5 Pa, T_o=286K). The C_f(=1.52x10^{-3}), u_τ(=19.4 m/s) and θ(=1.4 mm) obtained by them have values similar to those measured for case M2Re40 (See table 4.1).

The measured C_f can also be compared with the semi-empirical relation (equation 4.2) given by Cousteix (1989).

$$C_f = \frac{0.0172}{\mathrm{Re}_\theta^{0.2}} f^{6/5} \qquad with: \qquad f(M_\infty) = \frac{C_f}{C_{f_i}} \tag{4.2}$$

where the value of compressible skin friction coefficient to incompressible skin friction coeffi-

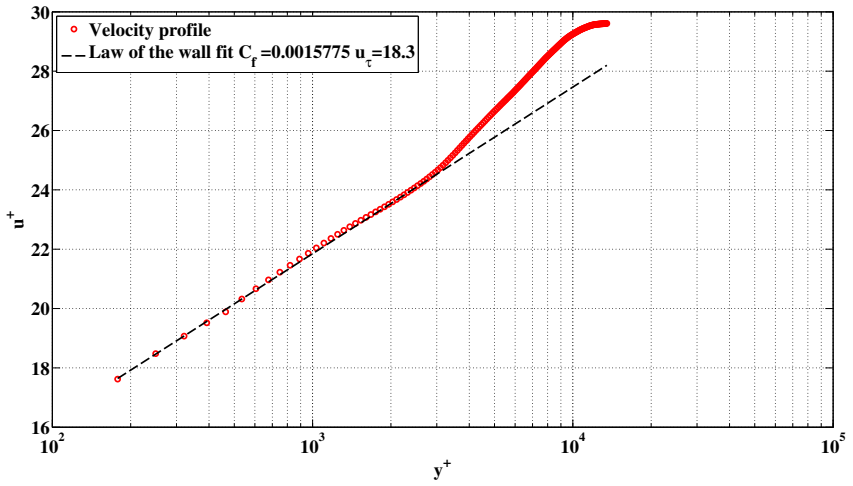

Figure 4.5: Van Driest's log law fit for case M2Re40.

cient ($\frac{C_f}{C_{f_i}}$) has been obtained from the equation 4.5 (which is explained later).
It is observed that as the Mach number increases, the C_f values obtained from Cousteix's relation differ more from the experimentally obtained C_f. It is quite probable that the difference is coming due to some improper scaling in the determination of the $\frac{C_f}{C_{f_i}}$ scaling ratio. Smits and Dussauge (2006) explains how this scaling ratio has been obtained. For an incompressible isothermal flow, the approximate power-law dependence of C_{f_i} is given by

$$C_{f_i} = K \left(\frac{\rho_\infty U_\infty \lambda_i}{\mu_e} \right)^{-m} \tag{4.3}$$

For compressible flows, the following relation has been reported

$$C_f = K \left(\frac{\rho_w}{\rho_\infty} \right) \left(\frac{\lambda_i}{\lambda_c} \right)^{-m} \left(\frac{\rho_w U_\infty \lambda_c}{\mu_w} \right)^{-m} \tag{4.4}$$

Assuming that viscosity follows the power-law relation i.e. $\frac{\mu_w}{\mu_\infty} = \left(\frac{T_w}{T_\infty} \right)^{-\omega}$ (Cousteix used $\omega = 0.76$), and for a one-seventh power-law at a constant Reynolds number the value of $m \approx 0.25$; the following relation is obtained

$$\frac{C_f}{C_{f_i}} = \left(\frac{\lambda_i}{\lambda_c} \right)^{-m} \left(\frac{T_\infty}{T_w} \right)^{1-(\omega+1)m} \tag{4.5}$$

λ_i and λ_c are length scales for incompressible and compressible flows. Now, here is where the equation is approximated by using x-location for length scale making the ratio $\frac{\lambda_i}{\lambda_c} = 1$. This approximation might not be accurate, because at different Mach numbers the turbulent length scales may differ for compressible flows. Another reason for the difference can be (Smits and Dussauge (2006)) that for supersonic flows, the 'correct' Reynolds number is based on the fluid properties evaluated at the wall temperature, rather than Re_θ.

4.3 Fluctuation Levels

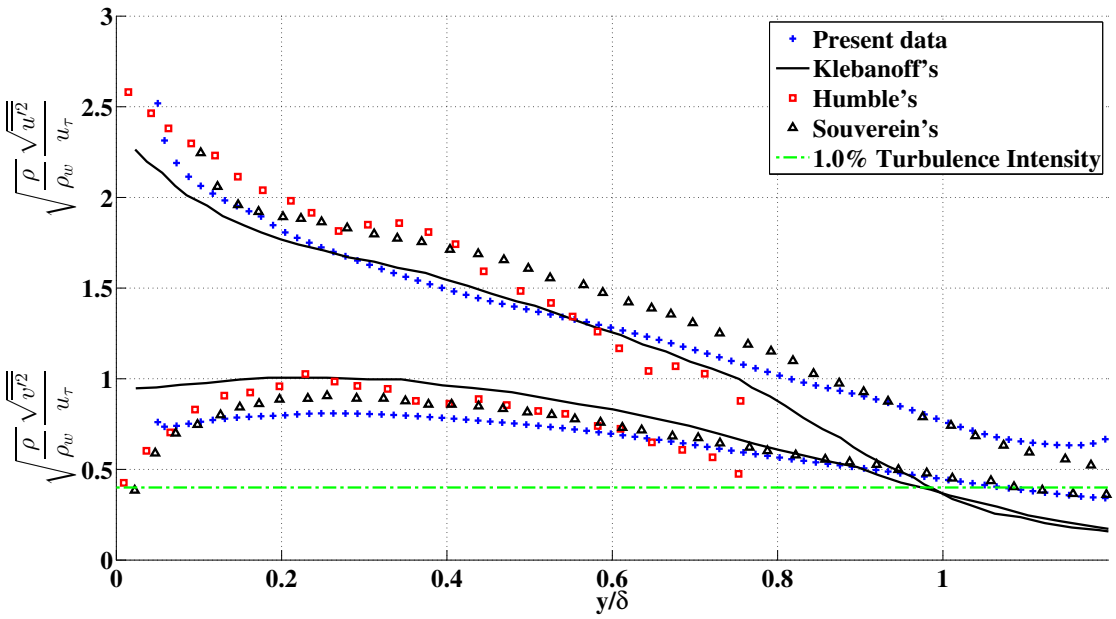

Figure 4.6: Velocity fluctuations in Morkovin scaling (upper curves represent u' and lower curves represent v'. Compared with Klebanoff (1955), Humble (2009) and Souverein (2010). Green line denotes the freestream turbulence intensity of 1.0%.

The turbulence properties are important to characterize the undisturbed boundary layer and substantiate the validity of the PIV data. The streamise and wall normal RMS velocity distributions for case M2Re40 (using 300 image pairs) are compared with reference data from Klebanoff (1955) in figure 4.6. The velocity fluctuation data obtained by Humble (2009) and Souverein (2010) are also used as a reference since their experiments were done in the same TST-27 wind tunnel, though under different conditions. The data are normalized by the friction velocity. It was reported by Kistler (1959) that velocity fluctuations divided by friction velocity fall with increasing Mach number, which is understandable, considering the fact that increasing the Mach number also ends up increasing the friction velocity u_τ. Compressibility effects are taken into account using Morkovin's hypothesis (Morkovin (1962)), by pre-multiplying the compressible data with the density ratio $\sqrt{\frac{\rho}{\rho_w}}$. To calculate the local mean density $\rho(y)$ in the boundary layer, Crocco-Busemann's approximation (White and Corfield (2006)) was used, as given by equation 4.1. For adiabatic walls, as approximated in this study, $T_w = T_{aw}$ and hence, the second term on the r.h.s. of the equation becomes zero.

It is evident from the figure that both streamwise and wall-normal components agree quite well with Klebanoff's data. The streamwise RMS velocity fluctuations for the present study fall below the RMS fluctuations reported by Humble and Souverein in separate experiments. However near the edge of the boundary layer (from 80% δ_{99}) and in the freestream, the present results, though being off from Klebanoff's data, agree quite well with Souverein (2010). The

fluctuations seem to reach agreeable free-stream turbulence level (as denoted by the green line). The freestream fluctuation are higher than 1.0% turbulence intensity level because the seeding rake also introduces some turbulence in the flow (Humble (2009)).

In summary, the undisturbed boundary layer measurements are in good agreement with previous data sets from the same test facility. The trends seen in the boundary layer properties are in agreement with the expectations from earlier literature. The incoming boundary layer for all cases do not show any strange behaviour and can be termed as standard turbulent boundary layers.

Chapter 5

Results : Micro-ramp Flow

In this chapter, the results of the experiment for all cases with micro-ramp will be discussed. The following notations are introduced:

- The letter h followed by the number denotes the height of the micro-ramp used for that case in mm.
- The remaining characters denote the inflow conditions at which the micro-ramp was tested. The inflow conditions are listed in table 4.1.

For example, h8M2Re40 means the results are for a micro-ramp of height 8mm tested at inflow condition M2Re40 (see table 4.1 for inflow conditions).
In section 5.1 the oil flow visualization results are presented and discussed. Section 5.2 is devoted to the PIV results as obtained from the experiment and finally in section 5.3, the PIV results are analyzed. The PIV analysis is given in a separate section so that the reader can observe the untouched data and see how the scaling and analysis affects and refines the results to give useful information about the effects of device height, Mach number and Reynolds number.

5.1 Oil Flow Visualization results

The oil-flow visualization results are presented in this section. Figure 5.1 shows the structures present in the vortex wake, as discussed in sub-section 2.3.1. A spanwise structure of the mean **primary** and **second secondary vortices** can be seen in figure 5.2. The primary vortices push the oil towards the center-line before separating form the surface, whereas the second secondary vortices push the oil outwards from the center forming clear oil streaks which form the vortex footprints. The present results confirm the vortex flow model proposed by Li et al. (2011). The oil flow lines on the micro-ramp surface show that the vortices start building up

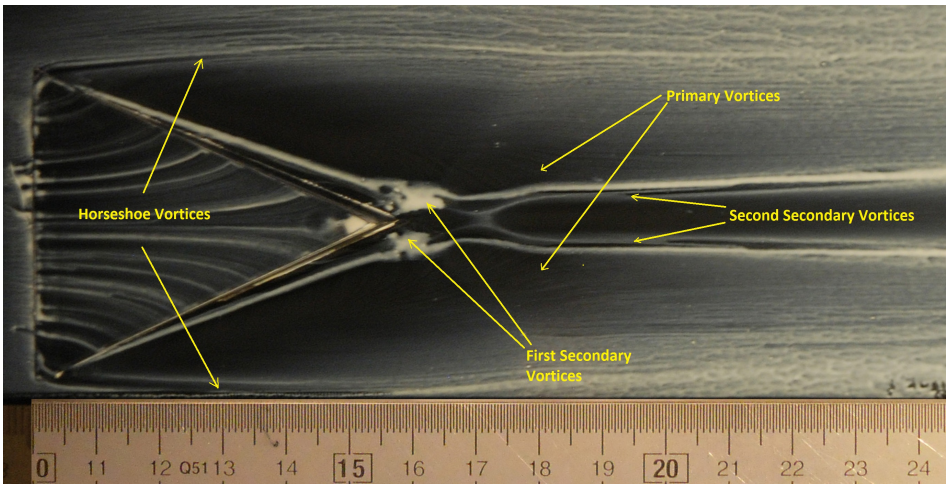

Figure 5.1: Vortex footprints from surface oil-flow visualisation for h8M2Re40.

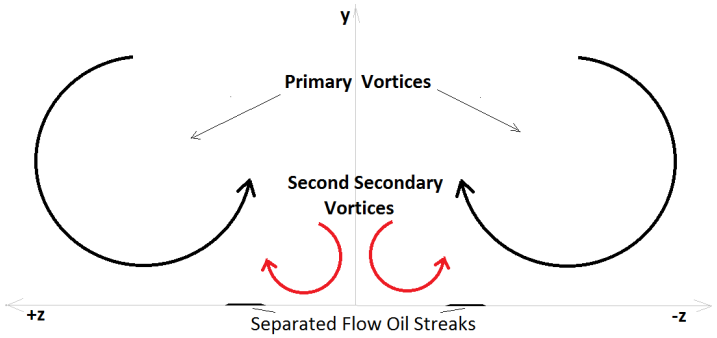

Figure 5.2: Schematic of the primary and secondary vortices that influence the oil streaks.

from the leading edge and the flow turns towards the edges. The oil moves by a small amount when the tunnel is shut down due to compression wave, as discussed in section 3.4. The **primary vortex** and the **horseshoe vortices** (showing an hourglass feature) are visible clearly. In addition, one can see the *kink* before which the **first secondary vortices** end, giving rise to **second secondary vortices**.

There are many interesting observations that can be made from figure 5.4, which shows the oil flow visualizations for the cases h8M1.5Re40, h8M2Re40, h8M2.5Re40 and h8M3Re40. For the sake of clarity, the lowest and highest Mach number cases shall be compared with each other. From the oil-streaks on micro-ramp surface, it can be seen that the flow starts turning earlier and more tightly along the edge for a Mach number of 1.5 than for a Mach number of 3.0. This can be noticed by observing the hourglass feature for horse-shoe vortices for h8M1.5Re40 and h8M3Re40 (as pointed in Figure 5.1). For the lower Mach number case h8M1.5Re40, the horse-shoe vortices are more curved and they start turning inwards (locations shown by yellow arrow in figures 5.4) after approximately 40mm from the leading edge of the micro-ramp. On the other hand, for case h8M3Re40, the same flow feature is straighter and starts curving inwards only at about 80-90mm from the micro-ramp's leading edge.

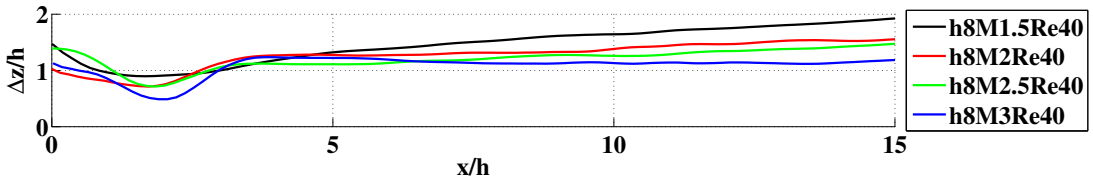

Figure 5.3: Height normalized separation between the primary vortex footprints traced for different Mach number cases from the oil flow visualization.

The *first secondary vortices* near the wall almost touch for the higher Mach number case (the kink is thinner for figure 5.4(d) compared to figure 5.4(a)),i.e. the spacing between them decreases with increasing Mach number. The observation for the primary vortices is similar as one moves downstream. Figure 5.3 shows the gap between the primary vortex footprints at different Mach numbers, as obtained from the oil flow images. It can be seen as the Mach number increases, the streaks made by *second secondary vortices* and the *primary vortices* start moving closer and the oil becomes less discernible. This might be because at lower Mach number the primary vortices are stronger and they curl upwards faster(Lee and Loth (2011)), pushing each other away; and hence they give the underlying *second secondary vortices* enough space to move outwards. Also, since the primary vortex is stronger, due to energy transfer, the *second secondary vortices* are also stronger, and hence a much clear separation line is visible for case h8M1.5Re40. At higher Mach number, the primary vortices do not rise up that fast and hence the secondary vortices are also pushed closer when one moves downstream.

The Oil-flow visualizations for varying Reynolds number cases h8M2Re28, h8M2Re40, h8M2Re52 and h8M2Re64 are shown in figure 5.5. There is no observable trend with changing Reynolds number. The kinks where *first secondary vortices end* are of similar sizes for all cases and so are the primary vortices and the horseshoe vortex.

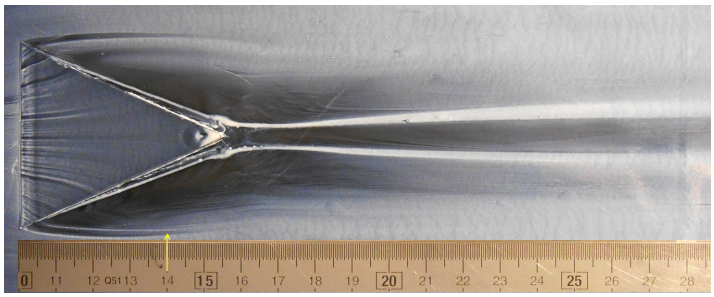

(a) Case h8M1.5Re40

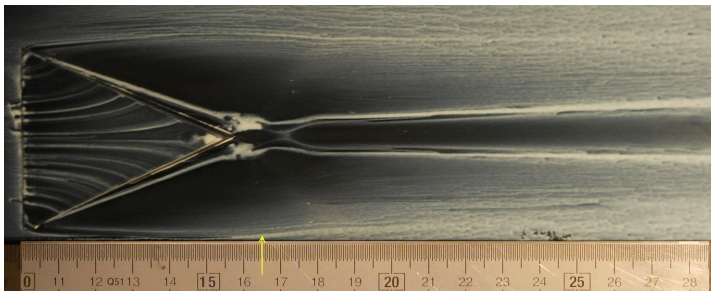

(b) Case h8M2Re40

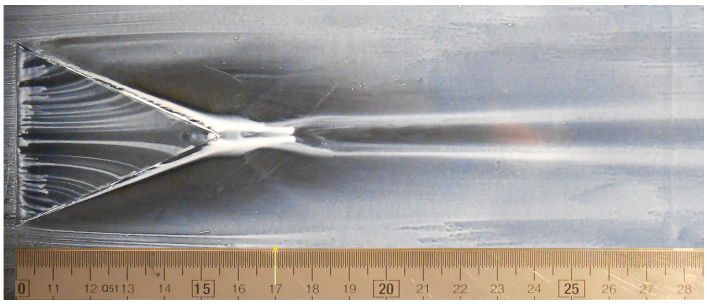

(c) Case h8M2.5Re40

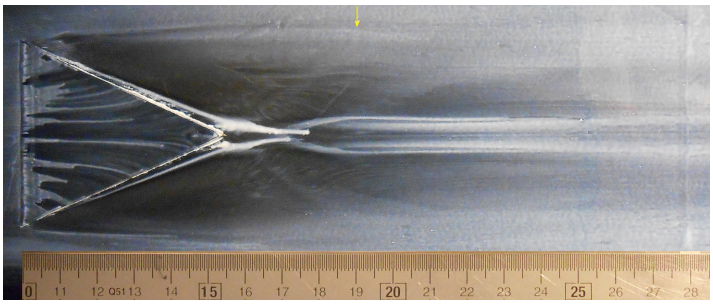

(d) Case h8M3Re40

Figure 5.4: Oil Flow visualisation results for 8mm micro-ramp at varying Mach Number. Yellow arrow shows the location where the horse-shoe vortex footprint turns inwards.

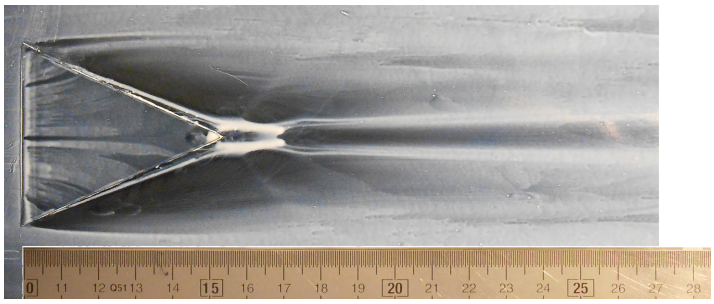

(a) Case h8M2Re28

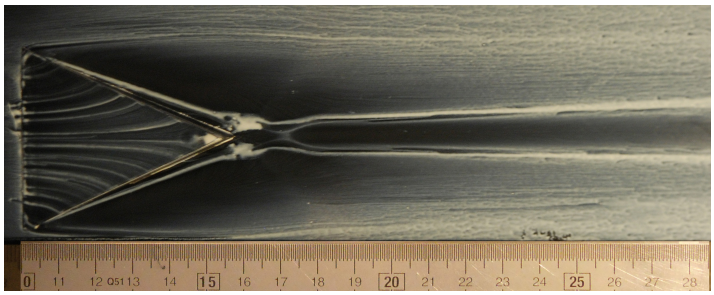

(b) Case h8M2Re40

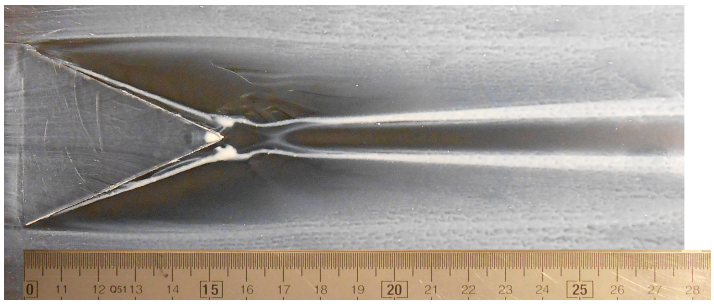

(c) Case h8M2Re52

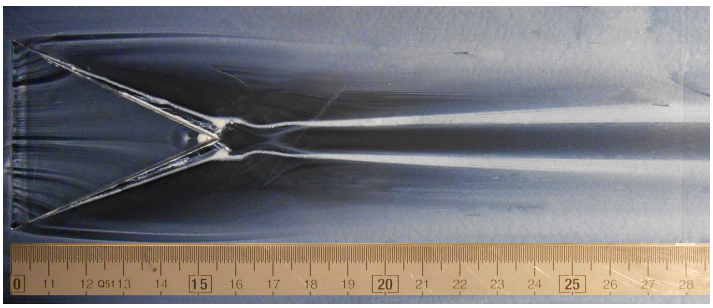

(d) Case h8M2Re64

Figure 5.5: Oil Flow visualisation results for 8mm micro-ramp at varying Reynolds Number.

5.2 Particle Image Velocimetry Results

This section presents the results of the PIV measurements that were performed on the cases with micro-ramp. In this section, the discussion starts with identifying the starting location for data extraction. It is followed by giving general velocity profiles and discussing the properties of the profile which will be used further in this section. The next sub-section deals with presenting the general results and trends observed in wake properties with changing micro-ramp height, Mach number and Reynolds number.

5.2.1 Measurement start location

The measurement start location behind the micro-ramp is determined by two factors, namely, the PPP levels in the wake and the reflections from the micro-ramp .
To find a start location for data extraction, the PPP levels (Particle per Pixel) in Camera 1 for all the cases were measured. Particle per pixel is the ratio of the number of particles in image to the image size in pixels and it indicates the amount of seeding present in the flow during the measurements. For best results from PIV cross-correlation, there should be at-least 9-10 particles in each interrogation window. The PPP levels are shown as a contour plot in figure 5.6. PPP levels were checked only for camera 1 because the corresponding field of view is nearest to the micro-ramp and hence, is affected most by the amount of particle mixing. In addition, the wake is strongest in the region close to the micro-ramp which results in ejection of the tracer particles. The PPP levels in the wake increase slowly as one moves away from the micro-ramp because the vortex strength decreases and the particles get more uniformly mixed in the flow. It was also seen that for higher Mach number, the PPP level is quite low in the wake closer to the micro-ramp, as can be compared between figure 5.6(a) and 5.6(b). Some other aberrations in the PPP level are also seen near x $\approx 6.5h$ behind the micro-ramp which have been masked while doing PIV processing.
In almost all of the cases, there were direct reflections from the micro-ramp surface and indirect reflections from the tunnel side walls which interfered with the measurements up to 5h behind the micro-ramp.

It was observed that the limitation due to low PPP levels dominate in the high Reynolds number and high Mach number cases for which the data is reliable only after x $\approx 8h$. Hence, the observations in the flow field are compared only after x=8h to maintain consistency.

5.2.2 Contour Plots

In this sub-section, the contour plots for all the tested cases, normalized by the freestream velocity are presented. The contour plots have been made after stitching the PIV results from all four cameras. As concluded in the previous sub-section, the data can be considered to be reliable only after around 6h distance behind the micro-ramp.

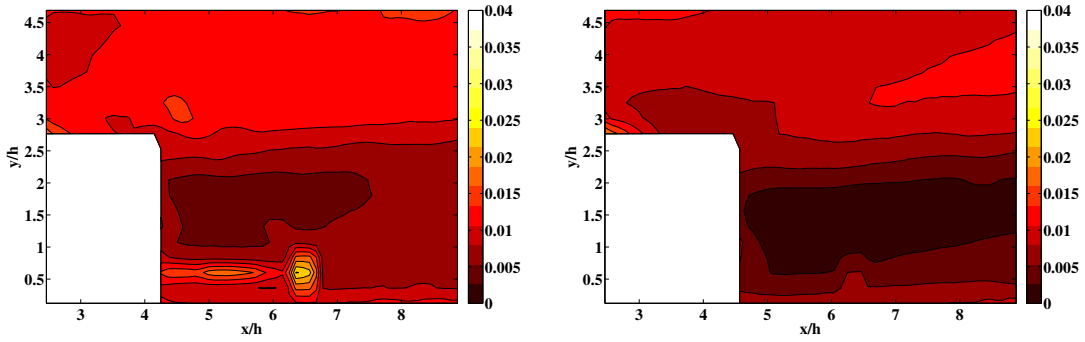

(a) Case h8M1.5Re40 Camera 1

(b) Case h8M2.5Re40 Camera 1

Figure 5.6: Particles per Pixel levels for two test cases (Using Camera 1). The reflections from micro-ramp are masked.

It can be seen from figure 5.7 the size of the wake region is proportional to micro-ramp height used(as the axes are scaled with micro-ramp height). The velocity deficit in the wake decreases and the wake lifts away from the surface when moving downstream. The angle of reattachment shock is the same for all three tested heights.

Contour plots for cases with changing Mach number are shown in figure 5.8. It can be clearly seen that as the Mach number increases, the reattachment shock angle decreases. For case h8M1.5Re40, the angle was measured to be 40.5°; for micro-ramp cases with undisturbed boundary layer condition M2Re40, it was measured to be 28.2° and for case h8M2.5Re40, the angle was found to be 23.3°. Also, the wake region lies lower for higher Mach number case h8M2.5Re40 when compared to low Mach number case h8M1.5Re40.
Figure 5.9 shows the contour plots of the cases with changing unit Reynolds number. There is no observable change in the flow features with changing Reynolds number. In the region near the micro-ramp, it seems that the velocity deficit decreases(i.e., wake strength decreases) with increasing Reynolds number. However, as can be seen from figure 5.9d that for the case h8M2Re64, the data is unreliable even till about 8h distance behind the micro-ramp due to reflections and low PPP levels observed for this case.

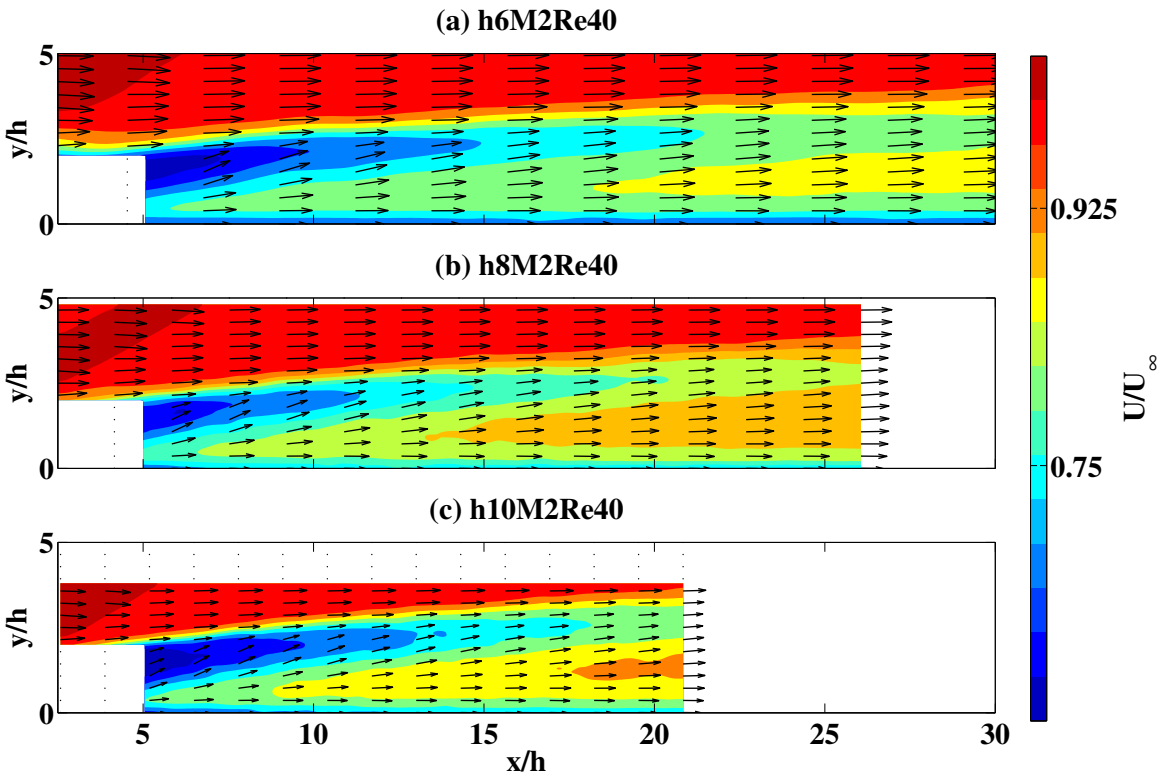

Figure 5.7: Normalized Contour plot for varying Micro-ramp Height cases.

5.2.3 Velocity Profiles

In this sub-section, the typical velocity profiles observed along the center-line in a micro-ramp's wake are discussed. It is followed by presenting the results of velocity profiles at different x-locations for all the tested cases.

Figure 5.10 shows typical streamwise velocity profiles behind the micro-ramp. The profile defines the locations and the values which will be used in defining characteristics of the micro-ramp wake. These profiles are not representative of the velocity magnitudes and are shown for illustrative purpose. Figure 5.10(a) shows a typical streamwise velocity profile downstream of the micro-ramp. Generally, the near-wall region of the velocity profile is fuller than uncontrolled turbulent flow due to the transfer of momentum by the micro-ramp's wake vortices. The flow at centerline of the micro-ramp contains a velocity deficit which is a remnant of the device wake. 'Wake Location' or wake height y_{wake}, shown by the red arrow in the figure, corresponds to the center of the low momentum region. The minimum velocity (shown by green arrow) in the wake region U_{min} is the velocity deficit existing in the wake. The deficit velocity U_{min} is used to define 'Wake Strength' which is numerically given as $\frac{U_\infty - U_{min}}{U_\infty}$. Also, the blue arrows indicate the location of upper and lower shear layers of the wake deficit region. These layers have been identified by calculating the location where the velocity profile switches from concave to convex and vice-versa (i.e. by locating the value of 'y' where the quantity $\frac{d^2U}{dy^2} = 0$).

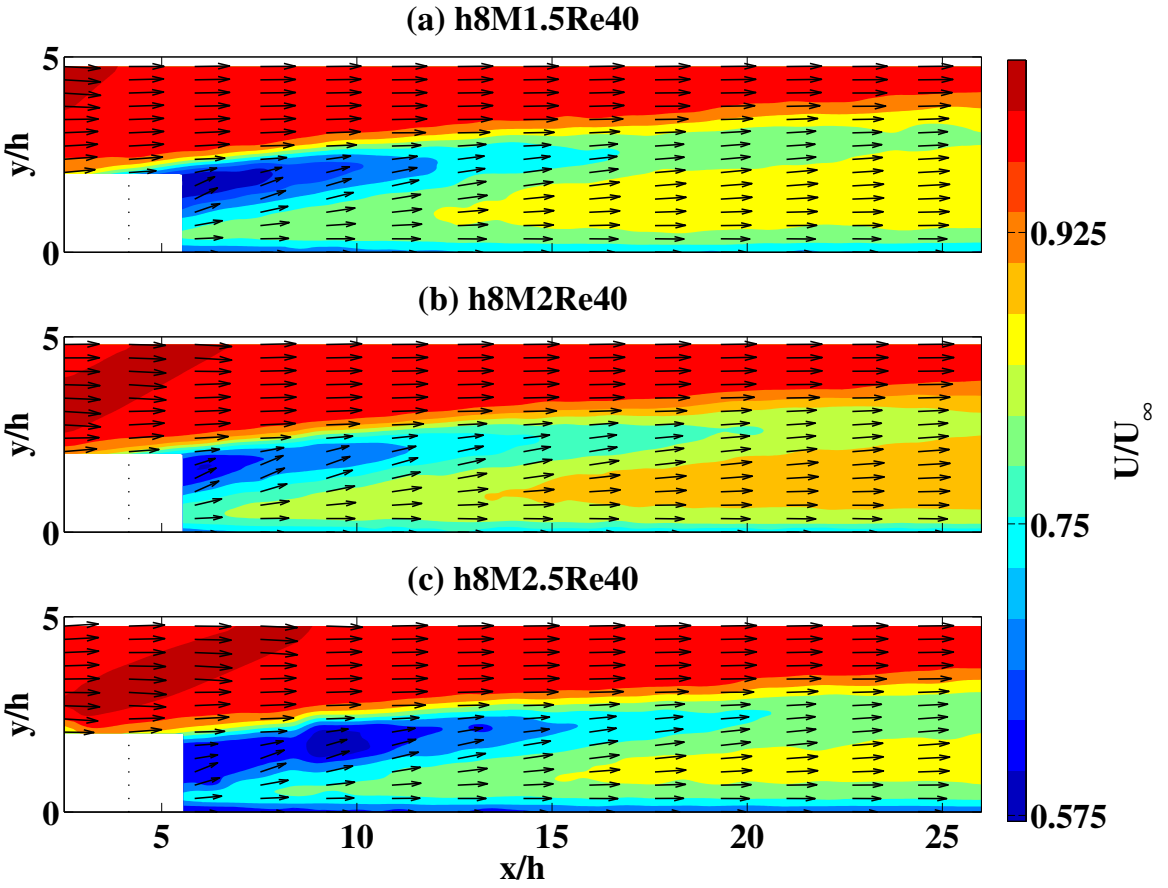

Figure 5.8: Normalized Contour plot for varying Mach number cases.

A typical upwash velocity profile is shown in figure 5.10(b). The region near the wall where the upwash velocity becomes negative denotes the presence of secondary vortices which rotate in direction opposite of the primary vortices. Hence along the micro-ramp centerline, these secondary vortices induce a velocity towards the wall. Away from the wall, the upwash from the primary vortex can be clearly seen. The peak of this vertical velocity maxima V_{max} lies slightly below the 'Wake Location' obtained from streamwise velocity profile. Upwash strength has been defined as $\frac{V_{max}}{U_\infty}$ and 'Upwash Location' y_{upwash} is shown by red arrow in the figure.

In the next part, the u-velocity profiles for all the cases is presented and discussed. The v-velocity profiles for the cases are presented in appendix C.

Micro-ramp height effects

Figure 5.11 shows the effect of changing micro-ramp heights (6mm, 8mm and 10mm) for the same inflow condition. As observed by Babinsky et al. (2009), the wake locations scale with micro-ramp height and a larger micro-ramp adds more momentum to the near wall region.

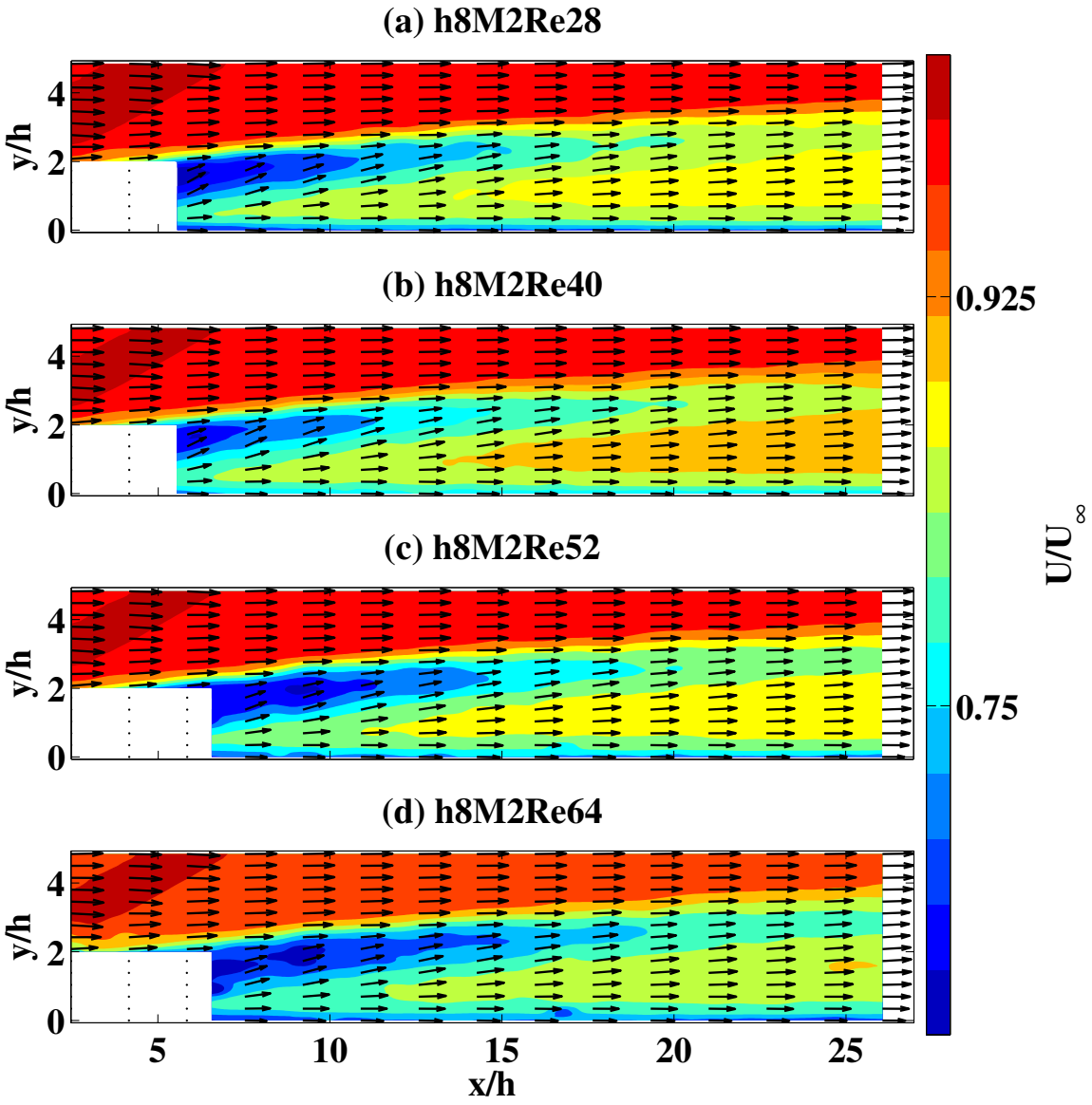

Figure 5.9: Normalized Contour plot for varying Reynolds number cases.

The primary vortex size and the momentum deficit region, hence, also scales with device height. It can also be deduced that for larger micro-ramps, the momentum deficit region is larger since the figures are scaled by micro-ramp height. The wake profiles along the center-line of the micro-ramp also scale with device height and hence it can be assumed that the drag increases with increasing device height.

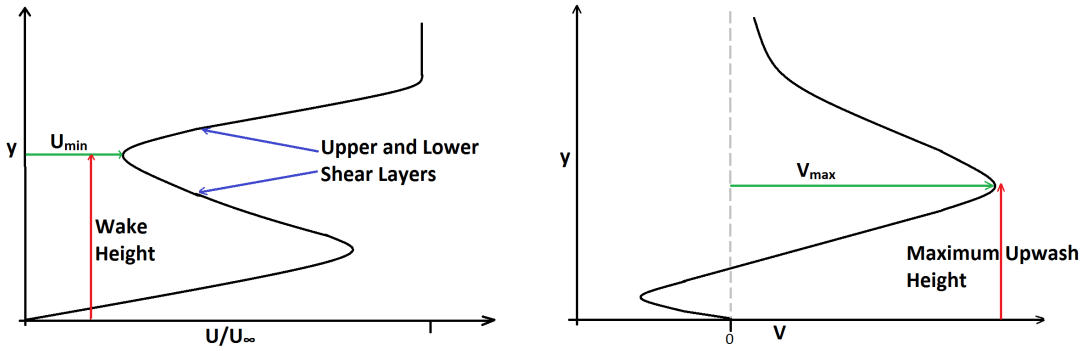

(a) Canonical u-velocity profile

(b) Canonical v-velocity profile

Figure 5.10: Typical velocity profiles behind a micro-ramp

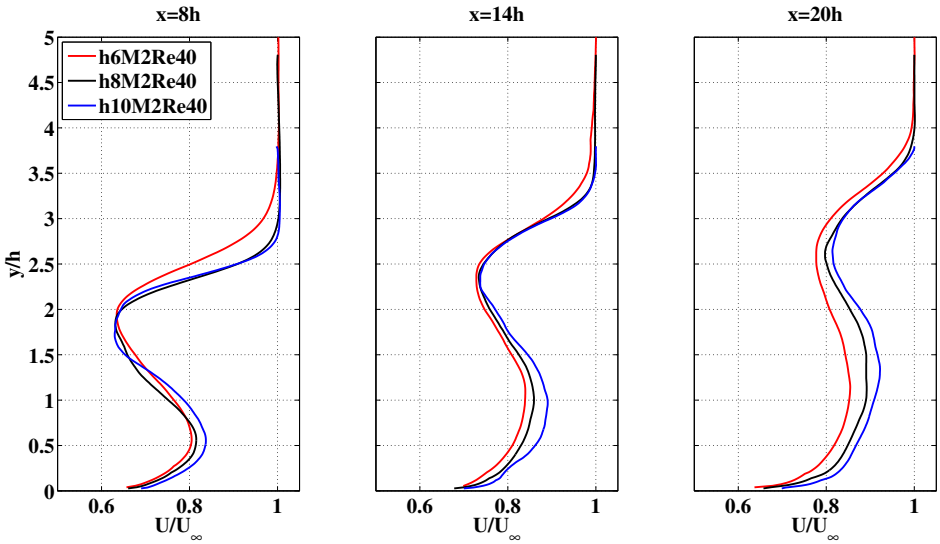

Figure 5.11: U-velocity profiles at x=8h, 14h and 20h for changing Micro-ramp heights.

Mach number effects

Figure 5.12 shows the velocity profiles obtained for the test cases h8M1.5Re40, h8M2Re40 and h8M2.5Re40 where the unit Reynolds number and the micro-ramp height are kept constant and only the Mach number is changed. At x=8.75h, the h8M2.5Re40 profile shows an overshoot because of the reattachment shock (as can be seen in figure A.1(c)) which has a lower angle for Mach 2.52. It can be seen from the plots that the wake strength is higher for a larger Mach number. The velocity profile is fuller near the wall for a lower Mach number indicating that at a higher Mach number, less momentum is added to the near wall region. It can also be seen clearly that increasing the Mach number pushes the wake location downwards as expected and discussed in 2.3.3.

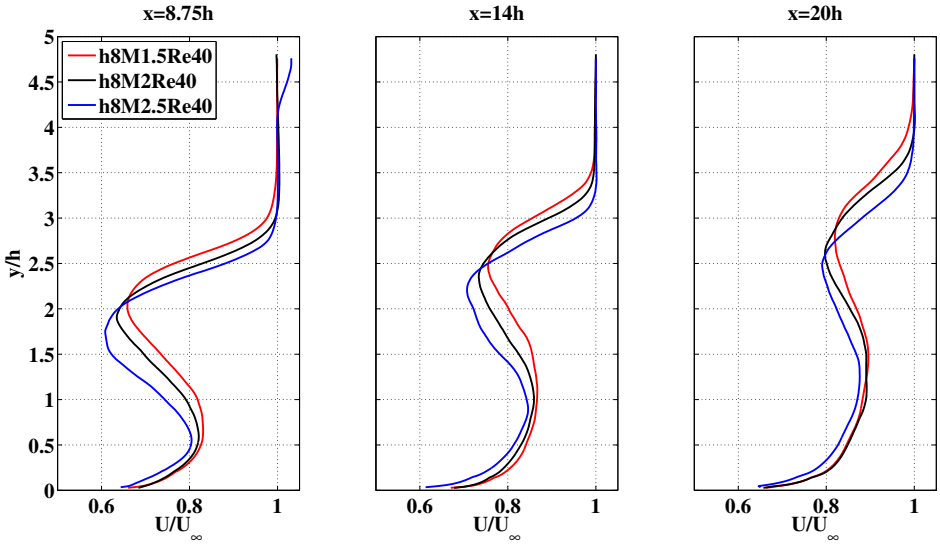

Figure 5.12: U-velocity profiles at x=8.75h, 14h and 20h for changing Mach number cases.

Reynolds number effects

The profiles with changing unit Reynolds number, are presented in figure 5.13. A weak Reynolds number effect can be seen in the region close to the micro-ramp. For the profiles at x=8h, it can be seen that lower Reynolds number case h8M2Re28 results in higher wake strength and relatively little momentum addition near the wall. Whereas, for the higher Reynolds number case h8M2Re64, exactly opposite trend is observed. Although, on moving downstream, this difference in the velocity profiles becomes less and the profiles agree quite well with each other.

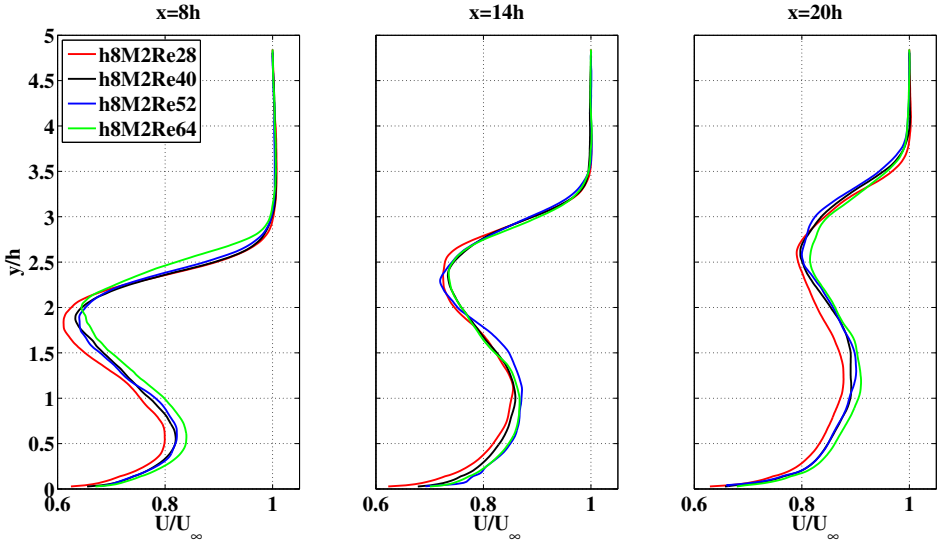

Figure 5.13: U-velocity profiles at x=8h, 14h and 20h for changing Reynolds number cases.

5.2.4 Wake Location

In this sub-section, the effects of changing Mach number, Reynolds number and micro-ramp height on the wake location are discussed.

Micro-ramp height effects

The wake location scales reasonably well with micro-ramp height, as can be seen in figure 5.14 which is in agreement with Babinsky's observations (Babinsky et al. (2009)). In all the three micro-ramp heights tested, the device wake gradually moves away from the wall due to the action of the primary vortices. The rate of this upward movement of device wake ($\frac{dy}{dx}$), also scales with the device height, as is evident from the figure. This also indicates that the strength of the vortices which are pushing the wake away from the wall increases with increasing micro-ramp height.

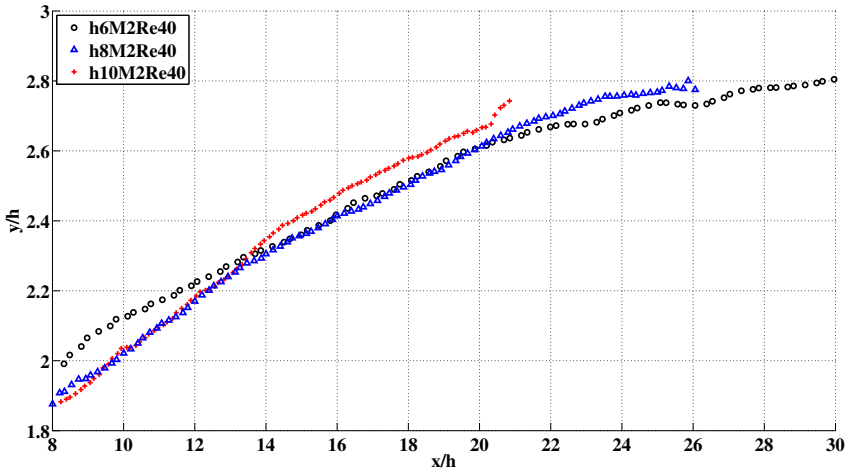

Figure 5.14: Scaled wake location (y/h) for changing micro-ramp height as a function of normalized distance behind micro-ramp (x/h).

Mach number effects

As discussed earlier in sub-section 2.3.3, it was expected that the wake location for higher Mach number would be lower. This has been shown correct by figure 5.15, where the cases tested have same micro-ramp height and unit Reynolds number. As discussed earlier, the rate of upward motion of wake location with respect to the distance behind micro-ramp can be correlated to the action of the primary vortices. Hence, the strength or the effect of primary vortices also reduces with an increasing Mach number. It can be seen in the figure that the wake-locations for all the cases are almost parallel to each other as one progresses downstream of the micro-ramp. Here, it might be useful to recall equation 2.8 which gives the rate of decay of the vortex strength. As can be seen from the flow properties, the C_f decreases with increasing Mach number (1.76×10^{-3}, 1.57×10^{-3} and 1.41×10^{-3} for M1.5Re40, M2Re40

and M2.5Re40 respectively). If the vortex height h_v is approximated by y_{upwash} (which is a reasonable approximation), from the velocity profiles at x=8h, the h_v approximately comes out to be 1.7h, 1.5h and 1.4h with decreasing Mach number. These values show that the ratio of C_f to h_v in the equation is almost similar for all Mach numbers. This might be an indication that the decay rate of primary vortex strength is independent of the Mach number.

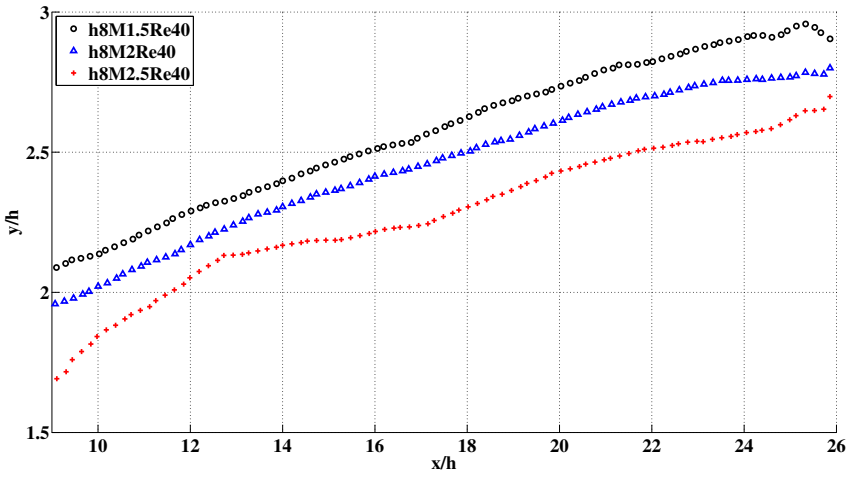

Figure 5.15: Scaled wake location (y/h) for changing Mach number as a function of normalized distance behind micro-ramp (x/h).

Reynolds number effects

It was observed that for the tested range of Reynolds number (table 4.1), the change in Reynolds number does not seem to have any effect on the location of the wake as can be seen in figure 5.16. This means that the flow features along the centerline of the micro-ramp do not change with changing Reynolds number and the wake location only depends on device height and the incoming Mach number.

5.2.5 Wake Strength

Wake strength, defined in the start of this section as $\frac{U_\infty - U_{min}}{U_\infty}$, has been used to categorize the strength of the low momentum region existing in the micro-ramp wake. In this sub-section, the effects of changing micro-ramp height, Mach number and Reynolds number on wake strength is discussed.

Micro-ramp height effects

Figure 5.17 shows the variation of wake strength vs. the micro-ramp height normalized distance behind the micro-ramp trailing edge. The wake strength scales, apparently, with

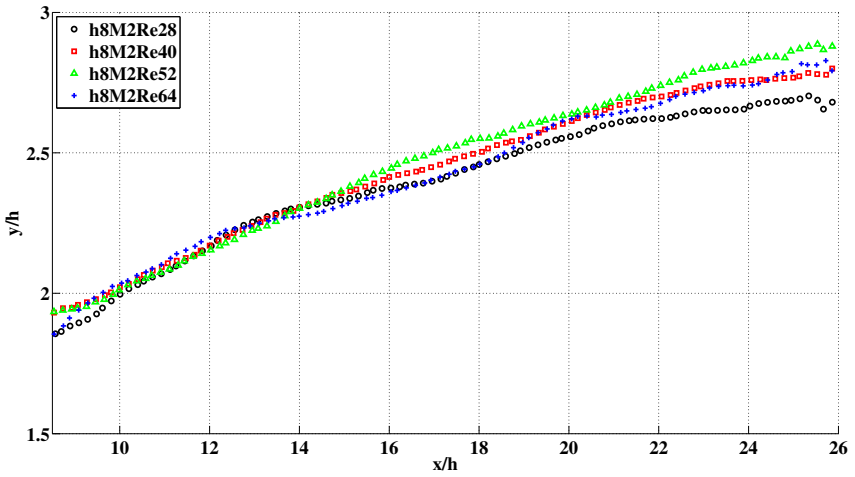

Figure 5.16: Scaled wake location (y/h) for changing Reynolds number as a function of normalized distance behind micro-ramp (x/h).

device height as can also be seen from the velocity profiles in figure 5.11. It implies that for the same absolute distance behind the micro-ramp trailing edge (x), the wake strength for a micro-ramp with larger height is bigger, implying a stronger low momentum region for a larger micro-ramp height. This conforms with the conclusions mentioned in Babinsky et al. (2009).

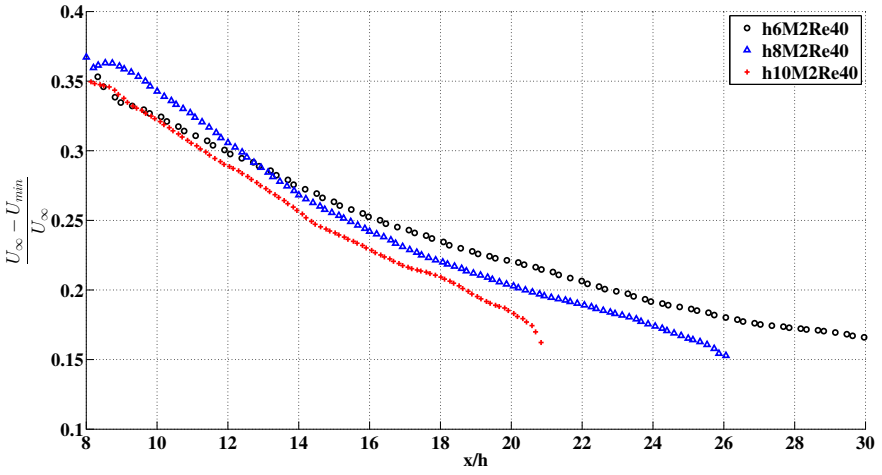

Figure 5.17: Wake strength variation for changing micro-ramp height as a function of normalized distance behind micro-ramp (x/h).

Mach number effects

It can be seen from figure 5.18 that the wake strength is higher for larger Mach number in the region near the micro-ramp. However, the difference becomes less pronounced as one moves

downstream. This implies that near the micro-ramp, the low momentum region is stronger for a higher Mach number and it continues to stay so, though the relative difference between the strength of low momentum region decreases.

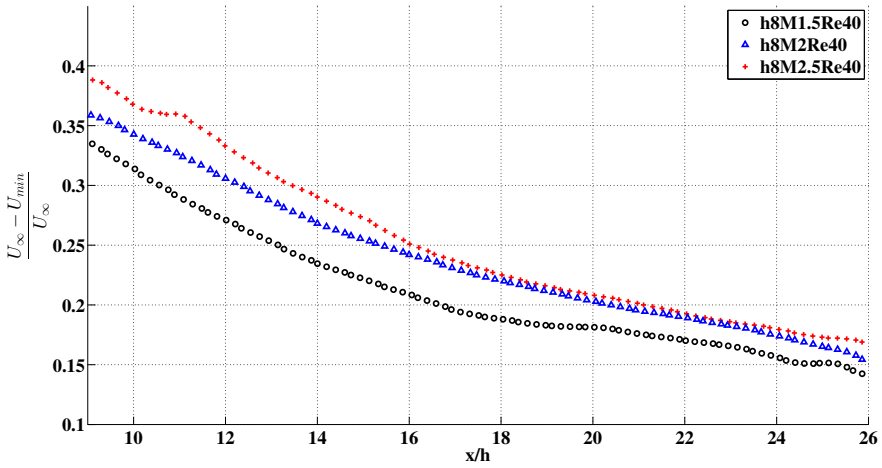

Figure 5.18: Wake strength variation for changing Mach number as a function of normalized distance behind micro-ramp (x/h).

Reynolds number effects

The wake strength for changing Reynolds number cases is given in figure 5.19. It was observed that near the micro-ramp, the wake strength is stronger for case h8M2Re28 than for case h8M2Re64. It can also be confirmed by observing the velocity profile at x=8h in figure 5.13. This indicates that Reynolds number probably effects the strength of the vortices near the micro-ramp, however this effect seems to disappear further downstream of the micro-ramp. After $x \approx 14h$ distance behind the micro-ramp trailing edge, the wake strength does not show any observable trend with changing Reynolds number.

5.2.6 Upwash Strength

Upwash strength is a measure of the maximum upwash existing in micro-ramp wake, normalized by the freestream velocity. It is an important quantity indicative of the vortex strength and circulation (Nolan (2013)). In this subsection, the trends in the upwash strength as a function of micro-ramp height, Mach number and Reynolds number are discussed. It is worth mentioning that the conclusions about the vortex strength from upwash are qualitative only.

Micro-ramp height effects

There is a clear trend visible in upwash strength near the micro-ramp for changing micro-ramp height, as can be seen in figure 5.20. The h10M2Re40 micro-ramp case has a higher

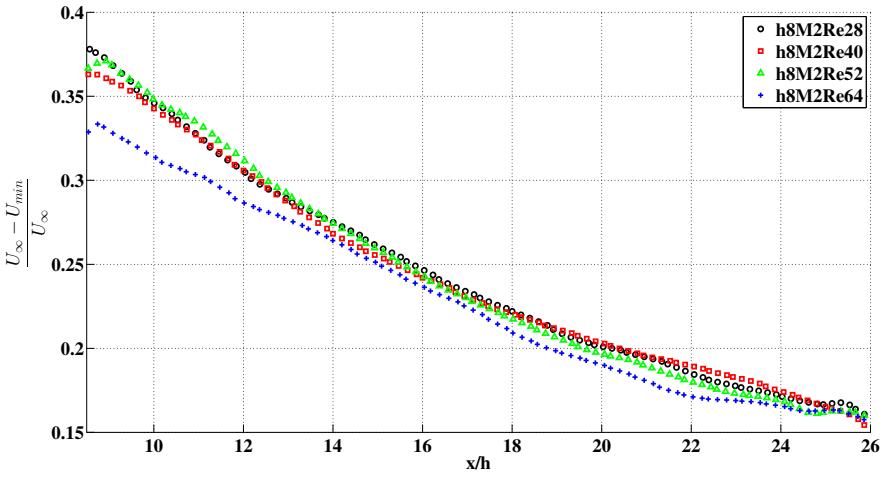

Figure 5.19: Wake strength variation for changing Reynolds number as a function of normalized distance behind micro-ramp (x/h).

upwash strength compared to h6M2Re40 micro-ramp case. It can, hence, be inferred from the plots that the vortices are stronger for a larger micro-ramp. This can also be the reason behind the fact that in figure 5.14, the evolution of wake location for h6M2Re40 is flatter(due to weaker vortices) compared to h10M2Re40. The primary vortex, although stronger, are further away from the center-line due to their bigger size for a larger micro-ramp. Hence, one would not observe a linear increase in upwash strength with micro-ramp height. Therefore, from the current results, it cannot be concluded that the vortex strength scales with device height. It is also seen from the plot that after around 20h behind the micro-ramp, the upwash strength becomes almost similar. That means that the decay of vortex strength with respect to height-normalized distance behind the micro-ramp is, probably, also faster for larger device height.

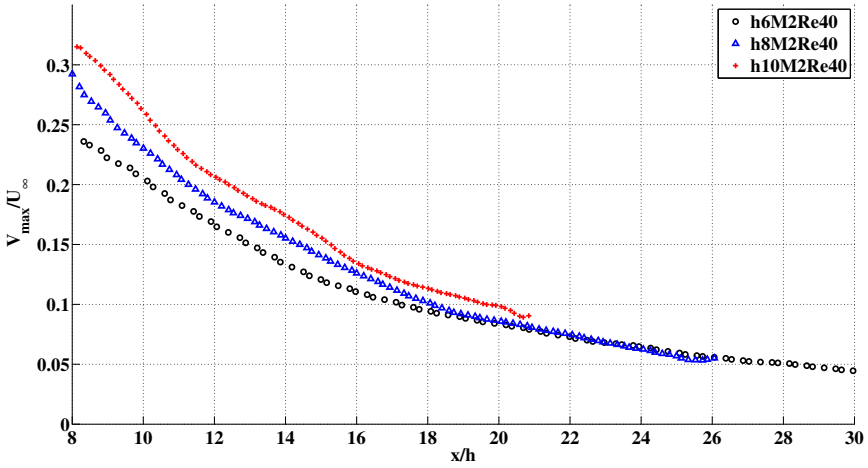

Figure 5.20: Upwash strength variation for changing micro-ramp height as a function of normalized distance behind micro-ramp (x/h).

Mach number effects

Figure 5.21 shows the variation of upwash strength with changing Mach number. It can be seen that near the micro-ramp, the upwash is highest for the lowest Mach number case h8M1.5Re40 compared to case h8M2Re40. For case h8M2.5Re40, it was not possible to get good results near the micro-ramp due to low PPP levels. Moving downstream of the micro-ramp, the upwash strength for case h8M1.5Re40 is the least, and that for case h8M2Re40 is most with the upwash strength for h8M2.5Re40 lying in between. The vortex strength probably decreases with increasing Mach number, thus decreasing the upwash strength, which might also account for lower wake location (figure 5.15). However, as can be seen from figure 5.3 which traces the vortex footprints, the primary vortices seem to move closer for higher Mach number, having a positive affect on the upwash strength. There are, thus, two phenomenon which have opposite affects on the upwash strength. Hence, the upwash strength cannot be directly correlated with the vortex strength in the cases with changing Mach number.

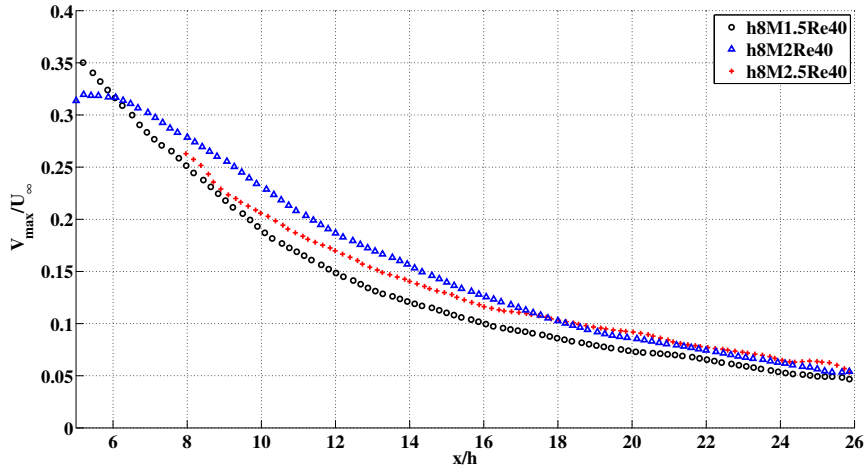

Figure 5.21: Upwash strength variation for changing Mach number as a function of normalized distance behind micro-ramp (x/h).

Reynolds number effects

Figure 5.22 shows the variation of upwash with changing Reynolds number. It can be seen that the upwash for case h8M2Re64 is lower compared to case h8M2Re28. For the cases h8M2Re40 and h8M2Re52, the upwash strength is almost similar to the low Reynolds number case. For all the cases, the upwash strength becomes similar as one moves away from the micro-ramp (at around x$\approx 15h$). The lower upwash strength for higher Reynolds number correlates with the lower wake strength for the same case as explained in subsection 5.2.5. Hence, it is quite probable that a higher Reynolds number makes the vortex weaker near the micro-ramp.

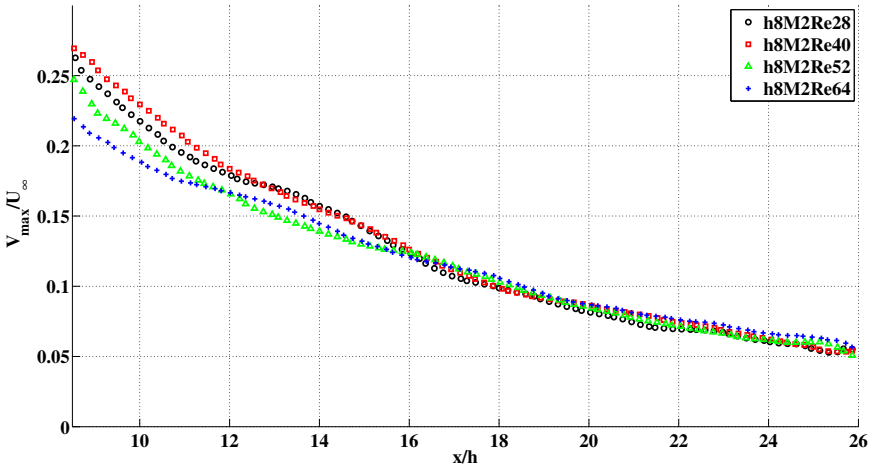

Figure 5.22: Upwash strength variation for changing Reynolds number as a function of normalized distance behind micro-ramp (x/h).

5.2.7 Shear Layers

As explained in subsection 5.2.3, the shear layers have been identified as the locations where the curvature of the u-velocity profile changes, above and below the wake location. Shear layers for the low velocity region in the horizontal velocity profile can give an estimate of the size of the low-momentum region (and hence, the approximate size of primary vortices).

Micro-ramp height effects

It can be seen that the upper and lower shear layers for cases with changing micro-ramp height almost fall on top of each other in figure 5.23. Both the x-axis and y-axis of the figure have been scaled with the micro-ramp height. This means that the size of the low momentum region scales with the micro-ramp height, i.e. micro-ramp with larger height creates a bigger momentum deficit region. This conforms with the observations on the momentum deficit region size reported by Babinsky et al. (2009). The evolution of the momentum deficit region away from the wall also scales with the micro-ramp height. If the present figure is compared with figure 5.14, it is worth noticing that the wake location loosely corresponds to the mid-point of upper and lower shear layers, and hence, to the center of the momentum deficit region. The gap between the shear layers increases gradually and since case h6M2Re40 offers a longer height normalized x-axis, it was chosen to enunciate the gap which increased from 1.1h at x=8h to 1.4h at x=30h.

Mach number effects

Figure 5.24 shows the evolution of upper and lower shear layer locations with changing Mach number. As discussed earlier in sub-section 5.2.4, the wake-location, and hence the momentum-deficit region lies lower for higher Mach number. This is also confirmed by the

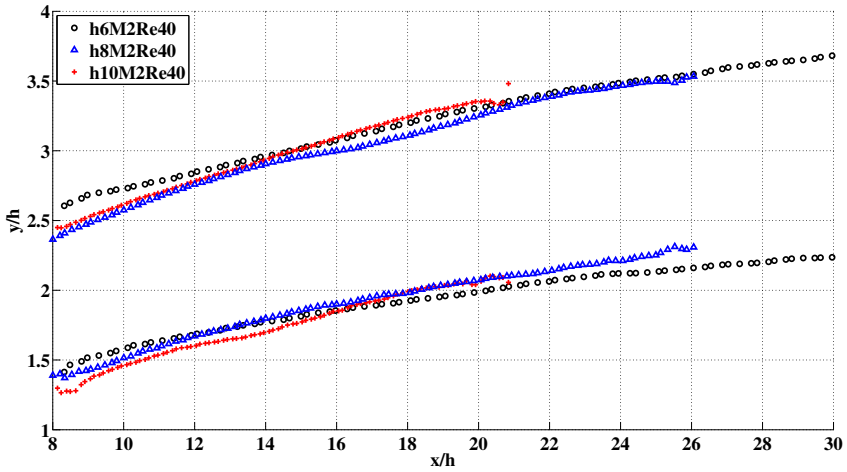

Figure 5.23: Upper and lower shear layer locations of the momentum deficit region for changing micro-ramp height as a function of normalized distance behind micro-ramp (x/h).

positions of the shear layers for cases h8M1.5Re40, h8M2Re40 and h8M2.5Re40. It is seen that the rate of upward motion of the shear layers with respect to distance behind the micro-ramp ($\frac{dy}{dx}$) is almost same for all 3 cases. The gap between upper and lower shear layers is, more or less, similar for all the cases, though it increases slightly while moving downstream. This indicates that the size of the momentum-deficit region does not depend on the freestream Mach number but only on the device height.

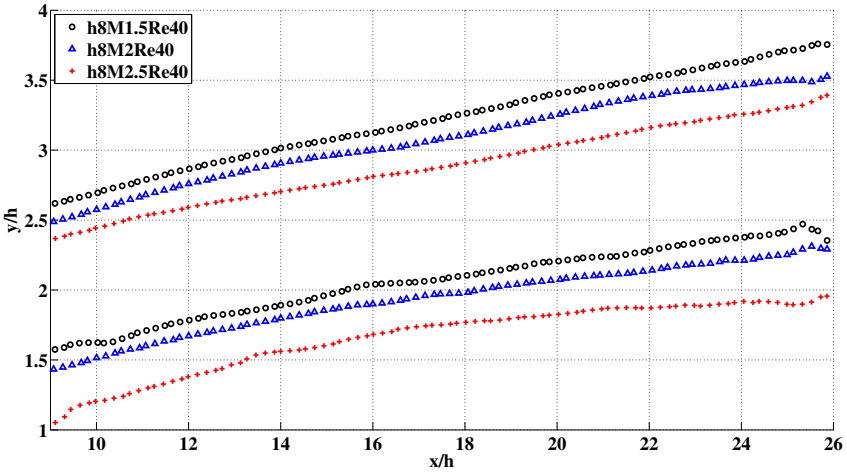

Figure 5.24: Upper and lower shear layer locations of the momentum deficit region for changing Mach number as a function of normalized distance behind micro-ramp (x/h).

Reynolds number effects

For cases with changing Reynolds number in the tested range, as shown in figure 5.25, no clear trend is visible. The size of the momentum deficit region, therefore only seems to depend on micro-ramp height. Reynolds number thus (in current test range) does not have any visible effects on the flow structure behind the micro-ramp though as discussed in previous sections, it might be effecting the strengths of the flow structures near the micro-ramp.

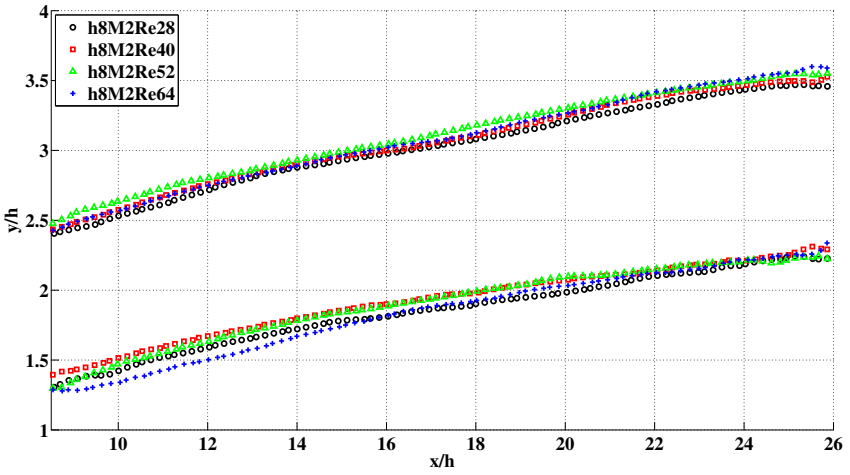

Figure 5.25: Upper and lower shear layer locations of the momentum deficit region for changing Reynolds number as a function of normalized distance behind micro-ramp (x/h).

5.2.8 Shape Factor

In this sub-section, the incompressible shape factor calculated from the streamwise velocity profile are compared for all cases. A lower incompressible shape factor means the boundary layer can withstand stronger adverse pressure gradient without separating.

Micro-ramp height effects

Figure 5.26 shows the variation of shape factor behind the micro-ramp with changing micro-ramp height. The dotted black line denotes incompressible shape factor for the undisturbed boundary layer. It can be seen that for larger micro-ramp, the shape factor crosses the free-stream value at a normalized distance (x/h) earlier than that for smaller micro-ramp. It can also be observed that the incompressible shape factor, for cases with micro-ramps, decreases beyond the corresponding undisturbed value. However, the decrease is more prominent for larger micro-ramp. From case h6M2Re40, since the data is available till 30h, it can be gauged that at large distance behind the micro-ramp (approx. 28-30h), the shape factor reaches a plateau (for all cases) and does not decrease further.

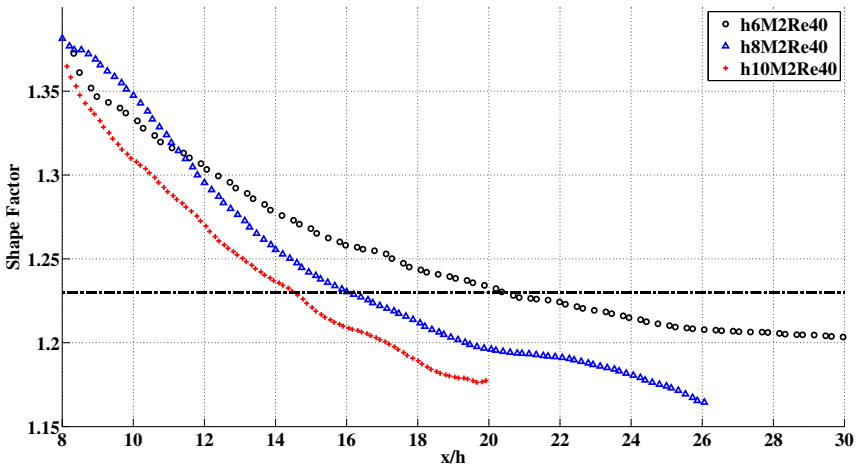

Figure 5.26: Shape Factor variation for changing micro-ramp height as a function of normalized distance behind micro-ramp (x/h). Black line denotes incompressible shape factor for undisturbed boundary layer case M2Re40.

Mach number effects

From figure 5.27 it can be seen that for the micro-ramp case with lower Mach number (h8M1.5Re40), the shape factor recovers to its corresponding undisturbed boundary layer value earlier than the cases with higher Mach number. It can also be observed that for a higher Mach number, the incompressible shape factor tends to remain larger than the lower Mach number case, throughout the measurement domain for the present experiment.

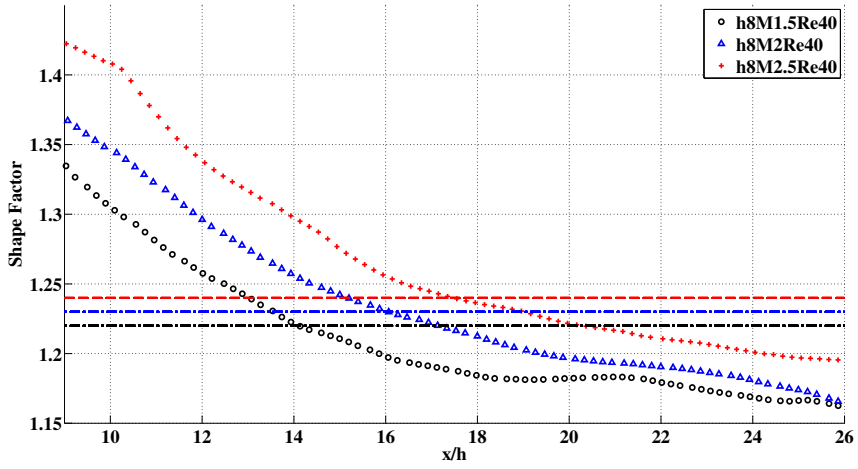

Figure 5.27: Shape Factor variation for changing Mach number as a function of normalized distance behind micro-ramp (x/h). Black line denotes incompressible shape factor for undisturbed boundary layer case M1.5Re40, blue line for case M2Re40 and red line for case M2.5Re40.

Reynolds number effects

It was observed that the incompressible shape factor behind the micro-ramp for varying Reynolds numbers recovers to the value for their respective undisturbed cases at approximately same location of x $\approx 16 - 18h$. Similar to the trends for undisturbed profiles, the shape factor for higher Reynolds number case h8M2Re64 is lowest and that for lower Reynolds number case h8M2Re28 is higher.

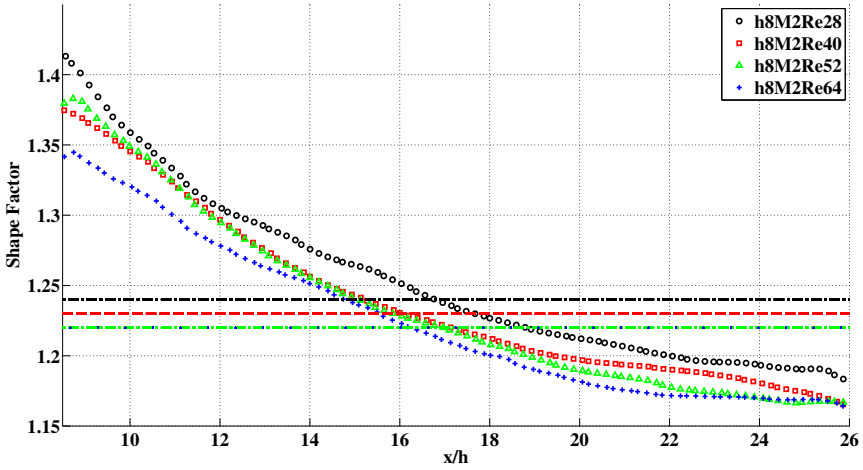

Figure 5.28: Shape Factor variation for changing Reynolds number as a function of normalized distance behind micro-ramp (x/h).Black line denotes incompressible shape factor for undisturbed boundary layer case M2Re28, red line for case M2Re40, green and blue dotted lines for cases M2Re52 and M2Re64 respectively.

Giepman et al. (2013), characterized the fullness of near wall micro-ramp wake profile by using added momentum flux. They reported that the distance between the micro-ramp and the shock for an effective control of separation is independent of the micro-ramp height and only depends on the boundary layer thickness. However, as discussed in appendix D, though scaling with δ_{99} does bring the plots closer, it is not that simple when both the micro-ramp height and the boundary layer thickness change.

5.3 Result Analysis

In this section, the results presented in section 5.2 are analysed and compared with existing literature.

5.3.1 Self Similarity of Velocity Profiles

As discussed in sub-section 2.3.2, the self-similarity of profiles for different micro-ramp height, Mach and Reynolds number will be compared using the parameters given by Sun et al. (2014). Sun et al. already showed that the profiles were self-similar for different micro-ramp heights and the self-similarity of profiles with micro-ramp height can be seen in figure 5.29. Figure 5.30 and 5.31 show that the velocity profiles are self-similar even with changing Mach number and Reynolds number. Since case h8M2Re40 is common for all shown profiles, it is worth

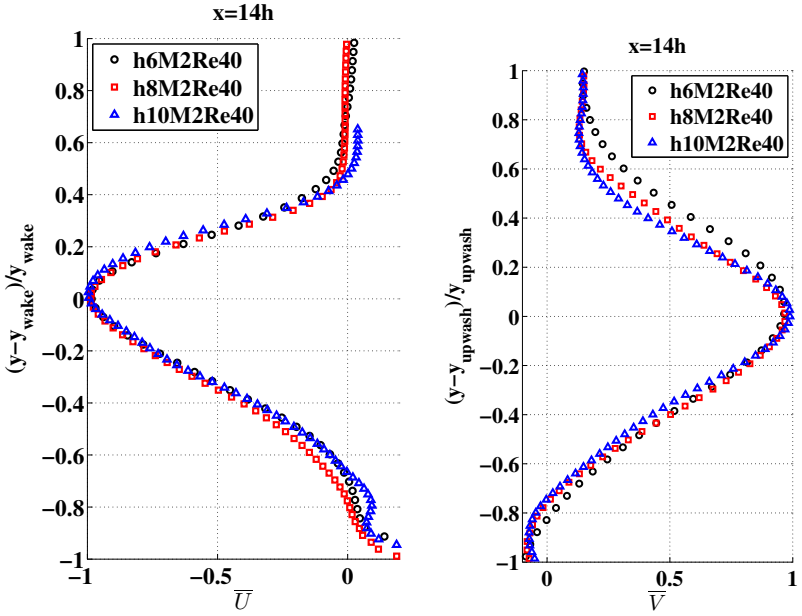

(a) Self similarity of horizontal velocity

(b) Self similarity of vertical velocity

Figure 5.29: Self-similarity profiles at x=14h for cases with different micro-ramp heights using scaling parameters given in Sun et al. (2014).

mentioning that for all the tested cases, the velocity profiles are self-similar. This implies that changing of Reynolds number, Mach number and micro-ramp height, does not essentially change any of the mean-flow features of the wake, though they might affect the strength and size of the flow features.

5.3.2 Wake Location Comparison with Literature

The wake locations for different Mach numbers from existing literature were compared in figure 2.16 and it was seen that for higher Mach number, the wake location was lower. Figure 5.32 compares the results obtained from the current experiment with experimental results by Nolan and Babinsky (2011), Babinsky et al. (2009) and Giepman et al. (2013). It can be

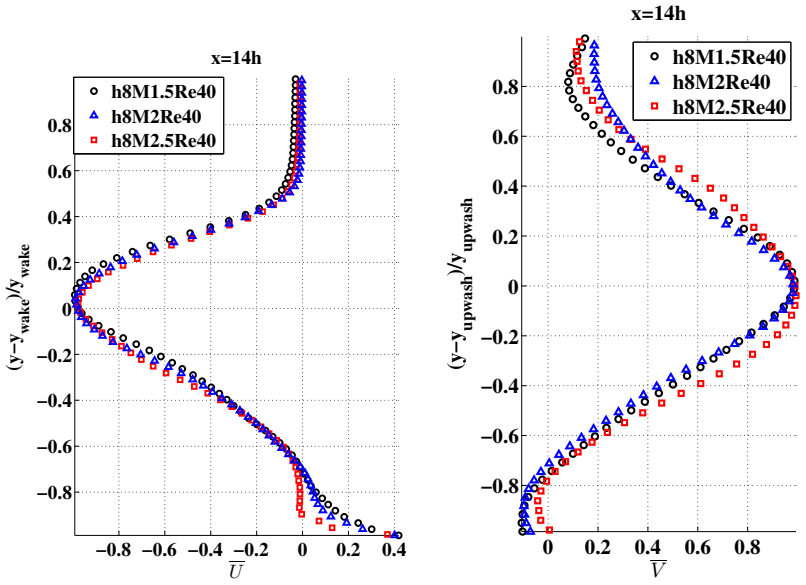

(a) Self similarity of horizontal velocity

(b) Self similarity of vertical velocity

Figure 5.30: Self-similarity profiles at x=14h for cases with different Mach number using scaling parameters given in Sun et al. (2014).

seen that for the case h8M2Re40 ($\frac{h}{\delta_{99}} \approx 0.46$), the results from current experiments agree quite well with the results by Giepman et al ($Re_{\theta_{inc}} = 21.8 \times 10^3$, $\theta_{inc} = 0.52mm$, $M = 2.0$, h=2mm, $\delta_{99} = 5.2mm$, $\frac{h}{\delta_{99}} \approx 0.39$). Also, the wake location for case h8M1.5Re40 is similar to that estimated form the contour plots of span-wise velocity given by Nolan and Babinsky (2011) ($Re_{\theta_{inc}} = 18.2 \times 10^3$, $\theta_{inc} = 0.7mm$, $M = 1.5$, $\delta_{99} = 7mm$, $\frac{h}{\delta_{99}} \approx 0.57$). Although, it was seen that for case h8M2.5Re40 ($\frac{h}{\delta_{99}} \approx 0.44$), the wake location was lower compared to h8M1.5Re40 and h8M2Re40 cases, it did not match that well with the results by Babinsky et al. performed at Mach 2.5. The reason might be because the experimental conditions for case h8M2.5Re40 ($Re_{\theta_{inc}} = 65.5 \times 10^3$, $\theta_{inc} = 1.65mm$ M=2.5, $\delta_{99} = 18.2mm$) were different from that of Babinsky et al. ($Re_{\theta_{inc}} = 28.8 \times 10^3$, $\theta_{inc} = 0.72mm$, $M = 2.5$, $\delta_{99} = 6mm$). It is also worth mentioning that the curve given by Babinsky et al. for wake location is a best fit curve fitted over the center of momentum-deficit region for all cases tested by them at four x-locations. For example the 2mm ($\frac{h}{\delta_{99}} \approx 0.4$) height micro-ramp case tested by them showed a slightly higher wake location than their best-fit and they identified that case as a measurement inaccuracy.

5.3.3 Scaling of Maximum Upwash

Sun et al. (2014) have proposed a power law scaling for decay of maximum-upwash downstream of the micro-ramp which has been discussed in 2.3.2. The upwash strength following

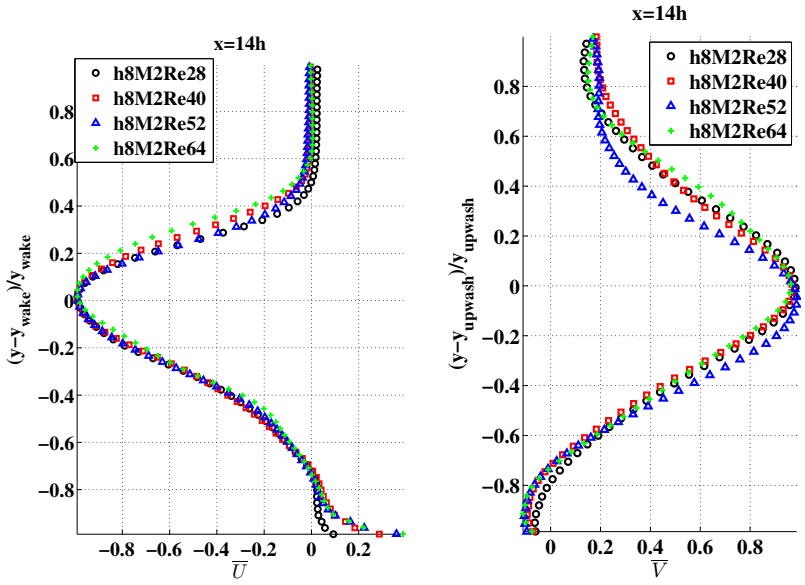

(a) Self similarity of horizontal velocity

(b) Self similarity of vertical velocity

Figure 5.31: Self-similarity profiles at x=14h for cases with different Reynolds number using scaling parameters given in Sun et al. (2014).

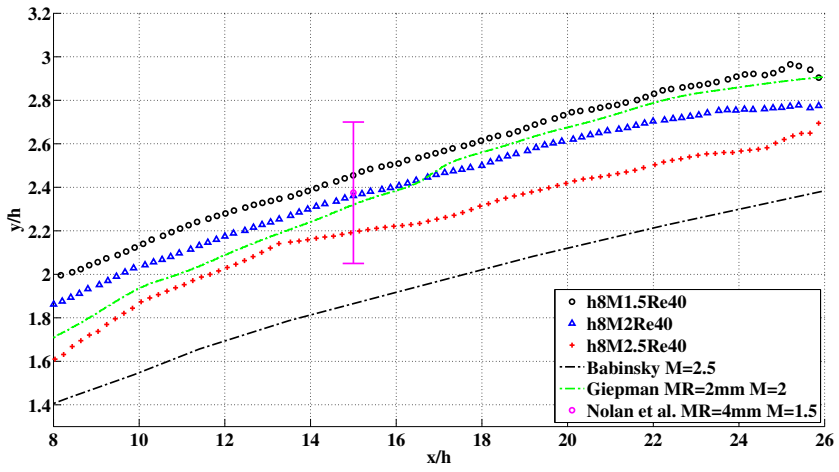

Figure 5.32: Wake location from current experiment with changing Mach number cases compared with results from Babinsky et al. (2009), Giepman et al. (2013) and Nolan and Babinsky (2011).

from equation 2.12, in general, can be given by the following power law fit

$$\frac{V_{\max}}{U_\infty} = c\left(\frac{x}{h}\right)^b \tag{5.1}$$

where c is a constant which depends on the micro-ramp height (Sun et al. have shown it to be 20 for 3mm micro-ramp and 25 for 4mm micro-ramp) and b is the power which is

approximately around -1.6 to -1.7 (for fits by Sun et al.). The power law approximation was applied for current test case with changing micro-ramp heights, and the following relations were obtained:

$$\frac{V_{\max}}{U_\infty} = 3.8\left(\frac{x}{h}\right)^{-1.29} \qquad (h6M2Re40) \tag{5.2a}$$

$$\frac{V_{\max}}{U_\infty} = 5.0\left(\frac{x}{h}\right)^{-1.34} \qquad (h8M2Re40) \tag{5.2b}$$

$$\frac{V_{\max}}{U_\infty} = 5.1\left(\frac{x}{h}\right)^{-1.3} \qquad (h10M2Re40) \tag{5.2c}$$

The power law fits are shown in figure 5.33 with colored symbols and power law fits for case

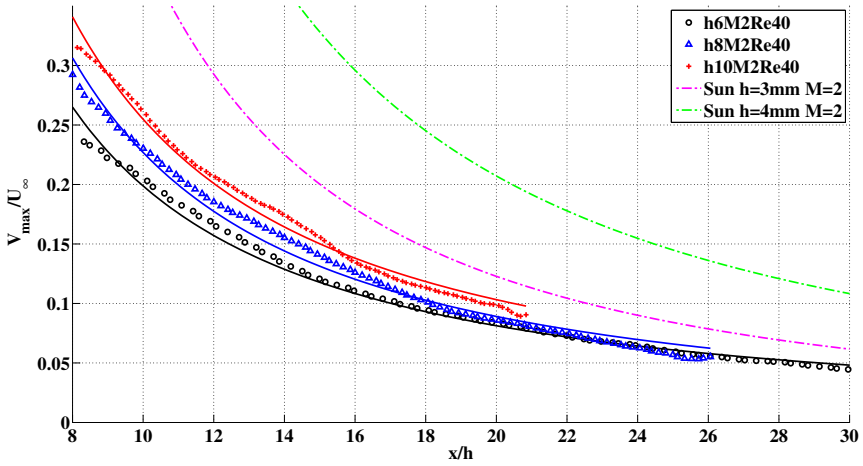

Figure 5.33: Power law fit on upwash strength for cases h6M2Re40, h8M2Re40 and h10M2Re40 compared with the power law given by Sun et al. (2014).

h6M2Re40 (black), h8M2Re40 (blue) and h10M2Re40(red). It can be seen that the power law fits from the current case differ from those obtained by Sun et al. (2014). There can be two reasons for this:

- Firstly, the upwash strength is probably affected by the value of $\frac{h}{\delta_{99}}$. The power law curve fit for the 3mm case by Sun et al. ($\frac{h}{\delta_{99}} = 0.58$) is closer to that for case h10M2Re40 ($\frac{h}{\delta_{99}} = 0.57$) compared to other cases but the difference indicates that there is some other factor in addition to $\frac{h}{\delta_{99}}$, which is influencing the curve fits.
- The second reason might be the difference in Reynolds number. It was reported in section 5.2.6 that change in Reynolds number influences the upwash strength in region close to the micro-ramp (higher Re_θ gives lower upwash strength). Sun et al. had a much lower Reynolds number ($Re_{\theta_{inc}} = 20.2 \times 10^3$) compared to current experiments ($Re_{\theta_{inc}} = 64.6 \times 10^3$ for cases at M2Re40).

Chapter 6

Conclusions

To answer the research question (section 2.4), measurements of the mean flow structure downstream of a micro-ramp at different device heights, Mach number and Reynolds number were carried out using planar PIV, complemented with surface oil flow visualization. As a result, several conclusions can be drawn from the work carried out in this thesis which are summarized in table 6.1. The trends reported in PIV measurements downstream of the micro-ramp are scaled with respect to the height (i.e. trends at same x/h location).

The surface oil flow visualizations showed that changing the Reynolds number does not affect the flow features near the wall. However, with increasing Mach number, the horse-shoe vortex footprint is less curved compared to that for a lower Mach number. It was also observed that at lower Mach number, the vortices move further apart than at higher Mach numbers.

The effects of changing micro-ramp height agree well with earlier literature. A larger device height gives a fuller velocity profile near the wall, but it also makes the device wake larger along the center-line of the micro-ramp. The location of the wake scales with height, however, the rate of the stream-wise evolution of the wake location ($\frac{dy_{wake}}{dx}$) is slightly larger for a larger micro-ramp. The upwash strength is also higher for a larger micro-ramp. A larger upwash strength implies stronger primary vortices for larger devices and also explains the higher $\frac{dy_{wake}}{dx}$ as the wake is pushed more strongly away from the wall.
The gap between the upper and lower shear layers in the device wake can give an estimate of the size of the momentum deficit region. An analysis of the shear layers showed that the size of the momentum deficit region depends solely on device height for the tested range of Mach number and Reynolds number. The size of the momentum deficit region shows a very gradual growth while moving downstream. The shape factor shows a strong dependence on the device height, being lower for a larger device. From the current results, no clear trends were observed on its downstream evolution with respect to height h or the boundary layer thickness δ_{99}.

It was observed that for a lower Mach number, the normalized velocity profile is fuller near

the wall. The wake location is lower for a higher Mach number, but the evolution of the wake location ($\frac{dy_{wake}}{dx}$) is similar, indicating the streamwise decay rate of the primary vortices does not depend on Mach number. The wake strength for the Mach 2.5 case is higher than that for the Mach 1.5 case, but the difference between the wake strength becomes smaller as one moves downstream.
The upwash strength recorded along the center-line depends on two factors: the vortex strength and the distance between the vortex core and the center-line. It was seen from the oil flow visualizations that the two primary vortices move closer at a higher Mach number. The PIV measurements revealed no clear trend in the development of the upwash strength with Mach number; except in the vicinity of the micro-ramp, where higher upwash values were recorded for the lower Mach number case. Since the vortex cores are approximately at the same distance from the center-line in the vicinity of micro-ramp, it can be deduced from the observations that the vortex strength decreases with increasing Mach number. This observation on vortex strength is well supported by the work of Nolan (2013). Although the vortex strength depends on Mach number, it was seen that the rate of decay for the vortices is independent of the Mach number. The momentum deficit region was lower for a higher Mach number, as estimated from the shear layer locations. The shape factor for a higher Mach number is higher at all x-locations. It was also observed that with increasing Mach number, the incompressible shape factor crosses its undisturbed boundary layer value at increasing distance behind the micro-ramp.

Reynolds number in the tested range, in general, does not seem to have much effect on the mean wake properties along the center-line of the micro-ramp. The wake location and the size of the momentum deficit region remain similar for all tested cases. However, some differences were observed in the region near the micro-ramp which vanish downstream. The velocity profile near the micro-ramp is fuller for a higher Reynolds number. Also, for the higher Reynolds number, the wake strength and the upwash strength are lower in the region near the micro-ramp. The downstream evolution of the shape factor scaled with the boundary layer thickness δ_{99}.

Since the boundary layer profiles were self-similar for all the cases, it can be concluded that the basic flow structures do not change with changing flow conditions for a fixed micro-ramp geometry. However, the strength and size of the flow structures (vortex core, low-momentum region, etc.) does depend on flow conditions. The wake locations obtained form the current experiment match well with the wake locations obtained by Giepman et al. (2013) and Sun et al. (2014). Wake location for the Mach 2.5 case did not match that well with Babinsky et al. (2009)'s results probably because the curve form Babinsky et al. is a best fit curve based on data from three downstream locations.

Table 6.1: Observations from PIV measurements. Trends are considering the same x/h location.

Property Measured	**Micro-ramp height**	**Mach number**	**Reynolds number**
Wake Location	Scales linearly with h $\frac{dy_{wake}}{dx}$ also increases with h	Wake location lower for higher M	No effect
Wake Strength	Downstream development scales approximately with h	Larger at higher M	Near MR: lower for higher Re; Downstream: no effect
Upwash Strength	Increases with increasing h	Near MR: lower for higher M; Downstream: No visible trend with M	Near MR: lower for higher Re; Downstream: No effect
Shear layers	Shear layer location and gap both scale linearly with h	Shear layer location is lower for higher M; No effect on shear layer gap	No effect
Shape Factor	Lower shape factor for larger h	Higher for higher M	Scales with $\frac{x}{\delta_{99}}$

Chapter 7

Recommendations

As a result of this thesis project, several recommendations are proposed. These are not exhaustive and they are suggestions in the hope of inspiring future research into the subject.

The measurements in the region close to the micro-ramp are affected by two factors. One is the reflection coming from the micro-ramp and the other is the low PPP levels in the wake. The reflections are the limiting factor in most of the cases. To minimize the reflections, it would be advisable to use TiO_2 particles for seeding because they are much brighter compared to DEHS, hence the laser can be operated at much lower powers, thus minimizing the intensity of reflections. If the PPP levels in the wake close to the micro-ramps are very low then instead of using single-image correlation technique to give instantaneous, sum-of-correlation technique can be used over a large number of image pairs to give a mean flow field. Particle tracking velocimetry (PTV) can also be adopted if the particle concentration is very low. The PIVTEC Aerosol Generator (figure 3.5(a)) can only operate till 5 bar over-pressure which limits its application on conditions where large stagnation chamber pressure is required (for example the M2Re64 case). Hence, it would be advisable to use a seeding generator which has a higher operating range.

Another factor that needs to be observed is the strength and locations of primary vortices using 3-dimensional tomographic-PIV at different Mach numbers. It can then give a useful insight into the trends that were observed on the upwash strength for varying Mach number cases as discussed in section 5.2.6. The wake locations obtained by Lee and Loth (2011) using LES did not match with the experimental observations probably because the Reynolds number was very low, limited by the computation costs. Hence, the numerical simulations need to be improved further to give results more comparable with experiments. It would also be beneficial to have experimental results from 3-dimensional flow field in the region close to the micro-ramps, where some differences in wake properties were observed, at different Reynolds number.

Bibliography

Topas di-ethyl-hexyl-sebacat. URL http://www.topas-gmbh.de/dateien/prospekt/dehs_prspe.pdf. [30]

IHS ESDU 93024. Vortex generators for control of shock-induced separation. part 1: introduction and aerodynamics., 1995. [15]

B. H. Anderson, J. Tinapple, and L. Surber. Optimal control of shock wave turbulent boundary layer interactions using micro-array actuation. *AIAA paper*, 3197:2006, 2006. [vii, xiii, 2, 11, 29]

J. D. Anderson Jr. *Fundamentals of aerodynamics*. Tata McGraw-Hill Education, 1985. [9]

P. R. Ashill, J. L. Fulker, and K. C. Hackett. A review of recent developments in flow control. *THE AERONAUTICAL JOURNAL*, 109:205–232, 2005. [xiv, 2, 17]

P.R. Ashill, J.L. Fulker, and K.C. Hackett. Research at dera on sub boundary layer vortex generators (sbvgs). In *39th AIAA Aerospace Sciences Meeting*, 2011. [15, 16, 25]

H. Babinsky. Understanding micro-ramp control of supersonic shock wave boundary layer interactions. Technical report, Cambridge University Department of Engineering, 2007. [2]

H. Babinsky, Y. Li, and C. W. Pitt Ford. Microramp control of supersonic oblique shock-wave/boundary-layer interactions. *AIAA JOURNAL*, 47:668–675, 2009. [vii, xiii, xiv, xvii, 2, 4, 7, 12, 13, 15, 17, 18, 20, 21, 22, 25, 59, 63, 65, 69, 74, 76, 80]

P.L. Blinde, R.A. Humble, B.W. van Oudheusden, and F. Scarano. Effects of micro-ramps on a shock wave/turbulent boundary layer interaction. *Shock Waves*, 19(6):507–520, 2009. [4]

J. Cousteix. *Aâerodynamique: Turbulence et Couche Limite*. Cepadues-éditions, 1989. [9, 47]

J Délery and R Bur. The physics of shock wave/boundary layer interaction control: last lessons learned. *OFFICE NATIONAL D ETUDES ET DE RECHERCHES AEROSPATIALES ONERA-PUBLICATIONS-TP*, (181), 2000. [xiii, 10]

R.H.M. Giepman, F.F.J. Schrijer, and B.W. Van Oudheusden. Flow control of an oblique shock wave reflection with micro-ramp vortex generators: Effects of location and size. In *5TH EUROPEAN CONFERENCE FOR AERONAUTICS AND SPACE SCIENCES (EUCASS)*, 2013. TU Delft Repository. [xiv, xvii, 4, 20, 21, 25, 73, 74, 76, 80, 97]

R.H.M. Giepman, F.F.J Schrijer, and B.W. van Oudheusden. Investigation of a transitional oblique shock wave reflection using piv. *17th International Symposium on Applications of Laser Techniques to Fluid Mechanics*, 2014. [27, 35]

E.L. Goldsmith and J. Seddon. *Practical intake aerodynamic design*. Amer Inst of Aeronautics &, 1993. [1]

R.H. Graham. *SR-71 Revealed: The inside story*. Zenith Imprint, 1996. [1]

T. Herges, G. Elliott, C. Dutton, and Y. Lee. Micro-vortex generators and recirculating flow control of normal shock stability and position sensitivity. In *48th AIAA Aerospace Sciences Meeting Including the New Horizons Forum and Aerospace Exposition*, 2010. [xiv, 21, 22]

S. M. Hirt and B. H. Anderson. Experimental investigation of the application of microramp flow control to an oblique shock interaction. In *47th AIAA Aerospace Sciences Meeting Including*, 2009. [4]

R.A. Humble. *Unsteady flow organization of a shock wave/boundary layer interaction*. PhD thesis, Delft University of Technology, 2009. [xiii, xv, 9, 10, 47, 49, 50]

A. L. Kistler. Fluctuation measurements in a supersonic turbulent boundary layer. *Physics of Fluids (1958-1988)*, 2(3):290–296, 1959. [49]

P.S. Klebanoff. *Characteristics of turbulence in a boundary layer with zero pressure gradient*. National Advisory Committee for Aeronautics, 1955. [vii, xv, 49]

S. Lee and E. Loth. Effect of mach number on flow past microramps. *AIAA Journal*, 49: 97–110, 2011. [xiv, 20, 21, 22, 53, 83]

S. Lee, E. Loth, and C. Wang. Les of supersonic turbulent boundary layers with microvortex generators. In *25th AIAA Applied Aerodynamics Conference*, 2007. [4, 17]

Q. Li and C. Liu. Les for supersonic ramp control flow using mvg at m= 2.5 and reθ= 1440. *AIAA paper*, 592:2010, 2010. [xiii, 12, 13]

Q. Li, Y. Yan, P. Lu, A. Pierce, C. Liu, and F. Lu. Numerical and experimental studies on the separation topology of the mvg controlled flow at m= 2.5. *AIAA paper*, 72:2011, 2011. [xiii, 4, 13, 14, 51]

C. Liu, Z. Sun, X. Wang, and Y. Yan. The vortical structures in the rear separation and wake produced by a supersonic micro-ramp. In *51st AIAA Aerospace Sciences Meeting*, 2013. [xiii, 14, 15]

F.W. Matting, D.R. Chapman, J.R. Nyholm, and A.G. Thomas. Turbulent skin friction at high mach numbers and reynolds numbers in air and helium. Technical report, DTIC Document, 1961. [45]

P. Meunier and T. Leweke. Analysis and treatment of errors due to high velocity gradients in particle image velocimetry. *Experiments in fluids*, 35(5):408–421, 2003. [37]

M.V. Morkovin. Effects of compressibility on turbulent flows. *Mecanique de la Turbulence*, pages 367–380, 1962. [49]

W. R. Nolan and H. Babinsky. Characterization of micro-vortex generators in supersonic flows. In *49th AIAA Aerospace Sciences Meeting*, 2011. [xiv, xvii, 20, 21, 74, 75, 76]

W.R. Nolan. *A Study of Vortex Generator Behaviour*. PhD thesis, University of Cambridge, 2013. [xiv, 16, 17, 18, 21, 23, 24, 25, 66, 80]

S.K. Norfleet. An evaluation of wall effects on stack flow velocities and related overestimation bias in epa's stack flow reference methods. In *1998 EPRI CEMS Users Group Meeting, New Orleans, Louisiana*, 1998. [8]

S.K. Norfleet and G. Savannah. Ctm-041 and potential revisions to epa reference method 2h. In *2005 EPRI CEMS Users Group Meeting, Savannah, Georgia*, 2005. [8]

M. Raffel. *Particle image velocimetry: a practical guide*. Springer, 2007. [xiv, 30]

D. Ragni, F.F.J. Schrijer, B.W. Van Oudheusden, and F. Scarano. Particle tracer response across shocks measured by piv. *Experiments in fluids*, 50(1):53–64, 2011. [30]

Mohd R. Saad, H. Zare-Behtash, A. Che-Idris, and K. Kontis. Micro-ramps for hypersonic flow control. *Micromachines*, 3(2):364–378, 2012. [13]

P.G. Saffman. *Vortex dynamics*. Cambridge university press, 1992. [16]

H. Schlichting, K. Gersten, and K. Gersten. *Boundary-layer theory*. Springer, 2000. [xv, 9, 44, 45, 46, 47]

A.J. Smits and J.P. Dussauge. *Turbulent Shear Layers in Supersonic Flow*. Springer, 2006. ISBN 9780387263052. URL http://books.google.nl/books?id=KtpFdcTEbQQC. [47, 48]

L.J. Souverein. *On the scaling and unsteadiness of shock induced separation*. PhD thesis, Delft University of Technology, 2010. [xiii, xv, 3, 49]

Z. Sun. *Micro Ramps in Supersonic Turbulent Boundary Layers: An Experimental and Numerical Study*. PhD thesis, Delft University of Technology, 2014. [xiv, 24, 25, 29]

Z. Sun, F.F.J. Schrijer, F. Scarano, and B.W. Van Oudheusden. The three-dimensional flow organization past a micro-ramp in a supersonic boundary layer. *Physics of Fluids (1994-present)*, 24(5):055105, 2012. [13, 14, 36, 37]

Z. Sun, F. Scarano, B.W. van Oudheusden, and F.F.J. Schrijer. Numerical and experimental investigations on the wake of a supersonic micro-ramp. In *51st AIAA Aerospace Sciences Meeting*, 2013. [xiii, xiv, 14, 15, 16]

Z. Sun, F.F.J. Schrijer, F. Scarano, and B.W. van Oudheusden. Decay of the supersonic turbulent wakes from micro-ramps. *Physics of Fluids (1994-present)*, 26(2):025115, 2014. [xiv, xvii, 17, 19, 20, 21, 74, 75, 76, 77, 80]

E.R. Van Driest. Turbulent boundary layer in compressible fluids. *Journal of Seronautical Sciences*, 18(3):145–160, 1951. [8]

F.M. White and I. Corfield. *Viscous fluid flow*, volume 2. McGraw-Hill New York, 2006. [7, 44, 46, 49]

M. Wu and M.P. Martin. Direct numerical simulation of supersonic turbulent boundary layer over a compression ramp. *AIAA journal*, 45(4):879–889, 2007. [10]

Y. Yan, C. Chen, X. Wang, and C. Liu. Les and analyses on the vortex structure behind supersonic micro vortex generator with turbulent inflow. *Applied Mathematical Modelling*, 38(1):196–211, 2014. [14]

Appendix A

Undisturbed Boundary Layer Contours

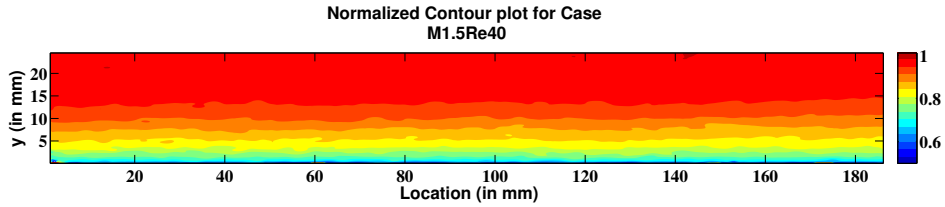

(a) Case M1.5Re40

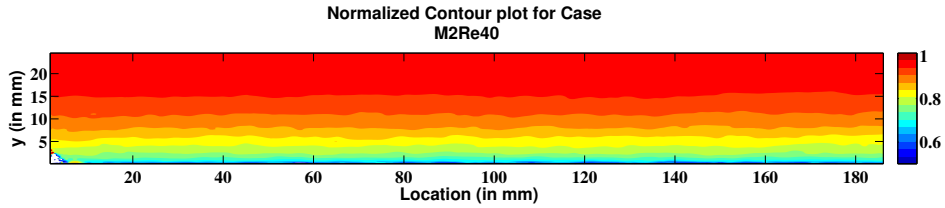

(b) Case M2Re40

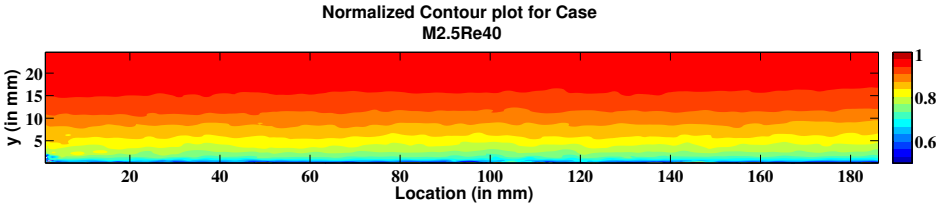

(c) Case M2.5Re40

Figure A.1: Contour plots for varying Mach number cases.

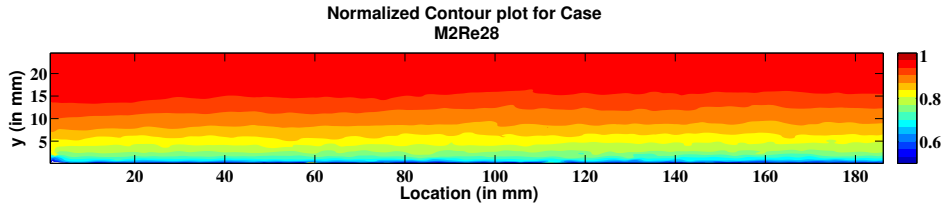

(a) Case M2Re28

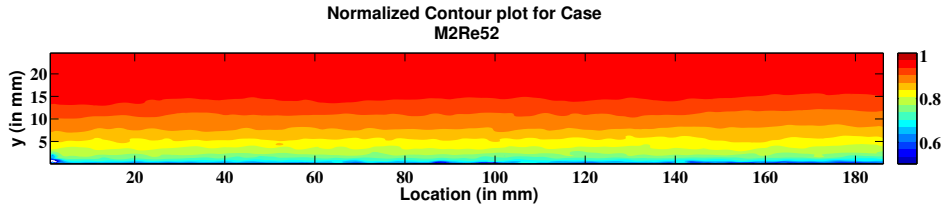

(b) Case M2Re52

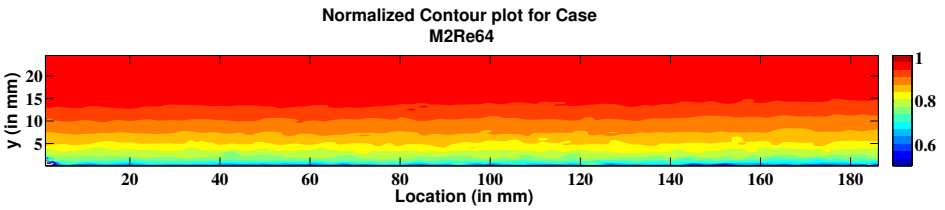

(c) Case M2Re64

Figure A.2: Contour plots for varying Reynolds number cases. (See also figure A.1(b) for case M2Re40.)

Appendix B

Log Law Fits

The Van-Driest's log law fit for case M2Re40 has been presented in section 4.2. The fits for all other undisturbed boundary layer cases is presented in this appendix.

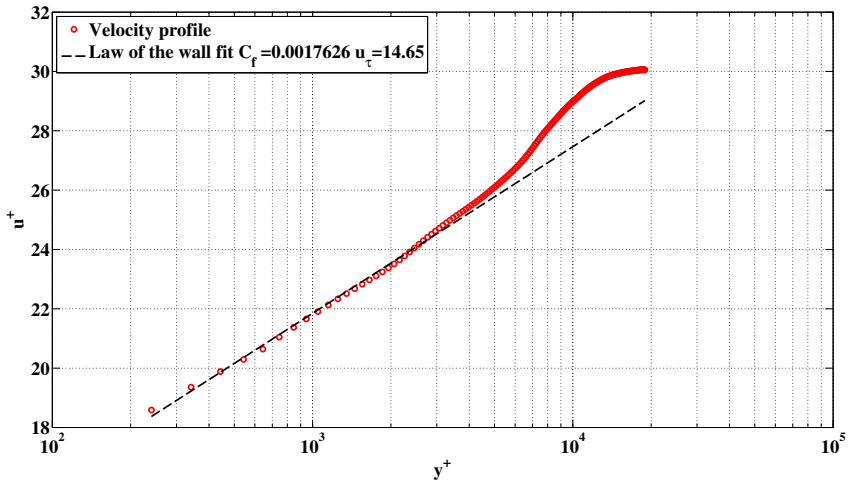

Figure B.1: Log law plot for case M1.5Re40

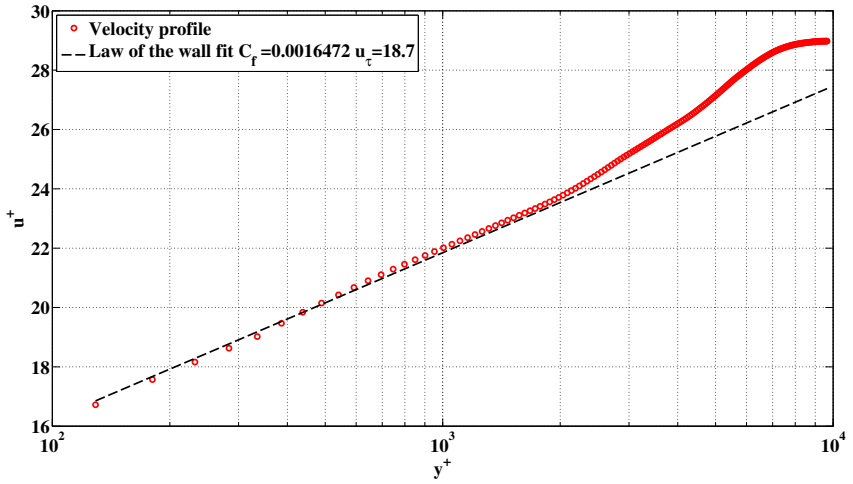

Figure B.2: Log law plot for case M2Re28

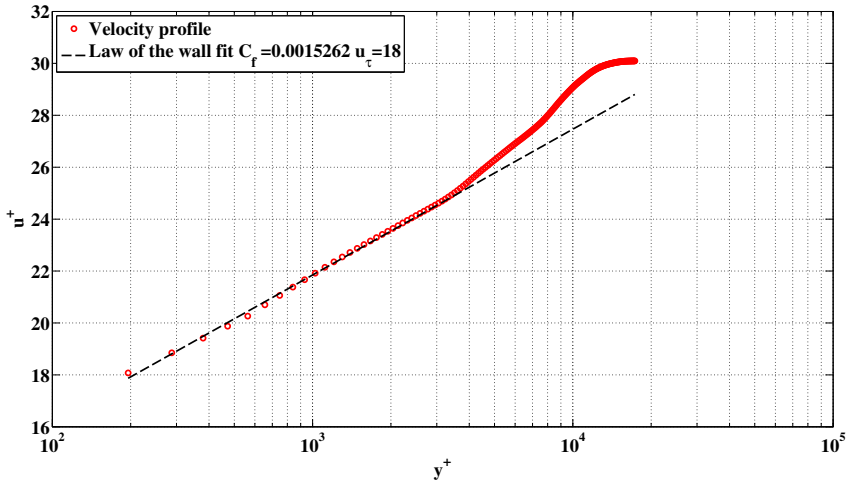

Figure B.3: Log law plot for case M2Re52

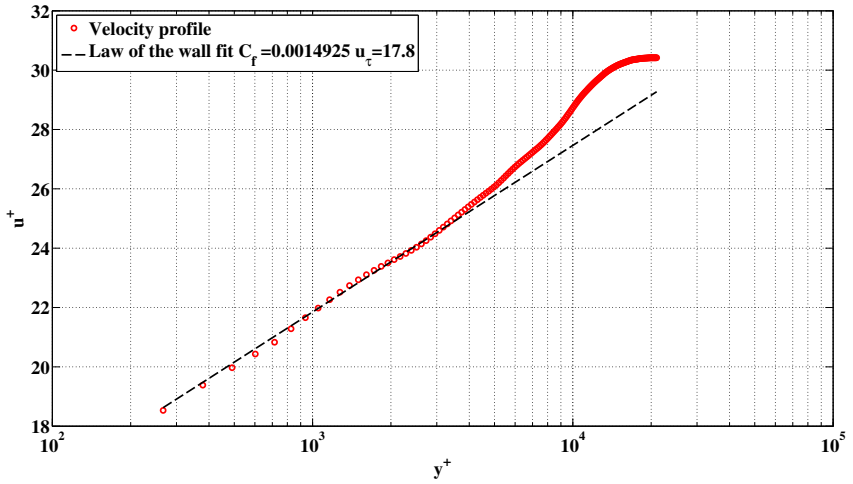

Figure B.4: Log law plot for case M2Re64

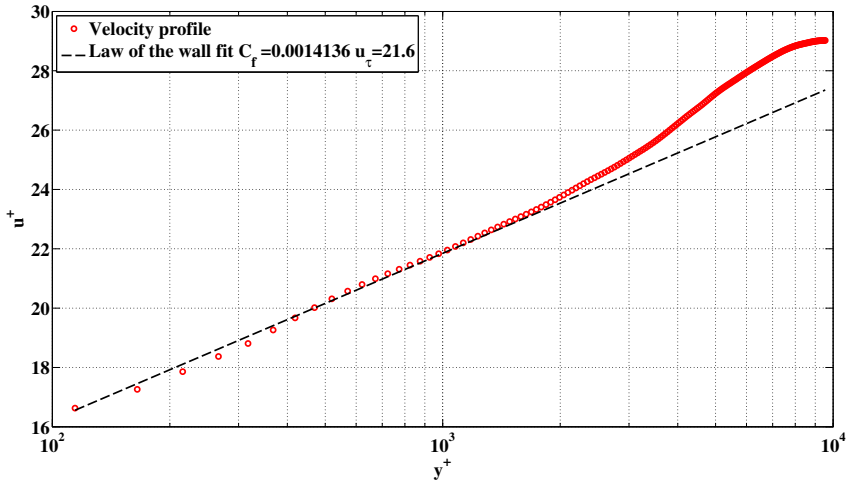

Figure B.5: Log law plot for case M2.5Re40

Appendix C

Upwash Profiles

In this appendix, the v-velocity profiles behind the micro-ramp are presented and discussed. A typical v-velocity profile can be seen in figure 5.10(b).

Micro-ramp height effects Figure C.1 shows the v-velocity profiles behind the micro-ramp in the cases with changing device height. It can be seen from the figure that the upwash for the case h10M2Re40 is highest and that for the case h6M2Re40, the lowest. The location of the maximum upwash scales with micro-ramp height.

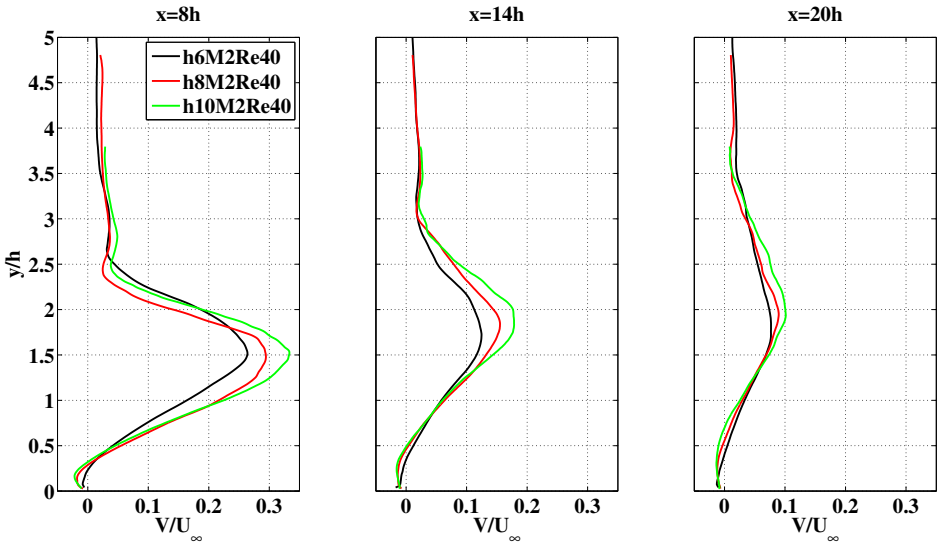

Figure C.1: V-velocity profiles at x=8h, 14h and 20h for changing Micro-ramp heights.

Mach number effects The Mach number effects on the maximum upwash do not show any conclusive trend as can be seen in figure C.2. At x=8h, the maximum upwash strength is highest for case h8M2Re40, and lowest for case h8M1.5Re40, showing a trend which has

already been presented in section 5.2.6. The y-location of maximum upwash decreases with an increasing Mach number, indicating that the primary vortices are lower. This conforms with the trend in the wake location for increasing Mach number, as discussed in section 5.2.4.

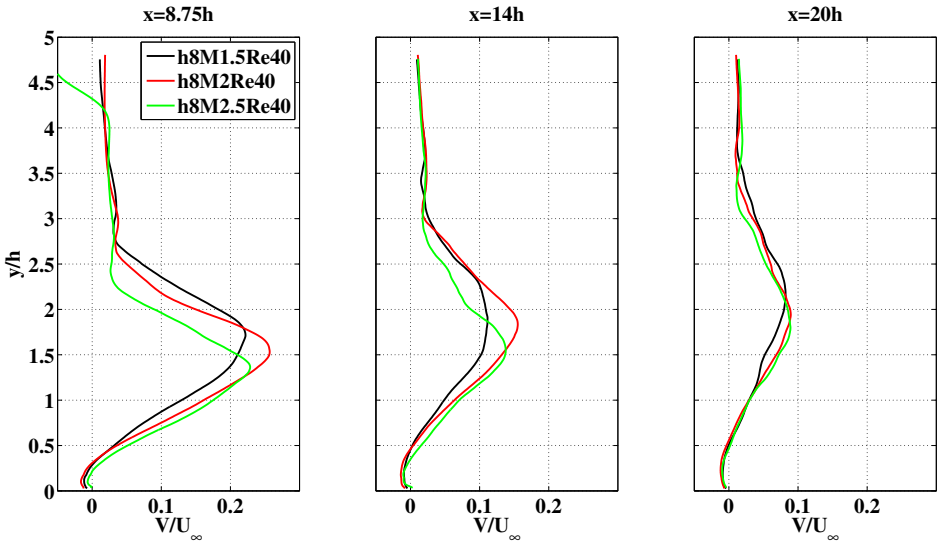

Figure C.2: V-velocity profiles at x=8h, 14h and 20h for changing Mach number.

Reynolds number effects The upwash strength with varying Reynolds numbers can be seen in figure C.3. It clearly shows that near the micro-ramp at x=8h, the upwash strength is slightly lower for h8M2Re64, but as one moves away form the micro-ramp, the difference decreases and the profiles become identical.

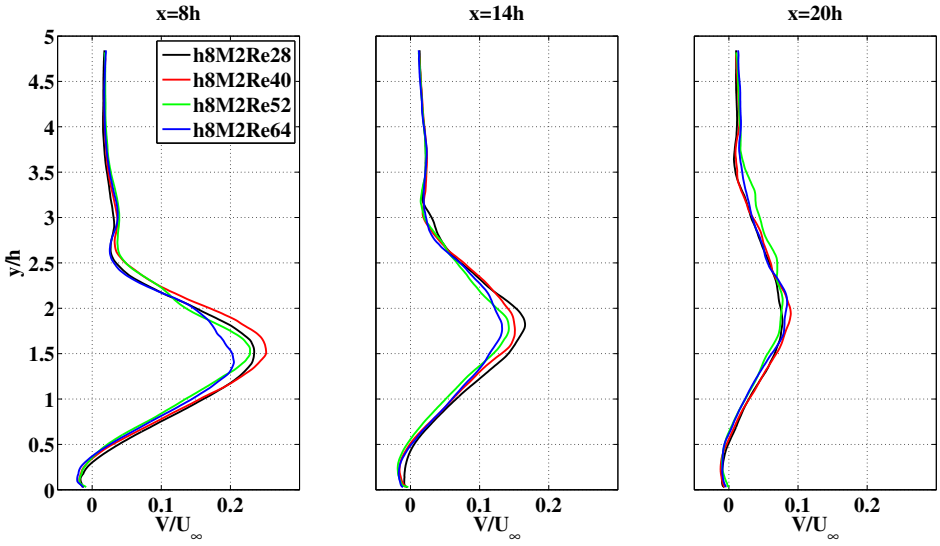

Figure C.3: V-velocity profiles at x=8h, 14h and 20h for changing Reynolds number.

Appendix D

Shape Factor scaling with δ_{99}

In this appendix, the evolution of incompressible shape factor as a function of x/δ_{99} for all the cases is presented. According to Giepman et al. (2013), the effectiveness of micro-ramp controlled flow on SWBLI scales with the boundary layer thickness. They arrived at this conclusion by measuring the added momentum flux, which essentially captures the fullness of the boundary layer profile near the wall. Incompressible shape factor can also be used to show the similar effects on the profile. It can be seen from figure D.1 that for a constant boundary layer thickness (at M2Re40), the shape factor also depends on the device height. Although, when the device height is kept constant, and the boundary layer thickness is varied (by varying the Reynolds number), the shape factor plots do fall on each other as can be seen in figure D.2. However, it is to be noted that the undisturbed boundary layer shape factors are different for different Reynolds number conditions and hence, the shape factor for each case with micro-ramp, reaches its corresponding undisturbed value at different $\frac{x}{\delta_{99}}$ locations. As an example of previous statement, case h8M2Re28 reaches the undisturbed boundary layer H at $\frac{x}{\delta_{99}} = 7.2$, whereas case h8M2Re64 reaches the corresponding undisturbed boundary layer H at $\frac{x}{\delta_{99}} = 7.8$.

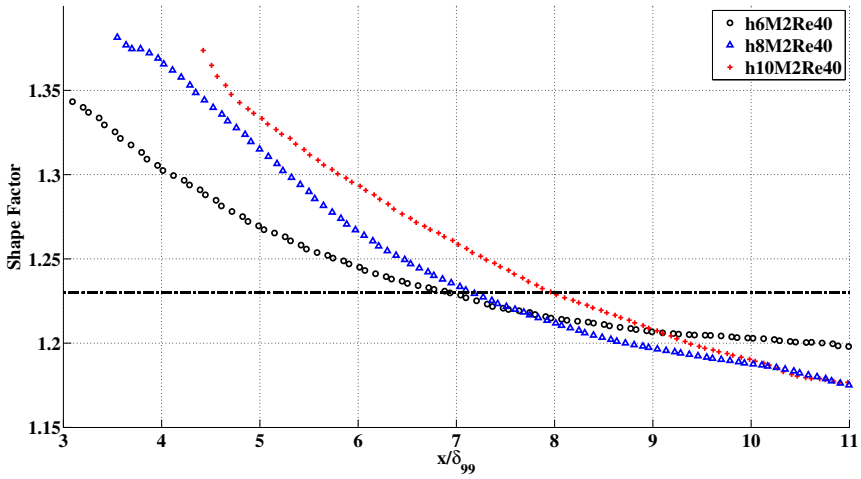

Figure D.1: Shape Factor variation for changing micro-ramp height over $\frac{x}{\delta_{99}}$. Black line denotes incompressible shape factor for undisturbed boundary layer case M2Re40.

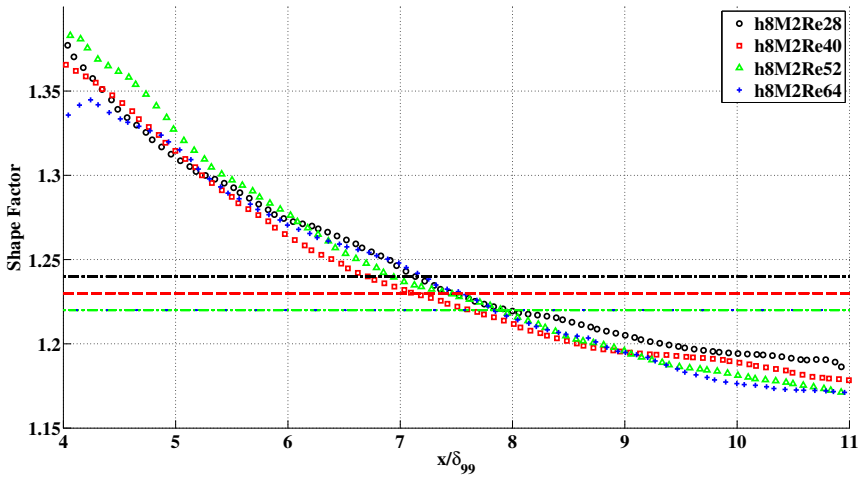

Figure D.2: Shape Factor variation for changing Reynolds number over $\frac{x}{\delta_{99}}$.Black line denotes incompressible shape factor for undisturbed boundary layer case M2Re28, red line for case M2Re40, green and blue dotted lines for cases M2Re52 and M2Re64 respectively.